NASA/TM–20210010310

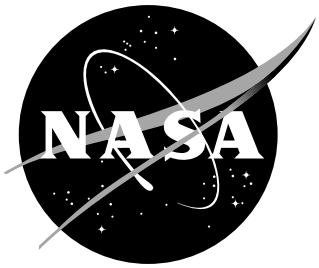

# Analysis of nonlinear shrinkage for the bound metal deposition manufacturing using multi-scale approach

*Dmitry G. Luchinsky*
*SGT Inc., Ames Research Center, Moffett Field, California*

*Vasyl Hafiychuk*
*SGT Inc., Ames Research Center, Moffett Field, California*

*Kevin R. Wheeler*
*Ames Research Center, Moffett Field, California*

*Tracie J. Prater*
*Marshal Space Flight Center, Huntsville, Alabama*

October 2020

NASA STI Program . . . in Profile

Since its founding, NASA has been dedicated to the advancement of aeronautics and space science. The NASA scientific and technical information (STI) program plays a key part in helping NASA maintain this important role.

The NASA STI Program operates under the auspices of the Agency Chief Information Officer. It collects, organizes, provides for archiving, and disseminates NASA's STI. The NASA STI Program provides access to the NASA Aeronautics and Space Database and its public interface, the NASA Technical Report Server, thus providing one of the largest collection of aeronautical and space science STI in the world. Results are published in both non-NASA channels and by NASA in the NASA STI Report Series, which includes the following report types:

- TECHNICAL PUBLICATION. Reports of completed research or a major significant phase of research that present the results of NASA programs and include extensive data or theoretical analysis. Includes compilations of significant scientific and technical data and information deemed to be of continuing reference value. NASA counterpart of peer-reviewed formal professional papers, but having less stringent limitations on manuscript length and extent of graphic presentations.
- TECHNICAL MEMORANDUM. Scientific and technical findings that are preliminary or of specialized interest, e.g., quick release reports, working papers, and bibliographies that contain minimal annotation. Does not contain extensive analysis.
- CONTRACTOR REPORT. Scientific and technical findings by NASA-sponsored contractors and grantees.
- CONFERENCE PUBLICATION. Collected papers from scientific and technical conferences, symposia, seminars, or other meetings sponsored or co-sponsored by NASA.
- SPECIAL PUBLICATION. Scientific, technical, or historical information from NASA programs, projects, and missions, often concerned with subjects having substantial public interest.
- TECHNICAL TRANSLATION. English- language translations of foreign scientific and technical material pertinent to NASA's mission.

Specialized services also include creating custom thesauri, building customized databases, and organizing and publishing research results.

For more information about the NASA STI Program, see the following:

- Access the NASA STI program home page at ***http://www.sti.nasa.gov***
- E-mail your question via the Internet to help@sti.nasa.gov
- Fax your question to the NASA STI Help Desk at 443-757-5803
- Phone the NASA STI Help Desk at 443-757-5802
- Write to:
  NASA STI Help Desk
  NASA Center for AeroSpace Information
  7115 Standard Drive
  Hanover, MD 21076–1320

NASA/TM–20210010310

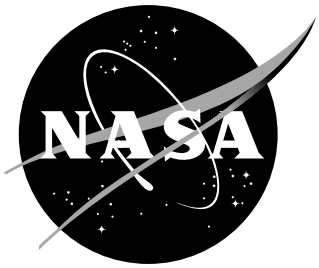

# Analysis of nonlinear shrinkage for the bound metal deposition manufacturing using multi-scale approach

*Dmitry G. Luchinsky*
*SGT Inc., Ames Research Center, Moffett Field, California*

*Vasyl Hafiychuk*
*SGT Inc., Ames Research Center, Moffett Field, California*

*Kevin R. Wheeler*
*Ames Research Center, Moffett Field, California*

*Tracie J. Prater*
*Marshal Space Flight Center, Huntsville, Alabama*

National Aeronautics and
Space Administration

Ames Research Center
Moffett Field, California 94035-2199

October 2020

## Acknowledgments

We are grateful to Dr. Taku Ozawa, Hiroya Nitta and Kenta Chaki for providing J-OCTA software support, help with MD simulations and valuable discussion. We thank Dr. Sudipta Biswas for providing extensive support of our Phase Field modeling of sintering.



Available from:

NASA Center for AeroSpace Information
7115 Standard Drive
Hanover, MD 21076-1320
443-757-5802

## Abstract

We consider problem of nonlinear shrinkage of the metal part during bound metal deposition manufacturing on the ground and in zero-G. To analyze this problem we developed multi-scale physics-based approach that spans atomistic dynamics at the scale of nanoseconds and the full part shrinkage at the time scale of hours. Using this approach we estimated the key parameters of the problem including grain boundary width, coefficient of surface diffusion, initial redistribution of particles during debinding stage, micro-structure evolution from round particles to densely packed grains and corresponding change of the total and chemical free energy, and sintering stress. The introduced method was used to predict shrinkage at the level of two particles, filament cross-section, sub-model, and the whole green, brown, and metal parts. To further improve accuracy and reliability of the shrinkage predictions we propose concept of intelligent additive manufacturing of metal powders in space that combines the strengths of both physics-based and data-driven methods of analysis of AM.

# Part I
# Brief introduction to sintering

## 1 Bind metal deposition: processing [41]

The In-Space Manufacturing (ISM) project at NASA Marshall Space Flight Center is currently working with industry partners to develop capabilities for 3D printing of metals which can be demonstrated on the International Space Station (ISS). The majority of spare parts identified as candidates for on-demand manufacturing on space missions are metallics. Thus demonstration of metal AM on ISS will significant enhance the state of the art for in-space manufacturing and broaden its infusion potential as an alternative to prepositioning of spares on long duration exploration missions. One technology being matured for an ISS experiment is an integrated system for Materials Extrusion Additive Manufacturing (MEAM) with highly filled polymers (HP), which uses sacrificial polymer binders (removed via a furnace cycle following printing) to produce metallic components. This work is led by the payload developer Techshot, Inc. The modeling effort described in this paper was performed to better understand operation of this process in microgravity and phenomena associated with material consolidation and part shrinkage. There are several commercial variations of the MEAM process being pursued for ISM which are considered for reference. In addition to metals, these processes can also be used to manufacture ceramics.

Two companies based in the USA, Desktop Metal Inc. and Markforged Inc., currently offer MEAM machines that use special profiles (rods) made up of metal or ceramic powder with a thermoplastic binder system. Desktop Metal calls their process bound metal depositionTM and Markforged calls theirs atomic diffusion additive manufacturing (ADAM). The profiles are fit into cartridges and are then fed into a plasticizing unit where the highly-filled thermoplastic composite is soft enough for extrusion. The soft material accumulates in a reservoir and finally a mechanical drive system (e.g., plunger) pushes the soft material and deposits it onto the building platform in a layer-by-layer manner.

Another particular difference is that the machine patented by Desktop Metal Inc. has an ultrasonic vibrator with sufficient energy to ultrasonically bond an extruded building material onto the previously deposited layers. Alternatively, the machine by Markforged Inc. has a laser scanning displacement sensor on the printed head that acts as an in-process inspection tool to ensure that the correct dimensions are being printed.

The rods use similar materials as used in the well-established pro-

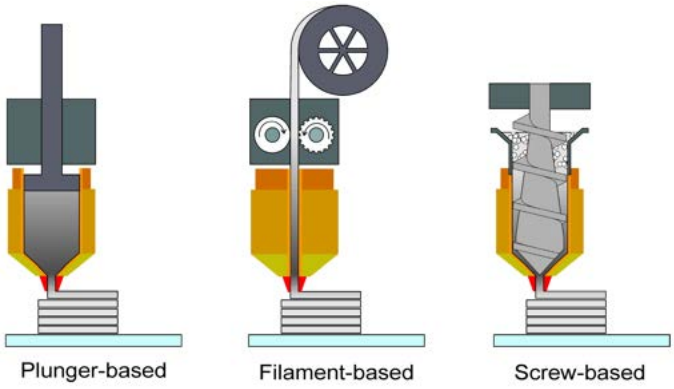


Figure 1. Different types and approaches for extrusion-based additive manufacturing. The plunger-based method is used by Desktop Metal Inc.

cess of powder injection molding (PIM) [44]. Recall, that in PIM the powder content usually ranges from 50 to 65% in volume, although there are claims of optimized commercial formulations in which even more than 80% is used. If the powder content is found to be lower than 50 vol.%, the sintering ability of the feedstock and the final density of the part are significantly lowered. From another standpoint, it is also important to keep the viscosity of the feedstock as low as possible in order to facilitate the injection molding process, reason for why a powder content higher than 65 vol.% should be handled with care [61].

## 1.1 Basic details of processing

Markforged Inc. offers their proprietary binder system with powder of stainless steel (316L and 17-4PH), and advertises in-development face feedstocks with Inconel (625), titanium alloy (Ti-6Al-4V), tool steel (A-2 and D-2), and aluminum (6061 and 7075). The Markforged Inc. binder is thermally debound before sintering. Desktop Metal Inc. advertises the development of feedstock materials with powders of stainless steel, high-performance steel, copper, tool steel, carbide, aluminum, heavy alloys, titanium, magnetics, low expansion metals, and superalloys. The binder used by Desktop Metal Inc. is solvent debound before thermal debinding and sintering is done.

Depending on the type of extruder used, one can classify material extrusion additive manufacturing into different types shown in Fig. 1. Shaping, dibinding, sintering (SDS) processing basics is illustrated in Fig. 2

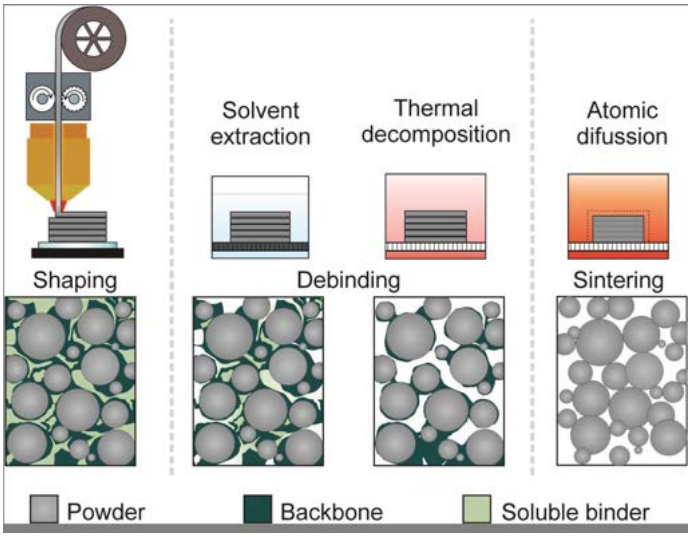


Figure 2. Schematic representation of the shaping, debinding, and sintering (SDS) process and respective morphology of the parts for the fabrication of metal, ceramic, or metal-ceramic.

## 2 Dependence of material properties on structure

The complexity of the inter-dependencies in the additive manufacturing of metals is illustrated in Fig. 3.

Some guidelines can be elucidated from earlier experience. For example, PIM utilizes particles with an average size between 5 to 15 $\mu$m. Typical mean particle sizes in ceramic CIM are 1 to 2 $\mu$m, but also submicron or nano sizes are used in advanced CIM (ceramic injection molding). Changing the characteristics of the powder can drastically influence the mechanical and flow properties of the feedstock materials, as has been reported in the PIM and the particulate composite literature [48, 86].

For example, Kukla et al. [57] reported that increasing the average particle size (from 5.5 to 8.6 $\mu$m) of round steel particles (316L) used in the filament, while maintaining all parameters constant, can lead to unprintable filaments. The increase in the average particle size resulted in the decrease of apparent viscosity and secant modulus of the filaments by ca. 42% and elongation at break by ca. 35%. More generally, particle size distribution is a property not dependent on other parameters, but the team points out that several issues and limitations can occur. For good flow, the PSD must be narrow and for a bulkier density, there must be wide distribution.

Another example of the effect of particle size distribution and sintering temperature is provided in [64] for alloy 625, see Fig. 4. It can be seen from the figure that broadening the particle size distribution and increasing sintering temperature towards limiting value of melting

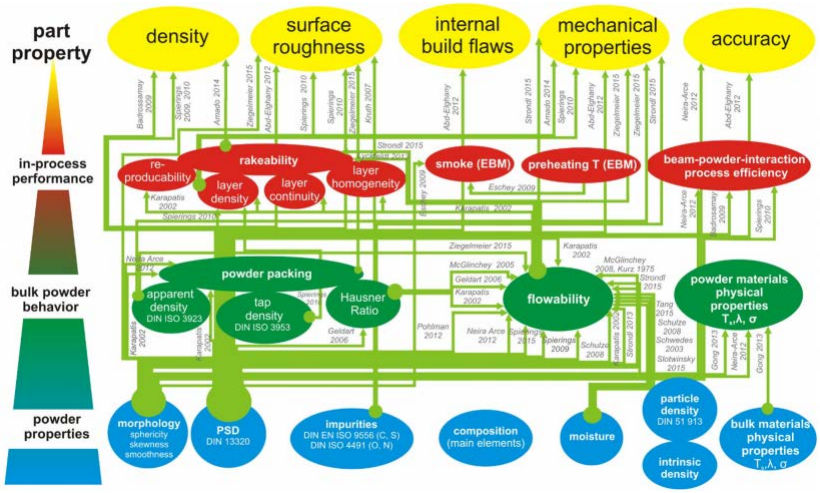


Figure 3. Visualization of the relationships between powder properties, bulk powder behavior, powder performance in process and finally the manufactured part quality as elaborated by different research groups [87].

point reduces the porosity of sintered samples.

"From the large amount of observed correlations between PSD and other process relevant aspects as well as final part quality reviewed above, it is clear that PSD is an important powder characteristic and has to be carefully tailored," states the research team. "However, it is not a parameter which can be used without additional information to decide how the powder will behave in the process."

The powder content in the filament has also been investigated. Gonzalez -Gutierrez et al. [42] characterized feedstocks and filaments with different contents of $Fe_{12}O_{19}Sr$. It was observed that increasing the content from 55 to 60 vol % made the filaments significantly less ductile (i.e ., shorter strain-stress curve); however, the stiffness remained almost unchanged. The filaments with the highest powder content had to be fed manually and even the printed parts were easily broken if not handled properly during the removal from the building platform.

The critical stress was considered to be approximately equal to the filament buckling stress by Euler's criterion. This criterion depends on the geometry of the filament, the elastic modulus (E), and the length between the feeding rollers and the liquefier unit (L). If the filament is a cylinder with radius R, then the critical stress ($\sigma_{cr}$) can be calculated as:

$$\sigma_{cr} \approx \sigma_E = \frac{\pi^2 E}{4(L/R)^2} \tag{1}$$

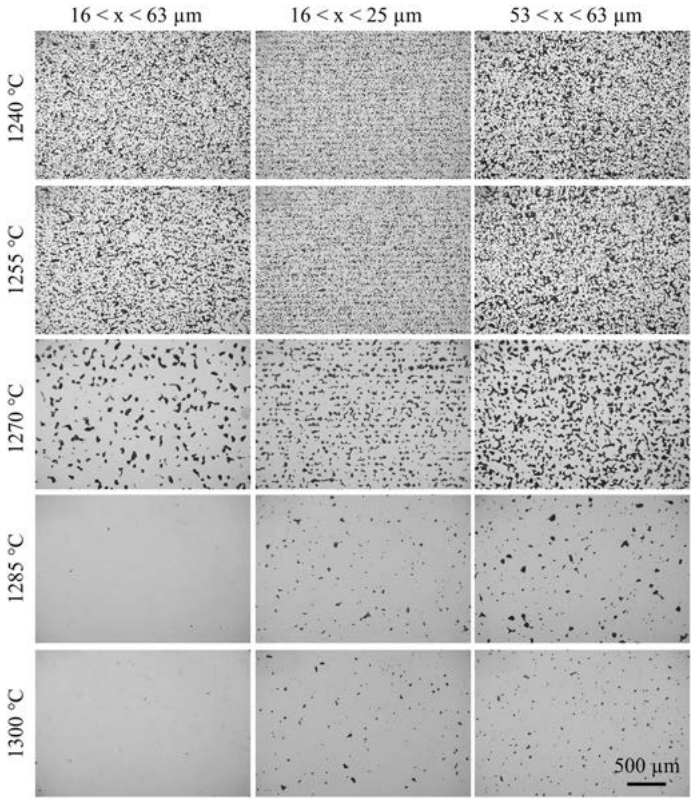


Figure 4. Optical micrographs of the BJ3DP alloy 625 samples sintered at different temperatures for 4 h. [64]

## 2.1 Dependence on processing parameters - preprocessing

It was observed that increasing the temperature of extrusion, bed, and/or envelope improves the adhesion between adjacent strands and as such the mechanical properties. In general, decreasing the layer thickness improves the mechanical properties of a built part, but it was found that a certain threshold is needed to avoid over-compression of the deposited strand, which negatively affects the mechanical properties.

It is very important to produce filaments with tight tolerances on the diameter, because the rate, based on the assumption that the filament has a constant diameter. Also, the filaments should be as round as possible. In order to produce filaments with constant dimensions and roundness, the extruder is coupled with a conveyor belt or a haul off unit that pulls away the filament, which is finally spooled in a winding unit. The filament's diameter and roundness need to be monitored with laser micrometers.

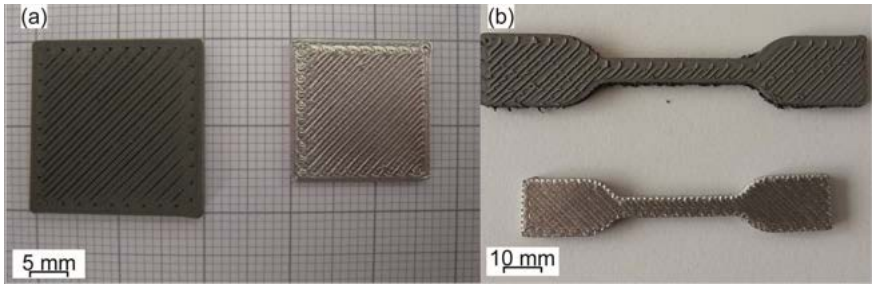


Figure 5. Comparison of printed and sintered parts: (a) 316L [56] and (b) 17-4PH steels [43].

## 2.2 Post-processing surface treatment

Grinding, sandblasting, low power laser surface treatment 25 s each improve surface properties.

## 2.3 Debinding

Binder removal is one of the most critical steps in the SDS process. The most common way to remove the binder from the shaped/printed parts is to heat the binder so it melts and flows out of the part and/or the binder is thermally degraded and diffuses out of the shaped part.

Another way to remove the binder system is to use first a solvent extraction step in a special solvent debinding unit, followed by a thermal debinding step in the same furnace where sintering will take place.

The Austrian company EVO-tech GmbH in collaboration with BASF SE offers filaments for MEAM that can be catalytically debound. The catalytic debinding process focuses on a solid-to-vapor catalytic degradation of the main binder component. This results in a much faster binder removal when compared to thermal or solvent debinding [44].

## 2.4 Sintering

Sintering is performed at temperatures below the melting temperature of the major constituent in the powder, generally within 70 to 90% of the powder's melting point [44]. It is important to mention that the shrinkage is anisotropic [16].

Besides polymer orientation, in MEAM-HP[1], shrinkage and density can be influenced by the presence of gaps between deposited strands. The more gaps, the larger the shrinkage and the lower the density of the sintered parts, since larger gaps cannot be closed during sintering [16]. The shrinkage can also be affected by the orientation of the filler particles, as discussed by Kukla et al. [55].

[1] material extrusion additive manufacturing of highly-filled polymers

Anisotropic shrinkage should be included in the CAD design of the parts for the MEAM of ceramics and metals, and the printing strategy needs to be considered and optimized to prevent excessive variation in the shrinkage.

One advantage of using MEAM as a shaping technology is that multi-material parts can be easily fabricated compared to powder bed technologies or vat photopolymerization. Recently, the possibility of producing parts made of 17-4PH steel and zirconia via MEAM-HP has been demonstrated [79]. Zirconia has an average particle size around 0.6 $\mu$m, while this steel has an average size around 20 $\mu$m. In order to increase the sintering activity the steel powder was re-shaped by attrition milling and ball milling. Also, after the milling, the initially spherical steel particles became irregular and angularly shaped; thus, the packing of the steel powder was changed and the overall sintering behavior became comparable between zirconia and steel [79].

In this work we focus on the nonlinear shrinkage problem in bound metal additive manufacturing of Ti6Al4V alloys for space applications. The report is organized as follows. In the next part we briefly discuss problem formulation and provide estimations of nonlinear shrinkage using knowledge of packing densities of spherical particles. Molecular dynamic simulations at the scale of tens of nanometers and a few nanoseconds are discussed in Part III. Results if the phase-field modeling of the micro-structure evolution in the filament cross-section are considered in Part IV. Application of discrete element model for analysis of initial shrinkage and particle re-arrangement at the scale of a few millimeters and several minutes is discussed in Part V. Finite element modeling of shrinkage in green, brown and metal parts is analyzed in details in Part VI. A novel concept of intelligent additive manufacturing in space is proposed in Part VII. Finally, conclusions are drawn in the last section of report.

# Part II
# Preliminary estimations

## 1 Problem formulation

In this project we are focused on a specific issue - nonlinear shrinkage of the printed parts. An example of the nonlinear shrinkage is shown in Fig. 6

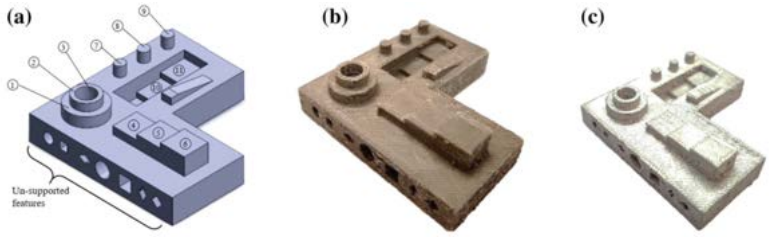


Figure 6. Example of nonlinear shrinkage for NIST standard item designed to test additive manufacturing.

The results of shrinkage measurements for the NIST test item are shown in Fig. 7

**Table II. Shrinkage of artifact part**

| | Shrinkage | |
|---|---|---|
| **FOI** | ***x–y*** | ***z*** |
| #1 | 14% | 23% |
| #2 | 18% | 20% |
| #3 | 18% | – |
| #4 | 13% | 22% |
| #5 | 16% | 22% |
| #6 | 17% | 19% |
| #7 | 13% | 23% |
| #8 | 13% | 23% |
| #9 | 13% | 23% |
| #10 | – | 18% |
| #11 | – | 15% |

Figure 7. The results of experimental estimation of nonlinear shrinkage in NIST test item [40].

The main problem is to reveal sources of nonlinear shrinkage and to propose methods that may alleviate the nonlinearity.

The Fig. 7 provides important insight into the actual scale of the nonlinearity. The first thing to notice is that major nonlinearity comes

from comparison of shrinkage in vertical ($z$) and horizontal ($x-y$) directions. Secondly, we notice that shrinkage in $x-y$ direction is uniform. These features together with the values of shrinkage are very important for further analysis as will be discussed in the Secs. 2 and 3.

## 2 Phenomena affecting nonlinear shrinkage

There are several phenomena that affect noninear shrinkage in bound metal deposition, including

- Particle size, material, size distribution, packing density;
- filament size, orientation, and filling density;
- geometry of the part, e.g. sharp corners, wall proximity;
- gravity;
- debinding process;
- temperature protocol

to mention a few of the most notable phenomena.

### 2.1 Particle distribution

Particles size and distribution have profound effects on the shrinkage that depends significantly on the initial density of the green sample and the presence of gravity force. An important insight into possible shrinkage effect can be gained by considering packing models available for initial configuration, see Table 1.

Table 1. Parameters of some packing models

| **Model** | **Description** | **Void fraction** | **Packing density** |
|---|---|---|---|
| Thinnest regular packing | cubic lattice (Coordination number 6) | 0.4764 | 0.5236 |
| Very loose random packing | E.g., spheres slowly settled | 0.44 | 0.56 (FILAMENTS) |
| Loose random packing | E.g., dropped into bed or packed by hand | 0.40 to 0.41 | 0.59 to 0.60 |
| Poured random packing | Spheres poured into bed | 0.375 to 0.391 | 0.609 to 0.625 (HIGH DENSITY) |
| Close random packing | E.g., the bed vibrated | 0.359 to 0.375 | 0.625 to 0.641 |
| Closet packing BCC | Coordination 8; 2 atoms per unit cell | 0.32 | 0.68 |
| Densest regular packing | fcc or hcp lattice (Coordination number 12) | 0.2595 | 0.7405 |

To see how data in the Table 1 can explain experimental results shown in the Fig. 7 we note first that the highest experimentally observed density of close random packing is 64%. This means that the

final density of the sample is 100 % and shrinkage is uniform in all 3 dimensions (as expected in an ideal sintering process) the observed value of linear shrinkage will be 14 %.

If the initial density is 45% the expected maximum linear shrinkage is ∼23 %. We note next that these are the values of shrinkage that are observed experimentally and shown in Fig. 7.

Next, we notice that shrinkage in $z$-direction corresponds to initial density ∼45%, while in $x$ and $y$ directions it corresponds to ∼64%. This observation of nonuniform shrinkage can be explained as follows.

If the original packing density is ∼45% there remains significant gaps between particles. This situation can be exemplified by considering HCP lattice shown in Fig. 8. The maximum packing density in this lattice is ∼75%, see last row in the Table 1. An approximation to a very loose packing of unsettled shperes with density ∼45% can be obtained by randomly shrinking radius of each sphere by 15% on average and by randomly shifting the center of these spheres by the difference between initial and final radii.

As a result the debinding stage of sintering in the gravity field will force spheres to settle in $z$-direction (direction of the gravity vector). I.e. the sample will shrink in $z$-direction by ∼ 10-11% due to the settling in the gravity, while it will rtain its size in $x$- and $y$- directions.

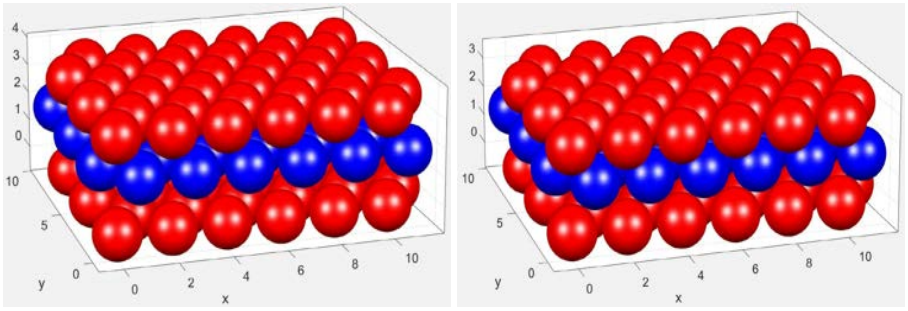


Figure 8. Nonlinear shrinkage of the HCP lattice in gravity. (left) initial configuration of the HCP lattice with density reduced to 0.45 by shrinking radii of the spheres. (right) Final configuration after settling spheres in vertical direction.

The settling can be seen in the Fig. 8 (right) by noticing the reduced distance between spheres in vertical direction and change in the vertical scale from 4 to 3.

When the spheres in the sample are settled it shrinks uniformly in all directions from initial settled density $\lesssim$0.64 to the final denisty $\lesssim$1. This will result in additional shrinkage in all the directions by ∼13%. Therefore we see that in the presence of the gravity the shrikage will be nonuniform: ∼23% in $z$-direction and ∼13% in $x$- and $y$- directions.

Thus preliminary estimations of the shrinkage based on the analysis of the known packing densities of spherical particles (shown in

the Table 1) provide deep insight into experimentally measured [40] anisotropic shrinkage of green parts in the gravity field. At the same time we note that there are instances of the parts features such as 2, 3,5, and 6 that demonstrate increased shrinkage in $x$- and $y$-directions that cannot be explained within ths simple framework. In addition we note that the shrinkage distortion in the gravity and microgravity can be much more intrigue and difficult to explain as we will discuss in the next section.

## 2.2 Gravity effect on sintering

Gravity is one of the main sources of the shape distortion during sintering on the ground.

"In space the rules of sintering change," said Rand German, principal investigator for the investigation titled NASA Sample Cartridge Assembly-Gravitational Effects on Distortion in Sintering. "The first time someone tries to do sintering in a different gravitational environment beyond Earth or even microgravity, they may be in for a surprise. There just aren't enough trials yet to tell us what the outcome could be. **Ultimately we have to be empirical, give it a try, and see what happens.**"

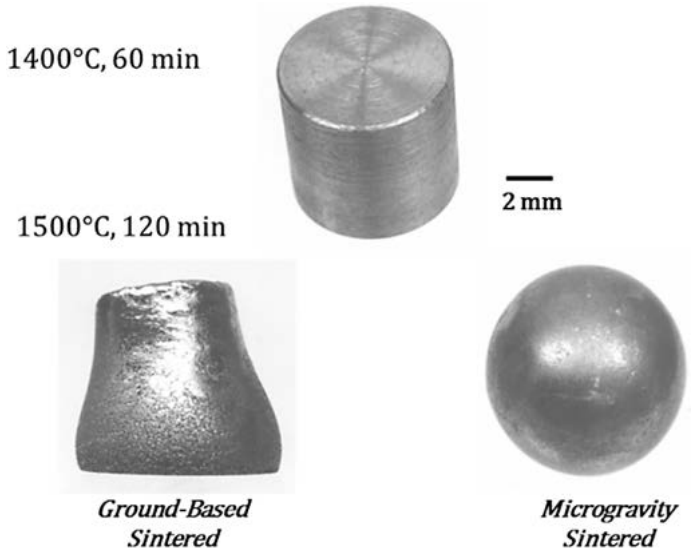


Figure 9. Comparative pictures prior to sintering and after sintering in the same conditions with and without gravity.

An example of the sintering trajectory difference is captured in Fig. 9. This image compares the pre-sintered compact (top center) with the shape after sintering at 1500 °C for 120 minutes in ground (lower left) and microgravity (lower right) conditions for 83W-12Ni-5Fe. The microgravity sample was less dense and more distorted. [36]

Thus we see that in micro-gravity sintering process may result in significant distortion of the shape that goes beyond nonlinear shrinkage.

## 3 Example of shrinkage estimations

Here we provide more detailed discussion of the shrinkage estimation in samples depending on the initial porosity of the powder and filament density.

In this example we consider cylindrical sample (with radius of the base 0.5 cm, height 1.27 cm, and volume 1 $cm^3$) fabricated using filaments with either low 0.55 to 0.59 or high 0.61 to 0.63 the powder loading. It is further assumed that filling density of the filaments is ranging from 0.85 for low to 0.9 for high density loading. We note that shrinkage has two main stages:

1. initial debinding stage when packing density can increase (without necking) to 0.6 - 0.62 due to the gravity and "poured" random

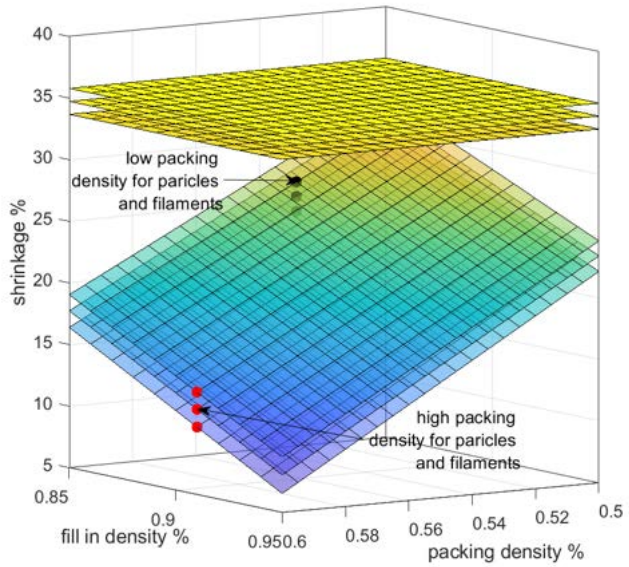


Figure 10. Predictions of parametric two stages shrinkage based on known properties of particles packing. Three lower planes show shrinkage of the cylinder height as a function of particles packing and feedstock filling density for three different intermediate densities: 61, 62, and 63 %. The top three planes show second stage of uniform volumetric shrinkage of these samples during sintering from intermediate to the final density 97%.

packing; initial shrinkage occurs mainly in the direction of gravity;

2. final stage of uniform shrinkage of densified sample final density can approach 80 to 97 %.

In the first stage it is assumed that radius does not shrink (since there is no necking process) while height is shrinking due to the action of the gravity forces, see also Sec. 2.4 for further illustration of this point. The three lower surfaces in the figure show volumetric shrinkage of the sample, since the radius of the cylinder is assumed to be constant during the 1-st stage the volumetric shrinkage also corresponds to the linear shrinkage of cylinder height. The three sheets correspond to the values of intermediate sample density 61, 62, and 63 %. The larger intermediate density the larger the shrinkage.

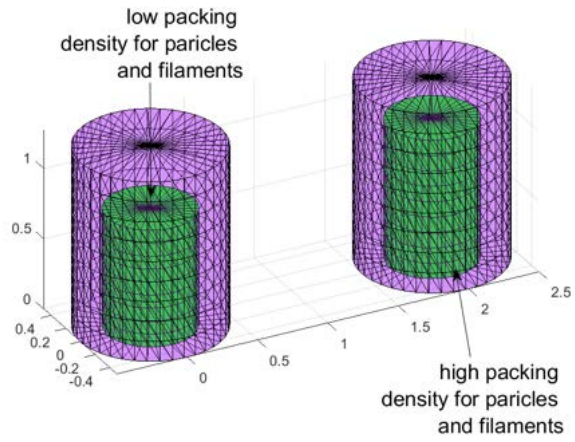


Figure 11. The shrikage of the initial cylinder (transparent faces shaded pink) corresponding to low (left) and high (right) densities of the powder and filament. Final cylinders are shaded by green color and correspond to porosity 3%. Axis show actual dimension in cm.

The top three surfaces correspond to the uniform volumetric shrinkage of the samples from the intermediate to final density ~97%. The total shrinkage corresponds to the sum of shrinkage in the 1-st and 2-nd stage. The dots indicate values with low and high packing and filling densities. The resulting shrinkage of the initial cylinder for the location of the dots is shown in Fig. 11. The overall shrinkage of the initial cylinder on both cases is shown in Fig. 11. It can be seen from the figure that shrinkage of the high density sample is smaller and substantially more uniform.

Preliminary conclusion of this section is that samples with high initial density (~ 62-64 %) are expected to demonstrate better printability and are less affected by the nonlinear shrinkage.

## 4 Methods of numerical analysis of shrinkage

For quantitative physics-based estimations of shrinkage we have to develop multi-scale modeling approach. The required scales naturally follow from the analysis of the process (see Fig. 3) and span from atomistic scale to the whole part dimensions. There are several numerical methods that are used to model sintering process including

- Molecular dynamics;
- Discrete element modeling;
- Phase field methods;
- Kinetic Monte Carlo simulations;
- Finite Element modeling.

All these methods have their own advantages and disadvantages and will be used to estimate the key parameters of shrinkage at different scales. Importantly, these methods are interconnected and parameters estimated at one scale are used as input parameters at the next scale.In this work we will estimate performance of these methods and develop a unique multi-scale approach the combines their individual strengths. To further improve accuracy and reliability of predictions of printability and nonlinear shrinkage we propose concept of intelligent additive manufacturing in space that blends physics-based and data-driven methods.

# Part III
# Molecular dynamics of sintering

## 1 Molecular Dynamics

At the initial stage of sintering the neck growth occurs due to several diffusion mechanisms [73] including: (i) Surface diffusion; (ii) Lattice diffusion; (iii) Evaporation and condensation from the particle surface; (iv) grain boundary diffusion; (v) lattice diffusion from the grain boundary; and (vi) plastic flow.

Various mechanisms of diffusion can be analyzed using MD simulations

Sintering occurs via two coupled major mechanisms of atomic diffusion: (i) diffusion at the grain boundary; and (ii) diffusion at the surface. The driving force for these two mechanisms is the gradient of the chemical potential: (i) at the grain boundary $\mu = \mu_0 - \sigma_n \Omega$; and (ii) at the surface $\mu = \mu_0 - \gamma_s \kappa \Omega$. Here $\mu_0$ is the standard chemical potential of the material, $\gamma_s$ is the surface energy, $\kappa = -2/r$ ($r$ is the sphere radius) is the surface curvature, and $\omega$ is the atomic volume. The positive normal stress on the surface $\gamma_s \kappa$ is tension and the negative one compression.

## 2 Molecular Dynamic simulations of sintering between 3 particles

### 2.1 Building Ti6Al4V particles in Atomsk and LAMMPS

To build nanoparticles of Ti6Al4V alloy we use free package Atomsk [49]. An example of the Atomsk script is shown in the List 1.

```
atomsk --create bcc 3.19 Ti -duplicate 100 100 100 ti_100_B.xsf
atomsk ti_100_B.xsf -select out sphere 0.5*box 0.5*box 0.5*box 100 -rmatom select Ti_sphere_100
    .cfg
atomsk .\Ti_sphere_100.cfg -select random 6\% Ti -substitute Ti Al Ti6Al_100_B.cfg
atomsk .\Ti6Al_100_B.cfg -select random 4\% Ti -substitute Ti V Ti6Al4V_100_B.cfg
atomsk Ti6Al4V_100_B.cfg -shift 55 0 0 .\Ti6Al4V_100RSp55_B.cfg
atomsk --merge x 2 .\Ti6Al4V_100RSp55_B.cfg .\Ti6Al4V_100RSm5_B.cfg Ti6Al4V_M1.cfg
atomsk --merge x 2 .\Ti6Al4V_100RSp55_B.cfg .\Ti6Al4V_100RSm50_B.cfg Ti6Al4V_M1.cfg
atomsk Ti6Al4V_M1.cfg lammps
```

Listing 1. Algorithm used to build Ti6Al4V particle with HCP (or BCC) lattice and diameter 20 nm.

The forces between atoms are calculated using the modified embedded atom method (MEAM) potential [20, 59]

$$E = \sum_i \left( F_i(\bar{\rho}_i + \frac{1}{2}\sum_{j\neq} \phi_{ij}(R_{ij})) \right), \qquad F(\bar{\rho}) = AE_c(\bar{\rho}/\bar{\rho}^0)\ln(\bar{\rho}/\bar{\rho}^0),$$
$$\bar{\rho}_i = \bar{\rho}_i^{(0)} G(\Gamma), \qquad G(\Gamma) = 2/(1+e^{-\Gamma}) \qquad \Gamma = \sum_{h=}^{3} t_i^{(h)} \left[ \rho_i^{(h)}/t_i^{(0)} \right]^2.$$
$$\rho_i^{a(h)}(R) = e^{-\beta^{(h)}(R/r_e - 1)}.$$

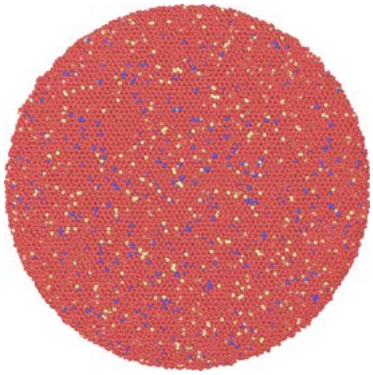

Figure 12. Resulting particle with HCP crystal structure ($\alpha$ phase) and diameter $D$ = 20 nm. Ti - red; Al - yellow; V - blue.

where $F$ is the embedding energy which is a function of the atomic electron density $\rho_i$ at the position of atom $i$, $\phi_{ij}$ and is a pair potential interaction, where the parameters $t_i^{(h)}$ are weight factors and the quantities $\rho(h)_i$ with $h = 0,...,3$, are partial electron densities, $E_c$ cohesive energy, $\bar{\rho}^0$ is the background electron density for the reference structure, $A$ is adjustable parameter, $R_{ij}$ is the distance to the $j$-th atom from the site $i$, $\beta^{(h)}$, the decay lengths are adjustable parameters and $r_e$ is the nearest-neighbor distance in the equilibrium reference structure.

Specific parameters of the MEAM potential used in this work are listed in the Table 2. The resulting particle of the Ti6Al4V alloy with HCP crystal structure is shown in Fig. 12.

Table 2. Parameters of the MEAM force field used in MD simulations.

| # elt<br># alpha<br># t0 | lat<br>b0<br>t1 | z<br>b1<br>t2 | ielement<br>b2<br>t3 | atwt<br>b3<br>rozero | alat<br>ibar | esub | asub |
|---|---|---|---|---|---|---|---|
| Al<br>4.975<br>1 | fcc<br>3.2<br>3.05 | 12<br>2.6<br>0.51 | 13<br>6<br>7.75 | 26.9815<br>2.6<br>1 | 4.05<br>0 | 3.36 | 1.16 |
| V<br>4.89<br>1 | bcc<br>4.74<br>1.7 | 8<br>1<br>2.8 | 23<br>2.5<br>-1.6 | 50.942<br>1<br>1 | 3.04<br>0 | 5.3 | 1 |
| Ti<br>5.03<br>1 | hcp<br>2.7<br>6.8 | 12<br>1<br>-2 | 22<br>3<br>-12 | 47.867<br>1<br>1 | 2.95<br>0 | 4.87 | 0.66 |

## 2.2 Sintering of 3 particles 16-12-14 nm

The results of sintering of three particles with hcp crystal structure, diameters 16, 12, and 14 nm and temperature $T$ = 1200 K are shown in

Fig. 13.

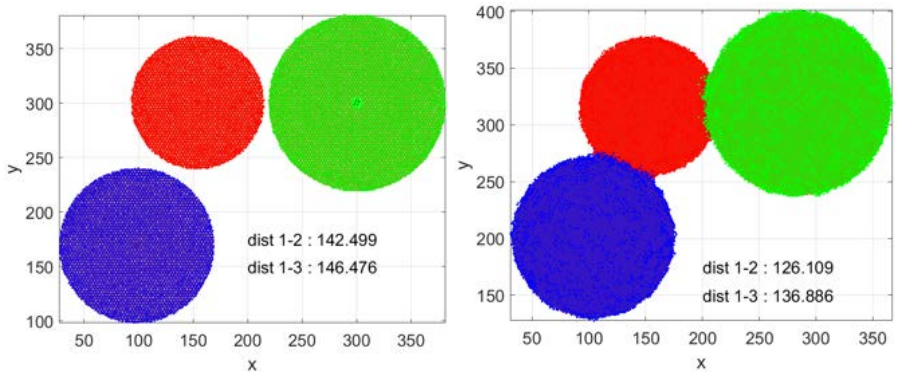


Figure 13. Initial (left) and final (right) states of sintering of 3 particle with HCP crystal structure ($\alpha$ phase) during 50 ps. Particle's diameter: 12 (red dots, 1-st particle), 14 (blue dots, 2-nd), and 16 (green dots, 3-rd) nm. Orange circle in the background of each particles indicates its original size. The distance between particles is shown by text.

The pairwise distance between the particles as a function of time is shown in Fig. 14. The initial stage of sintering during the first two picoseconds can be clearly identified in the figure. During this stage the particles that are initially separated by the distance of the order 10 Å (edge-to-edge shortest distance) are attracted to each other by the van der Waals forces [35].

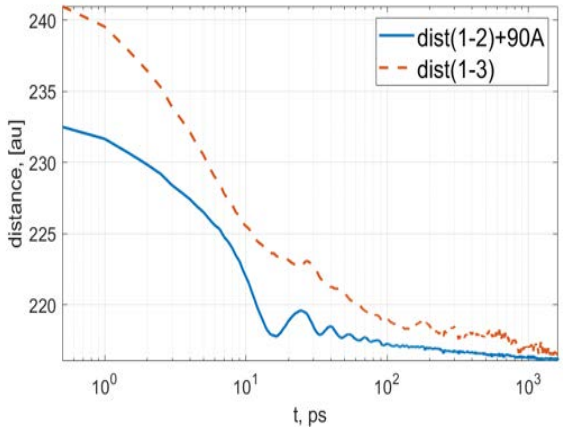


Figure 14. Distances between particles 1-2 and 1-3 as a function of time.

Since the initial velocity of the particles is zero the obtained results allow one to estimate the value of the Van der Waals forces, see next section for analysis of two particles.

## 2.3 Analysis of diffusion

In this section we analyze the diffusion of atoms at the interface between two particles with bcc crystal structure, diameter 24 nm and temperature 1300 K. The details of the simulations are shown in Fig. 15. In the top figure the atoms of two different particles are shown by blue and red colors and the interface is shown by the vertical dashed line.

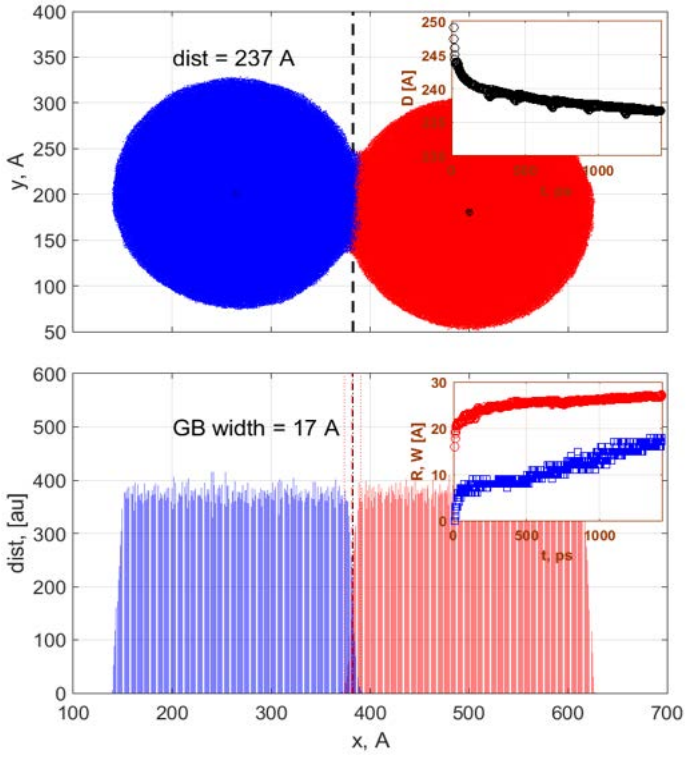


Figure 15. (top) Two interacting particles with the interface shown by the vertical dashed line. The inset shows distance as a function of time. (bottom) Distribution of titanium atoms in two particles along $x$ coordinate within cylinder with radius 50 Å and axis passing through the centers of both particles. The interface between particles is shown by the vertical dashed line. The inset illustrates the grain boundary width (blue squares) and neck radius (red circles) as a function of time.

The location of the titanium atoms at the boundary layer after 1 ns of simulation time is shown in Fig. 16 (bottom). To analyze statistics of the diffusion process we track the location of these atoms back in time using "prehistory approach" [60]. The initial locations of the Ti atoms that form grain boundary structure is shown in Fig. 16 (top).

The drift and diffusion coefficients of the atoms were calculated using standard approach [50]. In our case we follow trajectories of $N_{t1} = 3460$ and $N_{t2} = 4450$ Ti atoms within the left and right particle correspondingly (see Fig. 15). These trajectories are shown in Fig. 17. Each

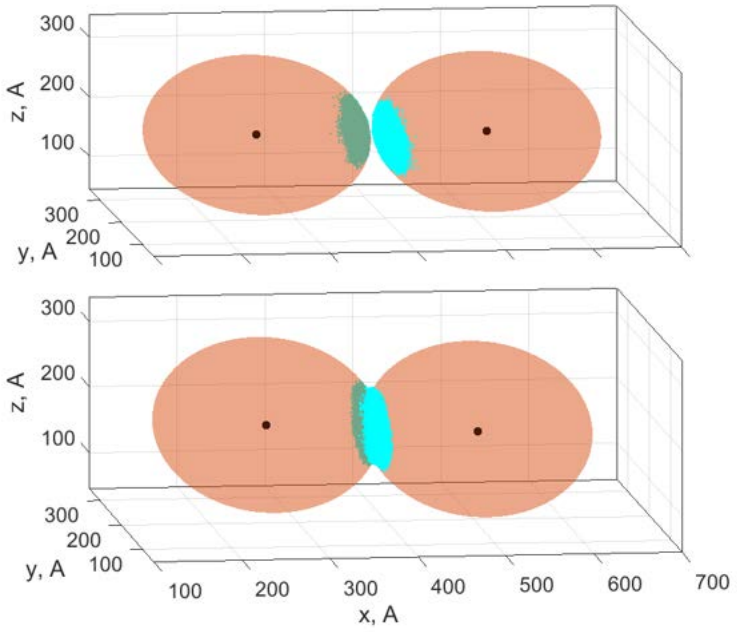


Figure 16. (top) Two spheres indicating location of two metal particles with centers indicated by black dots. Cyan points indicate location of Ti atoms that form boundary layer at 1 ns. (bottom) Distribution of titanium atoms in the boundary layer between two particles after 1 ns of simulations.

trajectory $\{r^i(t_1),...,r^i(t_{Ns})\}$ has length $N_s = 2300$ and sampling times $t_j$ with time step $\Delta t = 0.4$ ps.

According to the approach [50] the drift velocities ($\{a_x, a_y, a_z\}$) is found as

$$a_\alpha \approx \frac{1}{Nt} \sum_{i=1}^{Nt} \sum_{j=1}^{N_s-1} \frac{\alpha^i_{j+1} - \alpha^i_j}{\Delta t} \tag{2}$$

where $\alpha \in \{x, y, x\}$.

Similarly, the diffusion matrix $D_{\alpha\beta}$ where $\alpha, \beta \in \{x, y, z\}$

$$D_{\alpha\beta} \approx \frac{1}{Nt} \sum_{i=1}^{N_t} \sum_{j=1}^{N_s-1} \frac{(\alpha^i_{j+1} - \alpha^i_j)(\beta^i_{j+1} - \beta^i_j)}{2\Delta t}. \tag{3}$$

We note that the equations (2) and (3) correspond to the values of drift and diffusion averaged in time over the atom trajectories that form the grain boundary at 1ns and therefore should be considered as an order of magnitude estimates.

It appears that MD simulations largely overestimate drift coefficient as $a \approx 70$ mm/sec while providing reasonable values for the diffusion

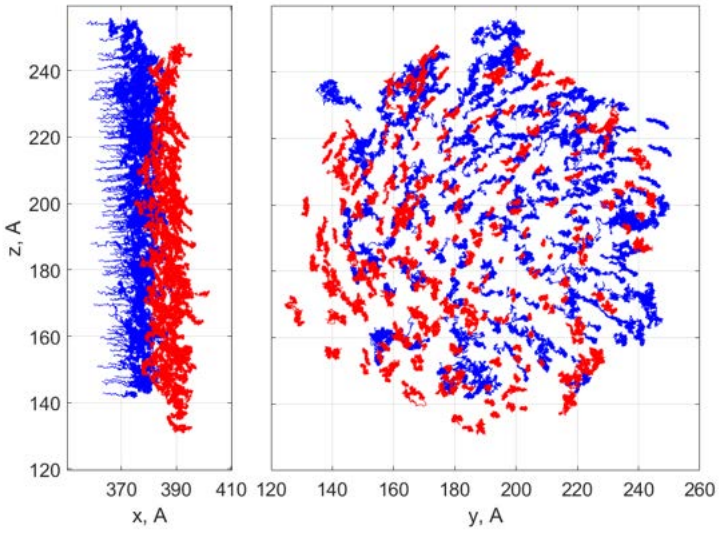


Figure 17. (left) XZ-view of trajectories of Ti atoms within the grain boundary layer after 1 ns of simulations. (right) YZ-view of the same trajectories. Color codding is the same as in the Fig. 15: red trajectories belong to the right particle while blue correspond to the left particle.

coefficient providing values ranging from $D_{surf} \approx 8 \times 10^{-10}$ m$^2$/sec to $\approx 1.6 \times 10^{-9}$ m$^2$/sec.

Importantly, MD simulations provide estimation for another key quantity of the system – namely grain boundary width $\delta_{gb}$ that will be used below to estimate sintering stress and sintering time in the phase-field model. It can be seen from the Fig. 15 that the $\delta_{gb}$ depends on time and quickly becomes $\geq 10$ Å after approximately 0.5 ns of simulations of the particles with diameter $D = 24$ nm.

It can also be seen clearly that the width of the grain boundary is tightly related to the geometry of the neck and can be expected to scale nearly linearly with the radius of the particle, see e.g. Fig. 18. Therefore we may well expect that the value of the $\delta_{gb}$ is of the order of 1.0 µm.

The later observation may clarify the situation in the phase field modeling of sintering. In the latter theory (see below) it is often assumed that the actual value of the $\delta_{gb}$ is $\approx 1.0$ Å. But this value is not suitable for phase-field simulations and therefore it is re-scaled to 1.0 µm under assumption that such re-scaling does not change the dynamics of the model. However, this assumption is not correct and is not required because as we have shown above 1.0 µm is a natural value for the grain boundary width for the particles with diameter of the order of 30.0 µm.

We see that molecular dynamics can provide important insight into the mechanism of diffusion and estimate values of the diffusion coeffi-

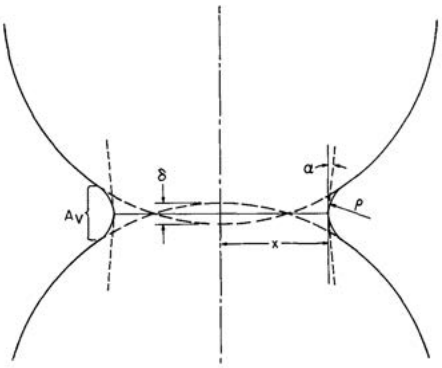


Figure 18. Sketch of neck geometry [51]. x is the neck radius, $A_v$ is the effective area across which atoms arrive by diffusion, $\delta$ is the grain boundary width, $\rho$ is the minimum radius of the neck surface curvature, $\alpha$ is the groove angle [51].

cient and grain boundary width. However, at present it has a number of weaknesses mainly related to the limited computing power. The size of the particles is limited to 30 nm in diameter. Already for particles with diameter 24 nm studied in this work LAMMPS simulations take 285.293 hours/ns on 46 processors and remain unpractical for simulations of the order 100 ns. In addition, MD overestimates sintering rate by orders of magnitude giving values ~2.0 Å per ns or ~0.2 µm per 1 µs, which does not correspond to the experimental observations.

The main results of this section that will be used for the estimation of the sintering stress and micro-structure evolution include estimations of the grain boundary width ~1.0 µm and the fact that the key mechanism involved into the sintering is surface diffusion with coefficient $\sim D_{surf} \approx 12 \times 10^{-10}$ m$^2$/sec.

# Part IV
# Microstructure evolution

One of the most nontrivial issues in estimation of nonlinearity is related to formation and growth the of grains during sintering of metal particles [37]. An example of grain growth is shown in Fig. 19 where one could see slow increase of the grains size from ~ 2 to ~ 20 mkm during 10 hours and correspopnding decrease of porosity.

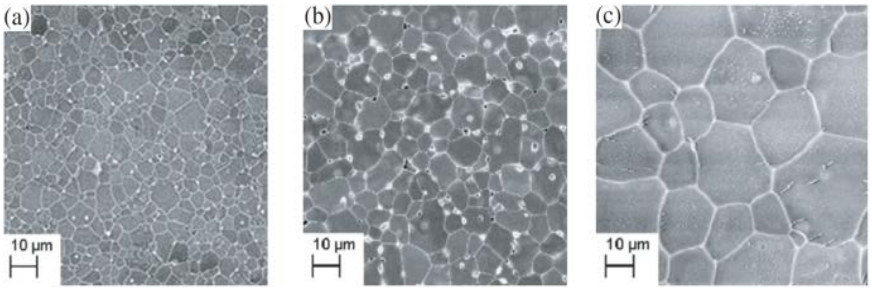


Figure 19. Scanning electron microscopy images of as-received and annealed samples: (a) as received, (b) annealed at 1600 °C for 5 h and (c) annealed at 1600 °C for 10 h [17].

Even more nontrivial is the initial stage of sintering when round metal particles form contacts with neighbors and undergo the shape transformation from the spherical to dense grain structure. Further details of the sintering stages are shown in Fig. 20. Three distinct stages of sintering were identified: stage I when density redistribution occurs due to increase in concentration of particle at certain locations, stage II where densification happens as the particles compacts taking up the void spaces and finally, stage III in which further sintering results in particle size increases and grain growth over time.

Theoretically the total driving force for microstructure evolution is [70] the sum of two terms related to the growth of the grain boundary

| | Initial Stage | Intermediate Stage | Final Stage |
|---|---|---|---|
| neck size ratio, $X/D$ | <0.33 | 0.33 to 0.5 | >0.5 |
| coordination, $N_C$ | <7 | 8 to 12 | 12 to 14 |
| density, % | 60 to 66 | 66 to 92 | >92 |
| shrinkage, $\Delta L/L_O$ % | <3 | 3 to 13 | >13 |
| surface area, $S/S_O$ % | 100 to 50 | 50 to 10 | <10 |
| grain size ratio, $G/D$ | ≈1 | >1 | >>1 |
| pore size ratio, $d/G$ | <0.2 | near constant | shrinking |

$X$ = neck diameter, $D$ = particle diameter, $N_C$ = coordination number.
$\Delta L/L_O$ = sintering dimensional change over initial size, commonly termed shrinkage.
$S$ = specific surface area, $S_O$ = initial specific surface area prior to sintering.
$G$ = grain size, $G_O$ = starting grain size, $d$ = pore diameter.

Figure 20. Stages of sintering from [37]

and shrinkage of the grain surface area

$$\Delta F_\mu = \Delta A_{gb}\gamma_{gb} + \Delta A_s\gamma_s \tag{4}$$

where $dA_{gb}$ and $dA_s$ are the associated changes of the grain bounday area (positive at the initial stage of sintering) and of the surface area (always negative). Sintering process continues as long as $\Delta F_\mu$ remains negative.

At the initial stage of sintering the neck formation and reduction of the surface area is the main driving force of sintering. At the intermediate stage the neck and grain growth processes compete. And at the finale stage, the grain growth and pore migration towards sample surface dominate the sintering process, see the Figs. 19 and 20.

# 1 Sintering model

Currently the most popular and powerful approach to modeling microstructure evolution during sintering is based upon phase field (PF) theory. In the phase-field method [63], the microstructural evolution is analyzed by means of a set of phase-field variables that are continuous functions of time and spatial coordinates. A distinction is made between variables related to a conserved quantity and those related to a non-conserved quantity. Conserved variables are typically related to the local composition. Non-conserved variables usually contain information on the local (crystal) structure and orientation.

Order parameters and phase-fields are both non-conserved variables that are used to distinguish coexisting phases with a different structure. Order parameters refer to crystal symmetry relations between coexisting phases. Phase-fields are phenomenological variables used to indicate which phase is present at a particular position in the system.

In a system with $N$ components each having the number of moles $n_i$ ($i = 1 \ldots N$) the following conservative variables can be used [63]

$$x_i = \frac{n_i}{n_{tot}}, \quad c_i = \frac{n_i}{V} = \frac{x_i}{V_m}$$

where $n_{tot} = \sum n_i$ is the total number of moles in the system, $V_m$ the molar volume and $V$ the total volume of the system

$$\sum_{i=1}^{N} x_i = 1, \quad \sum_{i=1}^{N}{}_i = \frac{n_{tot}}{V} = \frac{1}{V_m}.$$

The free energy $F$ may consist [63] of bulk free energy $F_{bulk}$, interfacial energy $F_{int}$, elastic strain energy $F_{el}$, energy terms due to thermal field $F_{th}$ and external field $F_{ext}$

$$F = F_{bulk} + F_{int} + F_{el} + F_{th} + F_{ext}.$$

## 1.1 Phase-field equations

The Cahn-Hillard (CH) and Allen-Cahn (AC) phase field equations used to model dynamics of conservative and non-conservative variables respectively have the form

$$\begin{array}{rcl} \frac{\partial c_i}{\partial t} & = & \nabla \cdot M_i \nabla \left( \frac{\partial f_{\text{loc}}}{\partial c_i} + \frac{\partial E_d}{\partial c_i} - \kappa_{c,i} \nabla^2 c_i \right) \\ \frac{\partial \eta_j}{\partial t} & = & -L \left( \frac{\partial f_{\text{loc}}}{\partial \eta_j} + \frac{\partial E_d}{\partial \eta_j} - \kappa_{\eta,j} \nabla^2 \eta_j \right). \end{array} \tag{5}$$

The dimensions of the two equations are

$$\frac{1}{t} = \frac{l^3}{mol} \frac{1}{l} \frac{l^2 mol}{t \cdot e} \frac{1}{l} \left( \frac{e}{l^3} + \frac{e}{l^3} - \frac{e}{l} \frac{1}{l^2} \right)$$

and

$$\frac{1}{t} = - \frac{l^3}{e \cdot t} \left( \frac{e}{l^3} + \frac{e}{l^3} - \frac{e}{l} \frac{1}{l^2} \right)$$

for the CH and AC equations respectively.
And the equations for residues in the weak form are (note split form of the CH equation)

$$\mathcal{R}_{\mu_i} = \left( \frac{\partial c_i}{\partial t}, \psi_m \right) + (M_i \nabla \mu_i, \nabla \psi_m) - \left\langle M_i \nabla \mu_i \cdot \vec{n}, \psi_m \right\rangle$$

$$\mathcal{R}_{c_i} = (\nabla c_i, \nabla (\kappa_i \psi_m)) - \left\langle \nabla c_i \cdot \vec{n}, \kappa_i \psi_m \right\rangle + \left( \left( \frac{\partial f_{\text{loc}}}{\partial c_i} + \frac{\partial E_d}{\partial c_i} - \mu_i \right), \psi_m \right)$$

$$\mathcal{R}_{\eta_i} = \left( \frac{\partial \eta_j}{\partial t}, \psi_m \right) + \left( \nabla (\kappa_j \eta_j), \nabla (L \psi_m) \right) + L \left( \frac{\partial f_{\text{loc}}}{\partial \eta_j} + \frac{\partial E_d}{\partial \eta_j}, \psi_m \right)$$

Phase-field model of isothermal sintering of metal particles considers free energy of the system in the form [25, 97]

$$F = \int \left[ f_0(c, \eta) + f_{el}(c, \eta) + \frac{\kappa_c}{2} |\nabla c|^2 + \frac{\kappa_\eta}{2} \left| \nabla \eta \right|^2 \right] dV \tag{6}$$

Parameters in this equation can be modeled as follows. Internal phase-field free energy is

$$\begin{aligned} f_0(c, \eta_i) = A c^2 (1-c)^2 + B \Bigg[ & c^2 + 6(1-c) \sum_i \eta_i^2 \\ & -4(2-c) \sum_i \eta_i^3 + 3 \left( \sum_i \eta_i^2 \right)^2 \Bigg] = A h(c) + B g(c, \eta). \end{aligned} \tag{7}$$

Phase field free energy is shown in Fig. 21

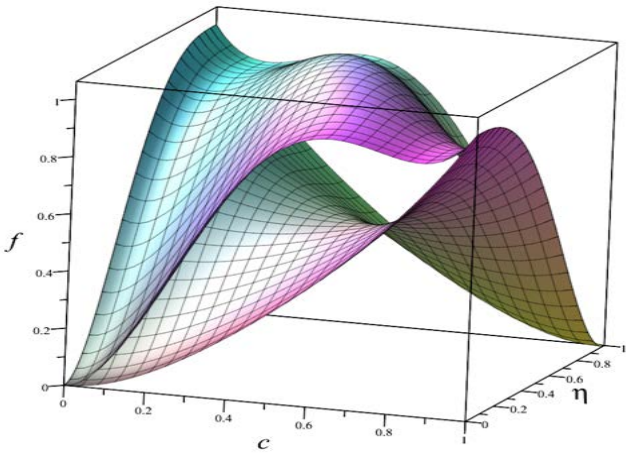


Figure 21. Chemical free energy as a function of concentration and order parameter for $B = 1$, $A = 1$ (bottom) and $A = 10$ (top) .

With units of $A$ and $B$ being $e/l^3$, the units of $L - l^3/(et)$, and the units of $M_i - (l^2 mol)/(et)$ (or $V_m M_i - (l^5)/(et)$), $\kappa_i$ and $\kappa_j$ are gradient energy coefficients with the units $e/l$.

$$M = \frac{V_m}{k_B T}\left[D_{vol}\phi(c) + D_{vap}\left[1-\phi(c)\right] + D_{surf}\, c\,(1-c) + D_{gb}\sum \eta_i \eta_j\right] \quad (8)$$

where $\phi(c) = c^3\left(10 - 15c + 6c^2\right)$ and the mobility coefficients $(M_i)$ are estimated from corresponding diffusion coefficients as

$$M_i = \frac{D_i V_m}{k_B T};$$

$$D_{\mathrm{gb}} = D_{gb0} e^{-\frac{Q_{\mathrm{gb}}}{k_B T}}; \quad D_{\mathrm{vol}} = D_{vol0} e^{-\frac{Q_{\mathrm{vol}}}{k_B T}}; \quad D_s = D_{s0} e^{-\frac{Q_s}{k_B T}}. \quad (9)$$

and

$$\kappa_c = \left(2\gamma_s - \gamma_{\mathrm{gb}}\right)\delta; \quad \kappa_\eta = \gamma_{\mathrm{gb}}\delta; \quad A = \frac{\left(12\gamma_s - 7\gamma_{\mathrm{gb}}\right)}{\delta}; \quad B = \frac{\gamma_{\mathrm{gb}}}{\delta}, \quad (10)$$

$\gamma_s$ and $\gamma_{\mathrm{gb}}$ are the surface and the grain boundary energy, $\delta$ is the interface width or the grain boundary thickness. The grain boundary width estimates usually varies between 0.5 - 2.0 nm. However, it was shown in the previous part $\delta_{gb}$ can be of the order of 1 µm.

## 2 Mechanics

The strong form of the governing equation on the domain $\Omega$ and boundary $\Gamma = \Gamma\iota i \cup \Gamma g i$ can be stated as follows:

$$\begin{aligned} &\nabla \cdot (\sigma + \sigma_0) + \mathbf{b} = \mathbf{0} \text{ in } \Omega \qquad \nabla \cdot \sigma = F/A = \left[\tfrac{1}{l} \cdot \tfrac{m \cdot l}{t^2 \cdot l^2}\right] \\ &\mathbf{u} = \mathbf{g} \text{ in } \Gamma_{\mathbf{g}} \\ &\sigma \cdot \mathbf{n} = \iota \text{ in } \Gamma_{\iota} \end{aligned} \tag{11}$$

$$\frac{m}{l^2 \cdot t^2} + \frac{1}{l^3}\frac{m \cdot l}{t^2} = 0$$

where $\sigma$ is the Cauchy stress tensor, $\sigma_0$ is an additional source of stress (such as pore pressure), $\mathbf{u}$ is the displacement vector, $\mathbf{b}$ is the body force per unit volume, $\mathbf{n}$ is the unit normal to the boundary, $\mathbf{g}$ is the prescribed displacement on the boundary and $\iota$ is the prescribed traction on the boundary. The weak form of the residual equation is expressed as:

$$\mathbb{R} = (\sigma + \sigma_0, \nabla\phi_m) - \langle \iota, \phi_m \rangle - (\mathbf{b}, \phi_m) = \mathbf{0},$$

where $(\cdot)$ and $\langle \cdot \rangle$ represent volume and boundary integrals, respectively. The solution of the residual equation with Newton's method requires the Jacobian of the residual equation, which can be expressed as (ignoring boundary terms)

$$\mathbb{J} = \left(\frac{\partial \sigma}{\partial \nabla \mathbf{u}}, \nabla\phi_m\right), \qquad \frac{m}{l^2 \cdot t^2}$$

assuming $\sigma_0$ is independent of the strain.

The material stress response is described by the constitutive model, where the stress is determined as a function of the strain, i.e. $\sigma \sim (\epsilon - \epsilon_0)$, where $\epsilon$ is the strain and $\epsilon_0$ is a stress free strain. For example, in linear elasticity (only valid for small strains), the material response is linear, i.e. $\sigma = \mathbf{C}(\epsilon - \epsilon_0)$. The tensor mechanics system can handle linear elasticity and finite strain mechanics, including both elasticity and plasticity.

## 3 Thermal model and Boundary Conditions

$$\rho \frac{\partial C_p \, \mathrm{T}}{\partial t} = \nabla (k_e \, \nabla T) \qquad k_e = k\,(1 - \theta)^p$$

$$T\,(x, y, z, 0) = T_0$$

In the present study we use isothermal conditions and thermal conductivity was only briefly tested in simulations.

We use mostly periodic boundary conditions.

# 4 Non-dimensional equations

An example of the parameter values used by Biswas et al [25] for tungsten, by Zhang [97] for Ti and Ni, by Wang [91] for TiAlV alloy, and by Ahmed [17] for $CeO_2$ are provided in this section, see also Sec. B in the Appendix. The non-dimensional phase field equations are derived following results reported in [18, 81].

Consider equations of the phase field (5) with $f_0$ given by (7) and parameters given by (9) and (10). If the energy normalization constant is taken as $B$, cf [18], the resulting set of equations takes form

$$\begin{aligned}\frac{\partial c}{\partial t} &= \nabla\cdot(M\cdot B)\nabla\left(\frac{\partial}{\partial c}\left[\frac{\left(12\gamma_s-7\gamma_{gb}\right)}{\gamma_{gb}}h(c)+g(c,\eta)\right]+\frac{\partial E_d/B}{\partial c_i}-\frac{\left(2\gamma_s-\gamma_{gb}\right)}{\gamma_{gb}}\delta^2\nabla^2 c_i\right)\\ \frac{\partial \eta_j}{\partial t} &= -(L\cdot B)\left(\frac{\partial}{\partial \eta_j}g(c,\eta)+\frac{\partial E_d/B}{\partial \eta_j}-\frac{\gamma_{\mathrm{gb}}}{\gamma_{gb}}\delta^2\nabla^2\eta_j)\right).\end{aligned} \tag{12}$$

Several important features can be seen in set of equations (12). First we notice that the overall decay of the total free energy – which is the driving force of shrinkage process – is governed by the transformation of the total surface area of the particles into the grain boundary area. During initial stage of the neck formation the resulting grain boundary area is approximately twice smaller than the initial surface area at the neck. Therefore, only when the surface energy is larger than one half the GB energy there is a thermodynamic driving force for sintering [46].

As we will see in the next sections this condition always holds for the materials in question. We also note that the values of the surface and grain boundary energies are of the order of 1 J/m$^2$ while the boundary layer width is of the order 1 $\mu$m. These two values set the characteristic dimensions of the problem parameters. In particular, we see that $\gamma_s \sim 2$ J/m$^2$ and $\gamma_{gb} \sim 1$ J/m$^2$, see section B.3.

Resulting dimensional values of the model parameters $A \sim 15\times 10^9$ J/m$^3$, $B \sim 1\times 10^9$ J/m$^3$, $\kappa_c \sim 3\times 10^{-9}$ J/m, and $\kappa_\eta \sim 1\times 10^{-9}$ J/m.

There is, however, no consistency in values of phase-field mobility $L$ and intrinsic interface mobility $M_{gb}$. Meaningful results can be obtained by using the following values [91] $L \sim 3.6\times 10^{-9}$ m$^3$/(J$\cdot$ s) and intrinsic interface mobility $M_{gb} \sim 2.6\times 10^{-15}$ m$^4$/(J$\cdot$ s). The diffusion mobility $M$ is given by (8), where all the diffusion coefficients are usually found experimentally.

In addition, one has to take into account molar volume of Ti $V_m = 10.43$ cm$^3$/mol (or alternatively atomic volume $\Omega_m = V_m/N_A \sim 1.7\times 10^{-29}$ m$^3$) and the relation between $L$ and grain boundary mobility $M_{gb}$

$$L = \frac{4}{3}\frac{M_{gb}}{\delta_{gb}} \tag{13}$$

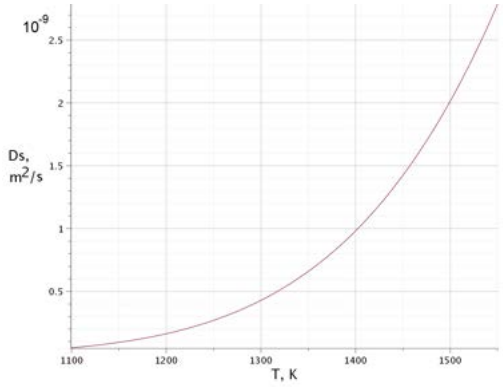


Figure 22. Temperature dependense of the surface diffusion.

and we see that values of $L$ and $M_{gb}$ differ by 6 orders of magnitude. This result is in accordance with the earlier obtained estimations (see Sec. 2.3) of $\delta_{gb} \sim 1.0\,\mu\text{m}$.

Next, we notice that the product $(L{\cdot}B)$ in the second line of (12) gives a natural time scale for the model $\tau_0 = 1/(L \cdot B)$. In which case the AC equation becomes

$$\frac{\partial \eta_j}{\partial t/\tau_0} = -\left( \frac{\partial}{\partial \eta_j} g(c,\eta) + \frac{\partial E_d}{B \partial \eta_j} - \frac{\gamma_{\text{gb}}}{\gamma_{gb}} \delta^2 \nabla^2 \eta_j) \right).$$

and the CH equation becomes

$$\frac{\tau_0 \partial c}{\partial t} = \nabla{\cdot}\left( \frac{D\Omega_m}{L k_B T} \right) \nabla \left( \frac{\partial}{\partial c} \left[ \frac{12\gamma_s - 7\gamma_{gb}}{\gamma_{gb}} h(c) + g(c,\eta) \right] + \frac{\partial E_d}{B \partial c_i} - \frac{2\gamma_s - \gamma_{gb}}{\gamma_{gb}} \delta^2 \nabla^2 c_i \right).$$

where

$$D = D_{vol}\phi(c) + D_{vap}\left[1 - \phi(c)\right] + D_{surf}\, c\,(1-c) + D_{gb} \sum \eta_i \eta_j$$

and $\phi(c) = c^3\left(10 - 15c + 6c^2\right)$. For further estimations we notice that $D$ is proportional to the largest diffusion coefficients $D_{vol}$, $D_{surf}$, $D_{vol}$, or $D_{gb}$. The largest diffusion coefficient is usually associated with surface diffusion and is of the order $10^{-9}$ m$^2$/s as was established earlier in this report. Note although that all the diffusion coefficients exponentially depend on the temperature, see (9) and Fig. 22. But for the range of temperatures of interest the surface diffusion value is approximately consant.

Finally, we notice that using nondimensional gradients in AC and CH equations leads to the following final nondimensional form

$$\frac{\partial \eta_j}{\partial t/\tau_0} = -\left( \frac{\partial}{\partial \eta_j} g(c,\eta) + \frac{\partial E_d/B}{\partial \eta_j} - \left( \frac{\delta}{l^*} \right)^2 \nabla^2 \eta_j) \right). \tag{14}$$

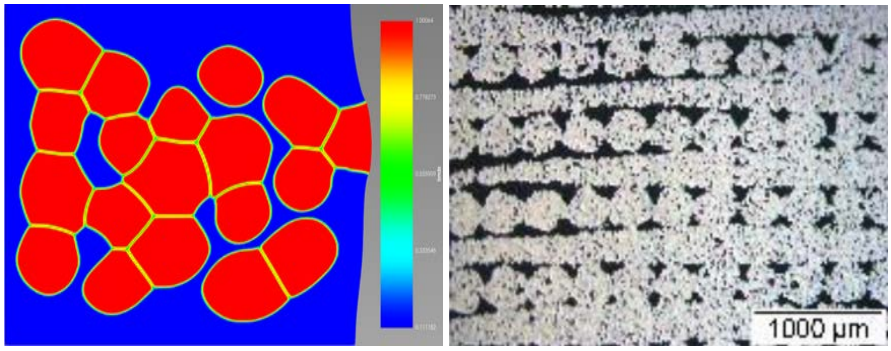


Figure 23. (left) Results of the simulations of the Phase Field model with reduced coefficients $\kappa_c$ and $\kappa_\eta$. (right) Experimental results of sintering with flow rate increased to 115 % as compared to nominal value.

$$\frac{\tau_0 \partial c}{\partial t} = \nabla \cdot \left( \frac{D V_m}{L k_B T l^{*2}} \right) \nabla \left( \frac{\partial}{\partial c} \left[ \frac{12\gamma_s - 7\gamma_{gb}}{\gamma_{gb}} h(c) + g(c,\eta) \right] + \frac{\partial E_d / B}{\partial c} - \frac{2\gamma_s - \gamma_{gb}}{\gamma_{gb}} \left( \frac{\delta}{l^*} \right)^2 \nabla^2 c \right). \tag{15}$$

**Length scale** This form of the nondimensional equations does not leave much freedom to choose parameters of the model. Indeed, the size of the 2D simulations region is of the order 100x100 pixels (it is even smaller in 3D) and it must correspond to $\sim 100{\times}100\,\mu m^2$ area. This gives us $l^* \sim 1.0\,\mu m$, because $l^*$ corresponds to the unit of mesh size. This means that to resolve the gradient of order parameters and of the concentration $c$ the value of $\delta$ has to be taken as $\sim$1.0 µm, which is 3 orders of magnitude larger than the nominal value of the grain boundary. However, as it was shown in the previous part $\delta_{gb} \sim 1.0\,\mu m$ is a natural length scale of the problem.

## 5 Dimensionless parameters

Only when the surface energy is larger than one half the GB energy is there a thermodynamic driving force for sintering since two surfaces are eliminated in the formation of a single GB. As a GB is formed at the neck of two particles, it reduces the free surface area while increasing the GB area, thus reducing the overall surface energy and increasing the overall GB energy [6].

```
[./constant_mat]
  type = GenericConstantMaterial
  block = 0
  prop_names = '  A    B   L   kappa_op kappa_c'
  prop_values = '16.0 1.0 1.0  0.5      1.0    '
[../]
```

Figure 24. Definition of dimensionless material parameters in phase-field model in MOOSE [25].

**Diffusion mobility** $M$ Consider now the discussed in the Partvalue of dimensionless diffusion mobility

$$\tilde{M} = \left(\frac{M}{Ll^{*2}}\right) = \left(\frac{DV_m}{Lk_BTl^{*2}}\right) = \left(\frac{3DV_m\delta_{gb}}{4M_{gb}k_BTl^{*2}}\right)$$

Thus the value of $\delta_{gb}$ is the key parameter that controls both the mesh size and the time scale of the model. There is no sufficient flexibility in the choice of this parameter. Its value has to be at least twice smaller than value of $\delta_{gb}$.

**Time scale** The time scale of the model can be chosen in a few different ways. Firstly, it can be taken as

$$\tau_0 = \frac{1}{L \cdot B} = \frac{3}{4}\frac{\delta_{gb}^2}{M_{gb} \cdot \gamma_{gb}}$$

to keep dimensionless value of the phase-field mobility $L \sim 1$, see lines in Fig. 24 from the MOOSE code that defines parameters in [25].

Note that this definition is not unique. There is a significant dispersion in the literature data on the $M_{gb}$ ranging from $10^{-8}$ [97] to $10^{-15}$ [91], which in turn leads to the dispersion of the phase-field diffusion parameter $L$ via (13). $M_{gb}$ and $\gamma_{gb}$ are usually related to the experimental observations while $\delta_{gb}$ can be chosen as fitting parameter. For example, $\delta_{gb} = 0.48\,\mu m$ in [55] and in [91] $\delta_{gb} = 0.542\,\mu m$ using values $L = 6.4\times10^{-9}\ m^3/(J\cdot s)$ and $M_{gb} = 2.6\times10^{-15}\ m^4/(J\cdot s)$ in equation (13).

On the other hand time scale parameter $\tau_0$ can be taken as an independent scaling parameter. Examples of material properties see Appendix B.

In this case mobilities are defined as

$$\tilde{M} = \left(\frac{MB}{l^{*2}}\right)\cdot\tau_0 = \left(\frac{DV_mB}{Lk_BTl^{*2}}\right)\cdot\tau_0 = \left(\frac{3}{4}\frac{DV_m\gamma_{gb}}{\delta_{gb}k_BTl^{*2}}\right)\cdot\tau_0$$

and

$$\tilde{L} = (LB)\cdot\tau_0 = \left(\frac{M_{gb}\gamma_{gb}}{\delta^2}\right)\cdot\tau_0\,.$$

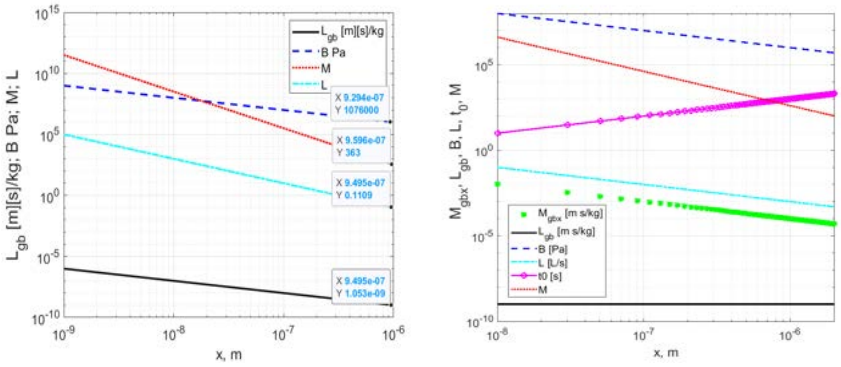


Figure 25. (left) Values of the phase-field model parameters for $\tau_0 = 100$ sec as a function of length scale $l^*$. $M$ and $L$ are dimensionless parameters diffusion and phase-field mobility respectively. (right) The same values as in the left panel but with time scale defined as $\tau_0 = 1/LB$, $D_s = 5 \times 10^{-8}$ cm$^2$/s. Time scale as a function of length scale is also added to the figure.

Dependence of the various dimensionless parameters of the assumed value of the grain boundary thickness $\delta_{gb}$ is shown in Fig. 25.

## 5.1 2D Model

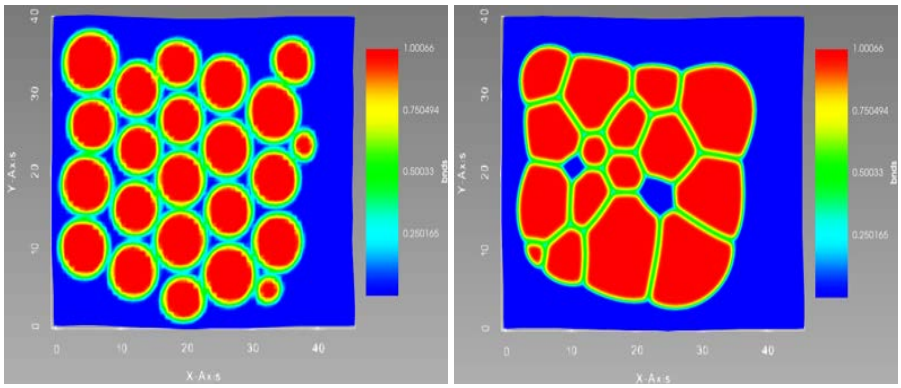


Figure 26. Results of the phase-field simulations of the microstructure evolution for 23 particles, zero gravity, and periodic boundary conditions.

To implement phase-field models of particles sintering in numerical simulations we use MOOSE (Multiphysics Object-Oriented Simulation Environment).

Significant help in developing the model was provided by Sudipta Biswas – Computational Scientist at Idaho National Laboratory. The main dimensionless parameters of the model are shown in Fig. 25, see

also Sec. B for examples of the phase field model parameters for sintering.

We developed 2D and 3D phase-field models of sintering. Results of the simulations in 2D are shown in Fig. 23 and 26 for zero gravity, periodic boundary conditions, 23 and 20 particles respectively. The difference between two figures is in the coefficient $\kappa_c$ in Cahn-Hillard equation, which is equal 0.1 in Fig. 23 and 1 in Fig. 26.

It can be seen in the figures that phase-field model reproduces the transformation from particulate to dense granular structure of the samples as shown in Fig. 20. This model also provides insight into the faults developed during such transformation as shown in Fig. 23 in comparison with the experimental results. Formation of the defects both between the particles inside the filament and between filaments can be reproduced by the model and is clearly seen in the figure. Furthermore, 3D phase-field models can be used to estimate sintering stress and time scales.

## 5.2 3D sintering model

Results of the phase-field simulation of 3D sintering of metal particles are shown in Fig. 27.

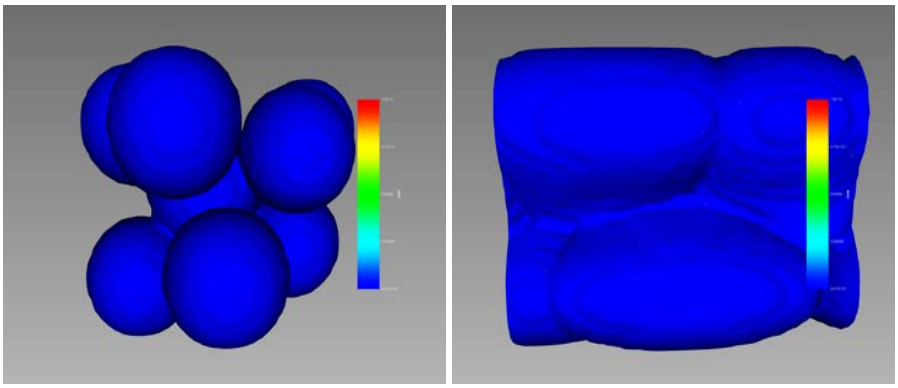

Figure 27. Results of the phase-field simulations of the microstructure evolution in 3D solid state sintering.

We note that at present the simulations are limited by a few particles and require a lot of simulation time on supercomputers. Here simulations were performed by 9 particles and mesh adaptation was excluded so that results can be considered as an order of magnitude estimations only.

Free chemical energy and the internal boundary of this system are shown in Fig. 28. This results will be used in the next section for the estimation of the sintering stress.

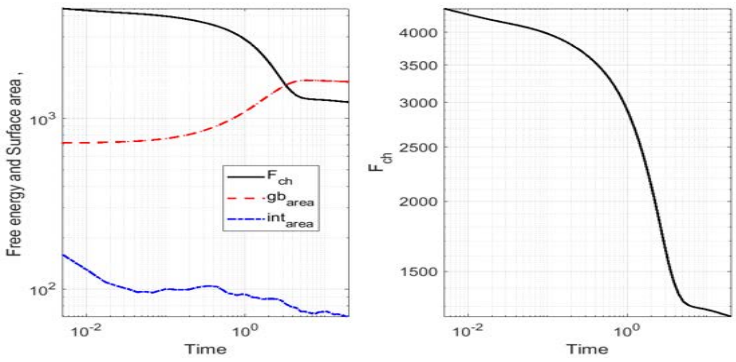


Figure 28. Results of the phase-field simulations of the microstructure evolution in 3D solid state sintering. (left) Free chemical energy, grain boundary surface area, internal boundary surface area vs time. (right) Free chemical energy as a function of time.

# 6 Estimation of the sintering stress

## 6.1 Sintering Stress: Phase Field Model

To estimate sintering stress from the results of the PFM and MD simulations we first estimate corresponding scale as $P_{scale} = R_p/G_s$ where $R_p$

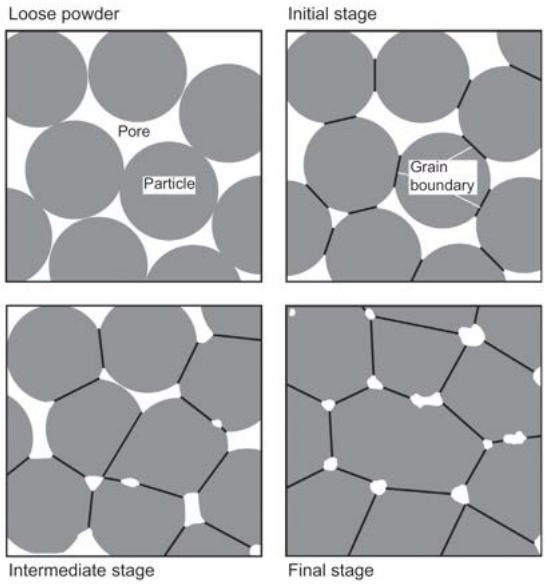


Figure 29. Graphical representation of the sintering stages, assuming the spherical particles start as a loose structure. Neck growth produces densification, round pores, and a strong body. Grain boundaries form at the particle contacts and grow as the necks merge. [37]

is the mean particles radius and $G_s$ is the surface energy, which gives

$P_{scale} \sim 10^5$ Pa.

Next estimation of the sintering stress uses the following expression [28, 67]

$$P_L = \frac{\partial F_s}{\partial v} \tag{16}$$

where $F_{s,i}$ is the surface free energy.

To apply this estimation to the discrete element model discussed in Part V we notice that initially all the metal particles are nearly intact, see Figs. 29 and 35. This allows to estimate initial surface energy as

$$F_{s,i} = \sum_{i=1}^{Np} S_{p,i} \cdot \gamma_s$$

where sum is taken over all the particles with surface areas $S_{p,i} = 4\pi R_{p,i}^2$.

To estimate the change of the volume we notice that in the intermediate state all the particles have the same volume but their shape is changed to the space filling polyhedrons. As an example we chose for e.g. truncated octahedron for which volume $V_{to}$ and surface area $S_{to}$ are known as a function of the edge length $a$

$$V_{to} = 8\sqrt{2}a^3 \qquad \text{and} \qquad S_{to} = \left(6 + 12\sqrt{3}\right)a^2.$$

We also notice that in this state all the particles are in full contact with each other and the form grain boundary surface as shown in the right panel of the Fig. 19. The final surface energy in this case can be found as half of the total area of the particles (to avid double counting of the grain boundary area) times grain boundary energy

$$F_{s,f} = \frac{1}{2}\sum_{i=1}^{Np} S_{to,i}\gamma_{gb}.$$

The corresponding change of the volume of the system of particles can be found if we recall that initial porosity in our model is around $\sim$ 60 %, which gives full initial volume $V_i = \frac{1}{0.6}\sum_{i=1}^{N_p} \frac{4}{3}\pi R_{p,i}^3$. This gives an estimate for the sintering stress according to (16) $P_L \approx (F_{s,i} - F_{s,f})/(0.4V_i) \approx 3.5 \times 10^5$ Pa.

Next, we use the results of the phase-field modeling discussed in Sec. 5.2. The sintering stress we estimate as

$$P_L \approx \frac{\Delta F_{ch}}{\Delta V_{pore}} \approx 4.3$$

using dimensionless variables.

To dimensionalize the obtained results we can use values of energy and time units shown in Fig. 25 and chose the value of the grain boundary width $\delta_{gb}$. The latter value was estimated in Sec. 2.3 as 1-2 µs. This

gives estimations for the sintering stress of the order 2-4 MPa, while the corresponding time scale of sintering can be estimated as 1.6 - 3.2 hours. We now compare these values with the values of the sintering stress obtained in experiment and in kinetic Monte Carlo simulations.

## 6.2 Sintering Stress: Experiment [28]

One of the measurement methods is loading dilatometry, in which the instantaneous shrinkage rates of a free as well as a uniaxially loaded powder compact are measured while sintering. Typically, a cylindrical sample is loaded in the axial direction and the shrinkage rates in the axial direction $\dot{e}_z$ and in radial direction $\dot{e}_r$ are measured and compared with the shrinkage rates in freely sintered samples $\dot{e}_f$. The sintering stress $P_L$ is obtained in the following manner. The axial strain rates

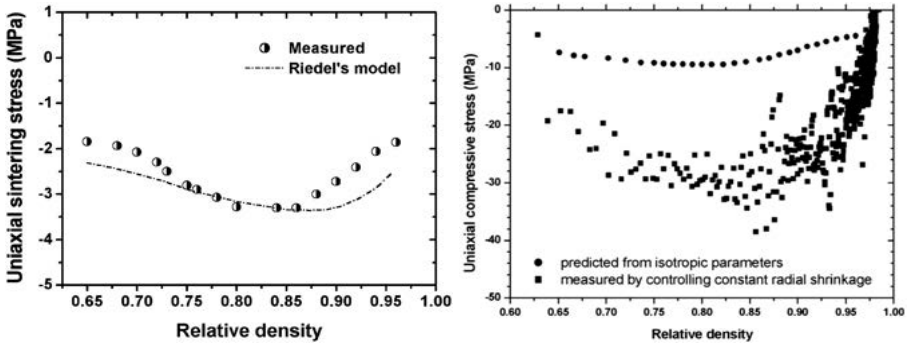


Figure 30. (left) Sintering stress as a function of density derived as the envelope from several discontinuous hot forging experiments [99]. (right) This was calculated using isotropic continuum models and measured uniaxial stress needed for radial shrinkage during sinter-forging as a function of density. [27].

$\dot{e}_z$ at several of different applied stresses are measured to calculate the uniaxial viscosity $E_p$, using the relation:

$$\dot{e}_z = \dot{e}_f + \frac{\sigma_z}{E_p}$$

where $\sigma_z$ is the applied uniaxial stress. The uniaxial viscosity $E_p$ and the free sintering rate $\dot{e}_f$ are then used to obtain the uniaxial sintering stress $\sigma_z$:

$$\sigma_s = \dot{e}_f E_p$$

The sintering stress $P_L$ is related with the uniaxial sintering stress $\sigma_s$ as:

$$P_L = \frac{\sigma_s}{1-2\nu_p}, \quad \nu_p = \frac{E_p\left(\dot{e}_f - \dot{e}_r\right)}{\sigma_z}.$$

Results of the experimental estimations of the sintering stress are shown in Fig. 30

### 6.3 Sintering stress obtained using kinetic Monte Carlo [28]

The sintering stress, $\sigma_s$, is defined as the mechanical hydrostatic stress which just balances the internal surface tension forces so that the porous solid does not shrink. It can be expressed as [28, 67], cf (16)

$$P_L = \frac{\partial F_s}{\partial v} \tag{17}$$

where $F_s = \frac{1}{V}\sum_{i=1}^{P}\sum_{j=1}^{N} J_{ij}$ is the surface free energy, $J_{ij}$ is the interaction energy at $i$-th pore site with $j$-th neighbor, and $v$ is tye specific volume.

Results of the numerical estimations of the sintering stress using kinetic Monte Carlo model are shown in Fig. 31

Data obtained in experiment (Fig. 30) and numerical simulations (Fig. 31) suggest that sintering stress can be as high 20 MPa in support of our estimations.

To conclude this section we note that phase-field model provides deep insight into the micro-structure evolution of the system during sintering and can reproduce the transformation from particulate to dense granular structure of the samples. It can also be used to estimate qualitatively the fault development during such transformation (including defects formed between and within filaments) that can be compared with the experimental observations. 3D phase-field models can be used to estimate sintering stress and time scales.

However, the simulations are limited by a few particles in 3D and phenomenological parameters of the model have to be fitted carefully for each type of the metal alloy and particles size and distribution.

At present phase-field models cannot be used for predictions of shrinkage of full-size components. However, it provides important parameters for continuous model sintering of full-size parts. These parameters include sintering stress $P_L$, its relation to the density, and non-

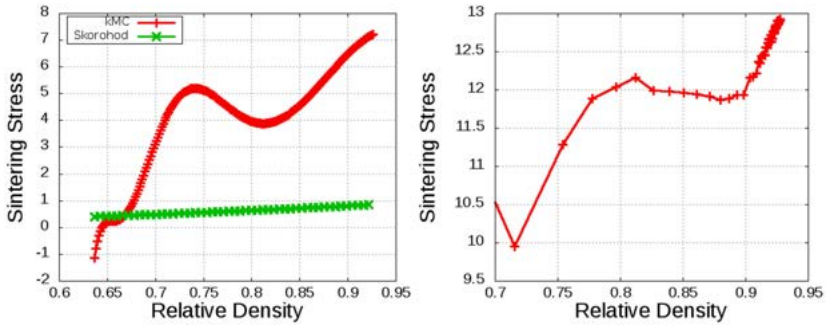


Figure 31. Results of simulations of the sintering stress for 4000 randomly packed particles obtained using energy method (left) and curvature method (right) in kinetic Monte Carlo simulations [28]. Stress units are $\gamma_s/r_0$.

uniform spatial distribution of the density due to the size of the particles and layout of the filaments.

Modeling of shrinkage for the full-size parts can be performed using continuous finite-element modeling in commercial software such as COMSOL Multiphysics® [32] as discussed in Part VI. But before we consider finite element model of the whole part we need to provide estimations of the mass distribution in the sample that accounts for the filament layout and the initial rearrangement of the particles. A convenient modeling framework that has the required unique capabilities is provided by the discrete element method discussed in the next section.

# Part V
# Discrete Particle Model [95]

## 1 Model

A microscopic model of sintering within the framework of the discrete element method (DEM) is based on a new generalized viscoelastic model of sintering proposed in [66].

The following equation for the particle interaction during sintering was obtained:

$$F_n = \frac{\pi a^4}{8 D_{eff}} v_{rn} + \pi \gamma_s \left[ 4r \left( 1 - \cos \frac{\psi}{2} \right) + a \sin \frac{\psi}{2} \right] \tag{18}$$

where $F_n$ is the normal force between two particles, $v_{rn}$ the normal relative velocity, $r$ the particle radius, $a$ the radius of the interparticle boundary, $\psi$ the dihedral angle, $\gamma_s$ the surface energy.

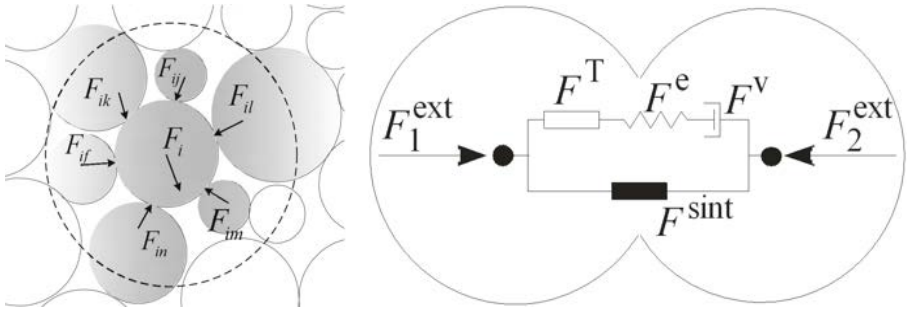


Figure 32. (left) Forces and particle arrangement in sintering process. (right) Components of the force between two particles.

It is assumed that the grain boundary diffusion is the dominant mechanism of sintering and the effective grain boundary diffusion mechanism is given by

$$D_{eff} = \frac{D_{gb} \delta \Omega}{k_B T} \tag{19}$$

where $D_{gb}$ is the grain boundary diffusion coeffcient with the width $\delta$, $\Omega$ is the atomic volume, $k_B$ is the Boltzmann constant and $T$ is the temperature.

The constitutive relations take the form [76]

$$\dot{\sigma} = \mathbf{C} : \left( \dot{\varepsilon}^e - \dot{\varepsilon}^T - \dot{\varepsilon}^v \right) + \mathbf{I} \dot{\sigma}^{sint} \tag{20}$$

where $\sigma$ is the Cauchy stress tensor, $C$ the elastic stiffness tensor, $\sigma^{sint}$ the sintering driving stress. And the strain rate $\dot{\varepsilon}$ is decomposed into the elastic, thermal and viscous parts, $\dot{\varepsilon}^e$ , $\dot{\varepsilon}^T$ and $\dot{\varepsilon}^v$ respectively:

$$\dot{\varepsilon} = \dot{\varepsilon}^e + \dot{\varepsilon}^T + \dot{\varepsilon}^v$$

where

- $\dot{\varepsilon}^T = \alpha T \mathbf{I}$;
- $\dot{\varepsilon}^v = \frac{\sigma'}{2\eta_s} + \frac{tr\sigma - 3\sigma^s}{9\eta_b}\mathbf{I}$
- $\dot{\varepsilon}^e = \frac{\beta\gamma_s\rho^2}{r}$
- $\rho = \rho_0 \exp\{-\left(\varepsilon_x + \varepsilon_y + \varepsilon_z\right)\}$

All parameters in the above equations viscosity $\eta_s$, $\eta_b$, initial relative density $\rho_0$, surface energy $\gamma_s$ etc. are related to microscopic material properties. For spherical shape of powder particles $\beta$ is equal 3, $\eta_s$ and $\eta_b$ are viscous shear and bulk moduli respectively and these factors are functions of porosity and temperature.

A preliminary conclusion of this subsection is that contact forces in the DEM formulation can be related to thermodynamics and constitutive relation of the Olevsky continuous model, see also Part VI. We used the DEM approach to model rearrangements of particles at initial stage of sintering in realistic geometries and filament layouts. A discussion of some results of simulations is presented in the next section.

# 2 Results of numerical simulations of DEM

## 2.1 Forces.

The discrete element model of particle sintering was developed in KRATOS Multiphysics [33,34]. The contact forces [75] between two particles was modeled using Hertz model with JKR cohesion [96]

$$F^{cont} = F^{elast} + F^{visc} \tag{21}$$

as a sum of elastic and viscous components.

- Elastic part assumes linear force–displacement relationship

$$F^{\text{elas}} = k\ \mathrm{u}_r$$

where $u_r$ is the particles penetration, $k$ is the contact stiffness.

- The viscous component is assumed to be a linear function of the normal relative velocity $v_{\text{rn}}$

$$F^{\text{visc}} = c\ \mathrm{v}_{\text{rn}}$$

viscosity coefficient $c$ can be taken as a fraction $\xi$ of the critical damping $C_{\text{cr}}$ for the considered system

$$c = \ C_{\text{cr}} = \xi\ \sqrt{\frac{k m_i m_j}{m_i + m_j}}$$

where $m_i$ and $m_j$ are masses of two particles and $k$ is an effective spring stiffness.

The particle interaction force, $F$, during sintering is given by the equation (18) derived considering mass transport and stresses at the grain boundary between two sintered particles. The effective diffusion coefficient is given by eq. (19).

## 2.2 Model geometry.

First, NIST test artifact (see Fig. 6) for sintering analysis was sliced using Repetier-HOST v.2.1.6 slicer, see top-left figure in Fig. 33. Next, a small subsystem, cylinder shown in the top-right Fig. 33, was selected for further analysis. Finally, sub-models of the cylinder with different filament layouts were constructed.

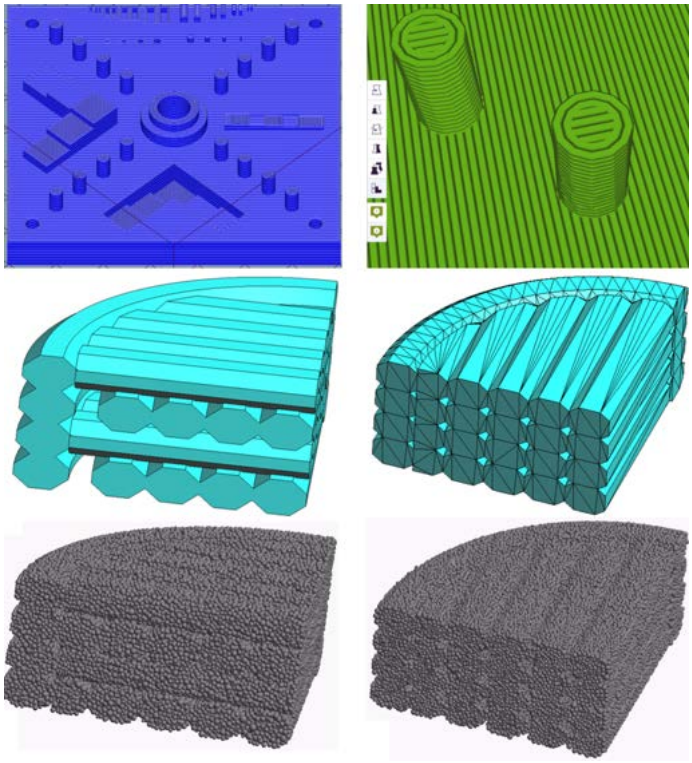

Figure 33. (top line) Result of slicing NIST artifact for additive manufacturing. (middle line) Mesh of a submodel of the NIST artifact using GID. (bottom line) Discrete element model of the filaments in KRATOS DEM.

The sub-models were build in SALOME v9.3 [78] for two different filament layouts: (i) cross layered layers and (ii) all layers are laid in the same direction. The STL files of sub-models were imported into KRATOS Multiphysics. Simulations were conducted using DEM application.

## 2.3 Effect of layout.

The material parameters chosen for the simulations are shown in the Table 3.

Table 3. Parameters of some packing models

| | |
|---|---|
| Density $\rho$ | $4500 kg/m^3$ |
| Poisson ratio | 0.3 |
| Coefficient of restitution | 0.2 |
| Constitutive law | Hertz with JKR cohesion |
| Yaung modulus, $E$ | $5{\times}10^6$ $Pa$ |
| Cohesion $E_c$ | 1500 $Pa$ |
| Gravity acceleration | 9.8 m/sec$^2$ |

**Cross-layers.** Preliminary results of initial sintering for the crossed direction of the filaments in each layer are shown in Fig. 34 In this case

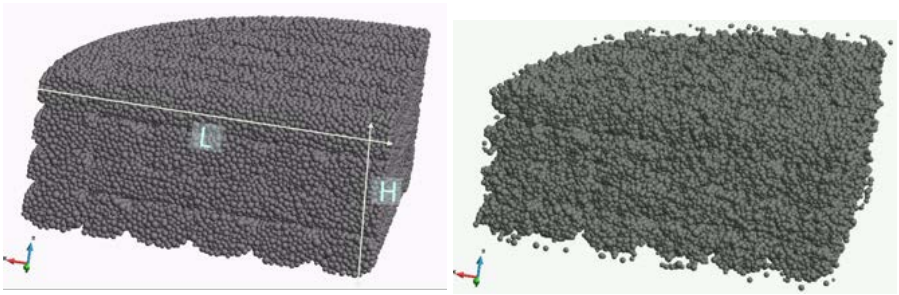


Figure 34. Results of sintering for crossed orientation of the filaments in each layer: (left) initial and (right) final states.

the following parameters were used $E = 1.5 \times 10^6$ Pa, $E_c = 1500$ Pa, and other parameters as in the Table 3. Resulting shrinkage is: $L_{x,f}/L_{x,0} = 0.956$ and $L_{z,f}/L_{z,0} = 0.955$. The total number of spherical articles in these simulations is $\sim$ 150,000.

**Unidirectional layout.** Similar preliminary simulations were performed for the same set of parameters but for the unidirectional filament layout shown in the Fig. 33 bottom right. Resulting shrinkage is: $L_{x,f}/L_{x,0} = 0.931$ and $L_{z,f}/L_{z,0} = 0.814$.

The preliminary results indicate that there is some dependence of the shrinkage on the filament layout. To verify predictions of preliminary calculations we performed a more detailed analysis of shrinkage as a function of model parameters. The results of this studies are summarized in Tables 4-6.

It can be seen from the Tables that results strongly depend on the model parameters. In this case two key parameters are Young's modu-

lus and cohesion energy. However, a few trends can be reveal from this examples. In most cases initial shrinkage is smaller in vertical and horizontal directions for cross-layout as compared to unidirectional layout. For one set of parameters (see Table 5) this trend is much more pronounced for increased initial porosity. In one case we could detect larger shrinkage in vertical as compared to the horizontal direction for reduced cohesion energy.

However, overall anisotropy is weak in the absence of gravity and gravity is the key reason for nonlinear shrinkage as we will discuss next.

Table 4. Comparison of shrinkage for cross- and unidi-rectional layout of filaments with $E = 5 \times 10^6$ Pa and $E_c = 500$ Pa

| NIST_item7_v4_test_default | | | | NIST_item7_v5_5_test2 | | | |
|---|---|---|---|---|---|---|---|
| E = 5e6 Pa; Ec = 500 Pa; default; uni | | | | E = 5e6 Pa; Ec = 1500 Pa; default; cross | | | |
| LY0 | 15.14 | LZ0 | 9.86 | LY0 | 16.14 | LZ0 | 9.58 |
| LYF | 13.96 | LZF | 8.93 | LYF | 14.95 | LZF | 8.97 |
| LYF/LY0 | 0.92 | LZF/LZ0 | 0.905 | LYF/LY0 | 0.926 | LZF/LZ0 | 0.935 |
| LX0 | 15.22 | LX0 | 21.42 | LX0 | 16.12 | LX0 | 20.75 |
| LXF | 14.14 | LXF | 19.89 | LXF | 15.1 | LXF | 19.16 |
| LXF/LX0 | 0.93 | LXF/LX0 | 0.93 | LXF/LX0 | 0.936 | LXF/LX0 | 0.923 |

Table 5. Comparison of shrinkage for cross- (right) and uni-directional (left) layout of filaments with $E = 5 \times 10^6$ Pa and $E_c = 1500$ Pa

| NIST_item7_v4_t5-porosity_04 | | | | NIST_item7_v5_5_t3_porosity_04 | | | |
|---|---|---|---|---|---|---|---|
| E = 5e6 Pa; Ec = 1500 Pa; Por 0.4; uni | | | | E = 5e6 Pa; Ec = 1500 Pa; Por 0.4; cross | | | |
| LY0 | 15.49 | LZ0 | 12.66 | LY0 | 15.01 | LZ0 | 7.73 |
| LYF | 13.87 | LZF | 11.07 | LYF | 14.24 | LZF | 7.23 |
| LYF/LY0 | 0.895 | LZF/LZ0 | **0.874** | LYF/LY0 | 0.949 | LZF/LZ0 | **0.935** |
| LX0 | 15.63 | LX0 | 27.49 | LX0 | 15.14 | LX0 | 16.72 |
| LXF | 14.02 | LXF | 23.96 | LXF | 14.02 | LXF | 15.73 |
| LXF/LX0 | 0.896 | LXF/LX0 | **0.872** | LXF/LX0 | 0.926 | LXF/LX0 | **0.94** |

## 2.4 Effect of gravity.

The gravity effect is illustrated in Fig. 35. The filament dimensions in this sample are $0.5 \times 2.0 \times 0.3$ mm. The volumes of the filament and the spheres are $V_f = 0.3$ mm$^3$ and $V_s = 0.136$ mm$^3$ respectively and initial porosity $\sim 56$ %. The shrinkage in $z$-direction is ~22% while the sample practically does not shrink in horizontal plane. The final porosity is ~42%, which approximately corresponds to our estimation of the particle density in the filament, see Sec. 2.1.

Table 6. E = 1e6 Pa; Ec = 500 Pa;  = 0.3; restitution = 0.2; t = 5 s; Porosity default; layout  uni (left) and cross (right)

| NIST_item7_v4_t4_default | | | | NIST_item7_v5_5_default | | | |
|---|---|---|---|---|---|---|---|
| E = 1e6 Pa; Ec = 500 Pa; default; uni | | | | E = 1e6 Pa; Ec = 500 Pa; default; cross | | | |
| LY0 | 17.3 | LZ0 | 12.34 | LY0 | 15.9 | LZ0 | 10.9 |
| LYF | 15.29 | LZF | 9.31 | LYF | 13.96 | LZF | 9.01 |
| LYF/LY0 | 0.884 | LZF/LZ0 | **0.754** | LYF/LY0 | 0.878 | LZF/LZ0 | **0.826** |
| LX0 | 17.36 | LX0 | 26.42 | LX0 | 15.95 | LX0 | 23.53 |
| LXF | 15.51 | LXF | 23.34 | LXF | 13.95 | LXF | 20.54 |
| LXF/LX0 | 0.893 | LXF/LX0 | **0.883** | LXF/LX0 | 0.875 | LXF/LX0 | **0.879** |

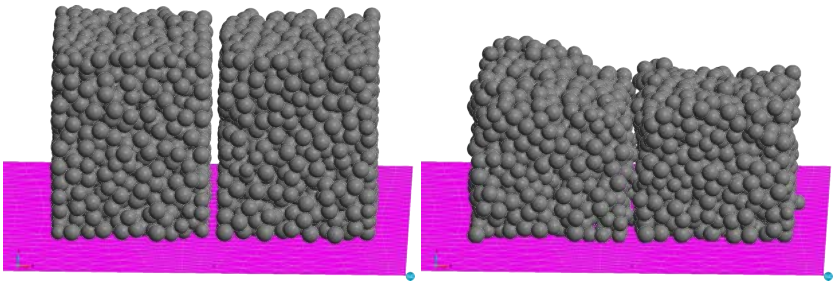

Figure 35. Effect of gravity on the initial shrinkage obtained in DEM model. (left) initial state; (right) final state after 10 sec of simulation time.

It can be clearly seen from the figure that the initial shrinkage is strongly nonlinear and the filament shrinks predominantly in $z$-direction. The observed shrinkage in $z$-direction is even larger than expected because initial density is lower than the one in filaments. We also notice that the initial gap between the two filaments ~0.02 mm remains practically intact in the end of the simulations.

Therefore, we see that simulations of the shrinkage using DEM modeling confirm our preliminary estimations of the dependence of shrinkage on the filament orientation (layout) and gravity. However, we note that Discrete Element Method at present has severe limitation in both accuracy and range of applications. In most of the DEM available software the shape of the particles does not change. Thus we have mainly used DEM approach to estimate initial rearrangement of the particles, gravity induced nonlinear shrinkage and spatial distribution of mass in the samples that are used in finite element modeling of the whole part as input parameters. We have also used DEM for estimations of the sintering stress as discussed in Sec. 6.1.

# Part VI
# Macroscopic modeling of sintering

## 1 Introduction of the sintering process for the representative materials: Ti6Al-4V and Al 7075

In this part we discuss the results of simulation sintering processes using continuum finite element modeling in COMSOL [32]. From the physics point of view we tried to keep model parameters close to those observed in experiments of sintering Ti-6Al-4V alloy made by Techshot team [1, 2]. In addition, we analyzed Al 7075 material, which was not part of the Techshot experiments. Powders of these metals can be combined with some polymer mixtures to form feedstock for fused deposition modeling in polymers. In fact, the softening temperature of compatible binder materials are substantially lower than the melting temperature of the metal powder enabling filament printing through an extrusion method [1, 2].

Once printed the waxes and polymers are removed from the printed part in a process known as debinding. The binder is removed by heating the sample in 50 Torr vacuum. Depending on the binder and metal material, it might be difficult to remove the binder material without partially melting some metal particles, especially for aluminum material. There is an overlap between the debinding and melting/sintering temperature of Aluminum. Due to this narrow temperature gap it is possible to have the debinding and sintering processes occurring simultaneously [2]. If this situation occurs, the residues from the binder will become trapped as impurities in the sintered aluminum structure. This means we should take into account polymer expelling during sintering and this physics might play a substantial role in shrinkage process.

In our simulations we are using typical structural parameters for the modeled material (similar to Ti-6Al-4V and Al 7075) considering that the green part was produced by printing filaments. Two different powders were considered both coarse and fine [1–3]. Based on the polymer decomposition behavior, the thermal debinding profile was generated for 59 vol % Ti-6Al-4V or Al 7075 feedstock. The selected heating rate was 1-2 °C/min with 3 holds at 240 °C, 325 °C and 440 °C with a holding time of 3 hours at each degradation stage. As a result, the binders were completely removed thermally at three stages at a heating rate of 1-2 °C/min in low pressure to produce the brown part. Later on, the brown part went through the sintering process, for example, for Ti-6Al-4V at 1300-1400 °C for 3 hours of holding time at a heating and after that cooling rate of 1-2 °C/min in a low pressure environment.

Here we will consider that wax-based binder was able to thermal debind green part without shrinkage and collapse of structure. The

shrinkage of the sintered part was considered at the sintering stage.

A large fraction, say about 40%, of the parts volume after debinding is the empty space, and it is referred to as a brown part. That is why the brown part is very fragile. Some residual binder mixes keep a component of the binder - a backbone binder in place until sintering starts to keep the print part from disintegrating in the brown stage. This stage accomplished by growth and strong adhesion among the adjacent particles, causing the retraction of the product whose dimensions usually reduce between 10 and 15%. The matter is that a small amount of residual backbone binder still exists keeping the sintering particle altogether. The part is then sintered while each powder particle will connect with its neighbors. Sintering usually takes place in a vacuum or in an inert gas [4].

As thermal debinding proceeds to the end (440 °C) only a small residual amount of backbone binder is left. This backbone binder is mostly located at inter-particle necks. The capillary force tends to rearrange particles and thereby to induce internal stress. In this case two possible mechanisms of sintering could be considered. The first one is due to sintering stress caused by capillary force and the second one is shrinking the solid continuum due to shrinking the solid continuum due to residual debinder expelling from the volume. The first mechanism is due to viscoelasticity and creep behaviour and second one is caused by swelling (shrinkage) of the solid continuum by change of the concentration of residual debinding. All these mechanisms are phenomenological one and can show qualitative results of the sintering.

## 2 Equations for modeling metal-fused filament fabrication (mFFF) process

A rheological theory of sintering was developed by Skorohod [5], and published in the book Rheological Basis of the Theory of Sintering in 1972. In this book, the theory of sintering of powder materials is sequentially formulated. The theory is based upon the phenomenological concept of the generalized-viscous flow of porous bodies. These results were further extended by Olevsky [6, 7] derivation (based upon the stochastic approach) of the relationships for the dependencies of rheological parameters (such as bulk, shear viscosities and effective sintering stress) of porosity and the solution of the problem of the deformation of a viscous porous body under sintering simultaneous to a uniaxial loading. The book also contains an analysis of the main molecular mechanisms of the viscous flow of real amorphous and crystalline bodies, the kinetics of inter-particle contact growth and models of non-isothermal sintering and sintering accompanied by heterodiffusion.

Since the printing process was simulated by Techshot using Digimat-AM to figure out residual stresses of the green part [1] we will not

consider this here. The matter is that residual stresses, thermal history, deformation and wrapage changes the structural parameters when you cool the structure down. During the debinding, formation of the brown part and sintering these thermo-mechanical 3D printing residual stresses most probably play a minute role. That is why we consider here two stages which might lead to shrinkage: debinding of the backbone polymer at the temperature close to sintering and sintering itself caused by capillary forces. In addition, we will try to model some properties of the sample obtained by metal fused filament fabrication (mf3).

Dimensional change during "mf3" process, shrinkage or swelling, could be predicted based on the continuum mechanics where the printed body part is composed by metal skeleton and binder embedded in this mechanical continuum. During debinding the binder is burned out and removed from the furnace chamber, while the pores are filled by air or inert gas. The corresponding solid system transformation is modeled by solving systems of coupled continues equations for solid state media, diffusion, and heat transfer. In addition, binder diffusion activated by temperature should be taken into account. Moreover we should imply how the medium changes in structure during debinding. Close to sintering temperature we do not have a binder embedded in the medium and we consider that the certain value of the air volume is in the structure.

The corresponding dimensional changes are the result of changes in the viscosity and sintering stress, which leads to collapse of the pores. Since we do not have experimental parameters for all these processes we cannot predict the shrinkage of swelling well. Instead, these processes are described by phenomenological parameters introduced on the basis of underlining physics.

To model the starting process we use continuum mechanics medium, which consist of Ti-6Al-4V or Al 7075 metal powder binded by polymer subsystem. Our goal is to determine shrinkage after two stages debinding and sintering. This means that in the final stage of the sintering process the voids containing trapped air and/or residual binder (backbone binder) in the brown part are eliminated. It follows from the experiment [1, 2] the dimensional changes between green part and brown part are not so substantial and the main shrinkage happens during sintering of the metal part. This implies that the densification of the metal powder particles are performed by elimination of pores left by the removed binders. The final sintering structure still contains pores as defects and modeling and/or machine learning approaches should be used to predict dimensions of the sintered part. Let us consider two of these approaches in more details.

## 2.1 The two laws of material behavior. Olevsky model simulation

The elastic mechanical component can be represented by an elastic spring and the viscous component by a dashpot (a pot that contains a viscous liquid that can flow under the action of a piston)

$$\sigma = E\varepsilon \text{ and } \sigma = \eta\dot{\varepsilon},$$

where $\sigma$ is stress, $\varepsilon$ is strain, $E$ is a Young modulus and $\eta$ is a viscosity. The first relation is elastic and the second one is viscoelastic. In turn, there are two different viscoelastic models. The Maxwell model consists of a spring term and and a dashpot term placed in series. As a result, strain rate is the sum of the contributions from both components

$$\dot{\varepsilon} = \dot{\sigma}/E + \sigma/\eta, \tag{22}$$

where first part is elastic law and second term is a creep.

The Voigt - Kelvin model consists of a spring and a dashpot in parallel. For this model, the strains on the elastic and dashpot components are always the same and the overall stress is the sum of the stresses on the spring and dashpot.

$$\sigma = E\varepsilon + \eta\dot{\varepsilon}. \tag{23}$$

The constitutive equations(22),(23) lead to different sintering models. The Voigt - Kelvin model is generalized for Olevsky model while Eq. (22) leads to Riedel's model [11]).

In fact, for the phenomenological sintering model, the strain rate consist of the equivalent elastic strain rate $\dot{\varepsilon}_e$, thermal strain rate $\dot{\varepsilon}_T$, and creep strain rate $\dot{\varepsilon}_{cr}$,

The last term is responsible for sintering and can be presented as a ratio between the deviatoric stress $\sigma'$ and shear viscosity modulus $\eta_s$ , and the ratio between the equivalent volumetric stress and bulk viscosity modulus $\eta_b$

$$\dot{\varepsilon}_{cr} = \frac{\sigma'}{2\eta_s} + \frac{tr(\sigma) - 3\sigma_s}{9\eta} I, \tag{24}$$

where $\sigma_s$ is the sintering stress (sintering driving force), tr($\sigma$) is the trace of the stress tensor, $I$ an identity matrix.

The constitutive model usually used for sintering was developed by Olevsky [7] is given by equation

$$\sigma_{ij} = 2\eta(\varphi\dot{\varepsilon}'_{ij} + \psi\dot{\varepsilon}_{ij}) + P\delta_{ij}, \tag{25}$$

where $\eta$ is the apparent viscosity of the porous body skeleton, $P$ is the effective Laplace pressure (sintering stress, $\delta_{ij} = 1, \quad \text{if} \quad j = i, 0, \quad \text{if} \quad j \neq i$ ), $\varphi$ and $\psi$ are the coefficients of the effective shear and bulk moduli, respectively

$$\varphi = (1-\theta)^2, \text{ and } \psi = (1-\theta)^3/\theta. \tag{26}$$

Here porosity $\theta$ is defined as the ratio of the volume of pores $V_{pores}$, to the total volume $V_{total}$:

$$\theta = V_{pores}/V_{total}. \tag{27}$$

The effective Laplace pressure can be considered as

$$P = \frac{3\gamma}{r_0}(1-\theta)^2, \tag{28}$$

where $r_0$ is the mean radius of powder particles, and $\gamma$ is the surface tension energy (surface of pores). For our sintering approach we can assume that external stress is equal to zero and from (25) get

$$P = 2\eta\psi\dot{\varepsilon}_v = \frac{3\gamma}{r_0}(1-\theta)^2, \tag{29}$$

where $\dot{\varepsilon}_v$ is a free volume shrinkage.

Using continuity equation for mass conservation

$$\dot{\theta} = (1-\theta)\dot{\varepsilon}_v = \frac{\sigma_s}{2\eta\psi}(1-\theta)^3 \tag{30}$$

from equations (26) and (29) we can obtain

$$\dot{\theta} = -\frac{3\gamma}{\eta_0 r_0}\theta = -\frac{\sigma_s}{\eta_0}\theta.$$

If the coefficients in front of $\theta$ on the right hand side do not depend on $t$ we can write the analytical solution of sintering

$$\theta = \theta_0 \exp\left(-\frac{\sigma_s}{\eta_0}t\right),$$

where $\theta_0$ is initial porosity. This equation shows that at infinite time we will have no porosity

As a result, specific time of sintering for continuum models is

$$\tau_{\text{sin}} = \eta_0/\sigma_s$$

This means that the higher is the sintering stress the shorter is the time off sintering. For the characteristic value $\sigma_s \sim 10^6 Pa$ and typical value of $\eta \sim 10^{12} Pa \cdot s$ we get the $\tau_{\text{sin}}$ is about $10^6 s$, which is not the case for the for mf3 sintering. In our case sintering is taking place for three hours and this means that sintering time is $10^4 s$. In order to have phenomenological Olevsky's theory working in our case we have to assume that viscosity is about $10^{10}$ - $10^{11} Pa \cdot s$.

The commercial software COMSOL® [32] has been used in the simulation of the sintering process. In addition to solid state structural module, the Domain ODEs and DAEs mathematics has been used for

porosity modeling. The viscoelastic properties have been taken into account by using Kelvin-Voit approach.

Some simulation experiments were done to check the limiting cases. First, we considered the case with no gravity and no sintering stress. The results are presented in Fig. 36 (a). In this case the initial porosity distribution which was taken 0.3 does not change. It should be noted that displacement and stress in this case look similar to Fig. 36 (a) and are not shown here, since no external or internal stresses are applied. In the second numerical experiment external force (gravity) was applied. As a result simulations demonstrate small perturbation in porosity, displacement and stress that can be seen in Fig. 36 (b), (c), (d). These distributions depend on the value of the viscosity in viscoelastic case. The lower is the viscosity the larger are these values.

Next, simulation is done for significant sintering stress (Fig. 37). If the initial porosity was 0.3 the final one is 0.09. The left plot (a) is done for the no gravity case. We can see that distribution of the porosity is very homogeneous with terminal porosity about 0.1. The plot (b) is the same simulation with the gravity. Final porosity is about the same. In Fig. 37 (c) we see the vertical displacement distribution which shows vertical structure shrinkage about 5%. The characteristic stress distribution (von-Mises invariant) displays practically no stress in the structure.

The result for directional and total displacement are presented in Fig. 38 for the lower viscosity and sintering stress. One can see the sintering sample shrinks and the value of the shrinkage is about 13% in vertical and lateral directions. The von Mises residual stress generated is presented in Fig. 38 and is sufficiently small.

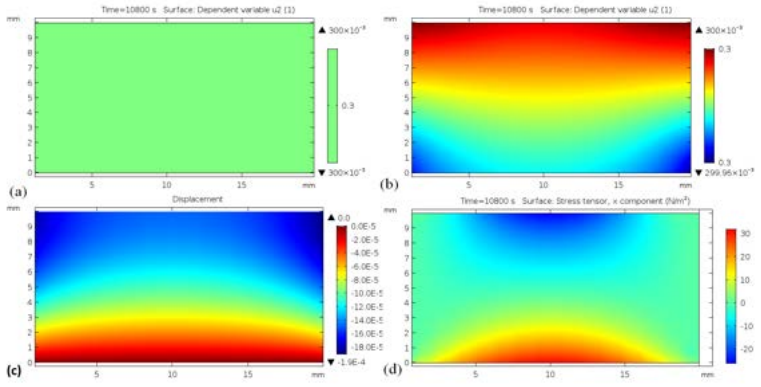


Figure 36. Simulation results for sintering at zeros sintering stress: No gravity case – (a), porosity distribution with gravity (leads to minute change in porosity) – (b), Total displacement (shrinkage uder gravity) – (c) and small residual stress – (d). Simulation performed at viscosity $\eta = 10^{10} Pa \cdot s$ for 3h of sintering time.

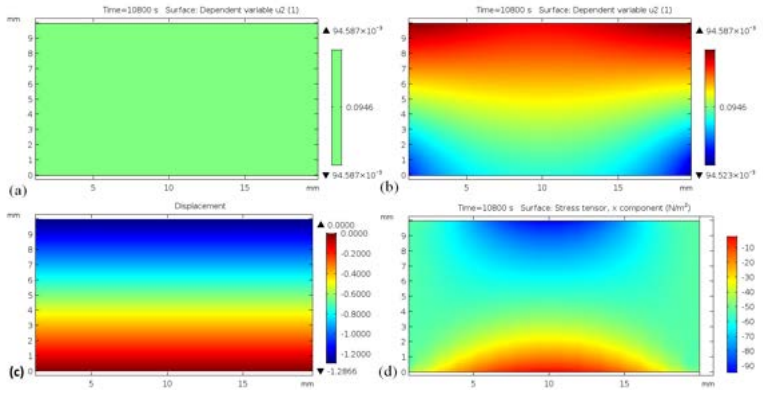

Figure 37. Porosity distribution at the end of 3h sintering time (Top left plot belongs to No gravity case – (a) and right hand side case corresponds to gravity – (b), vertical displacement distribution – (c) and x-stress componenet – (d) at $\eta = 10^{11} Pa \cdot s$, $\sigma_s = 1MPa$ ).

In Fig. 39 we see how porosity depends on the sintering stress parameter. The larger is sintering stress the smaller is the porosity value at the end of the sintering time. This dependance is a function of the viscosity value.

The simulation results for a fixed bottom constraint is presented in Fig. 40. One can see that porosity goes down except for spot point areas near the fixed corner of the structure. This characteristic feature of the high porosity is caused by nonuniform stress distribution which is sufficiently high in this area. The shrinkage of the structure could be understand from Fig. 40 (b), (c), which is about 10%. The stress distribution is presented in Fig. 40 (d), (e), and (f). One can see that

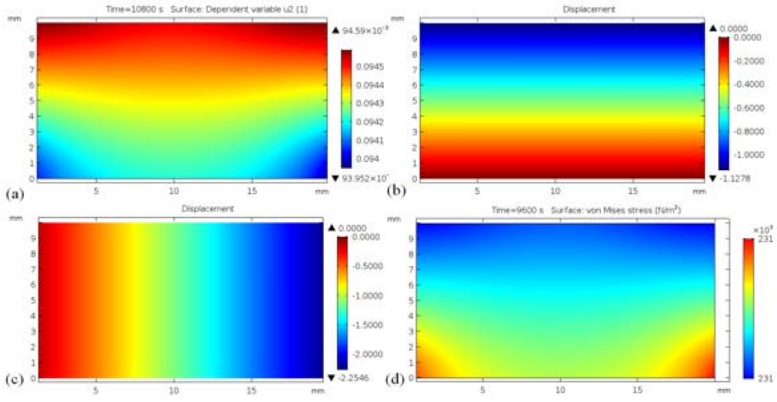

Figure 38. Illustration for shrinkage process: porosity distribution – (a) vertical displacement – (b) and transverse one –(c) and von Mises stress – (d), $\eta = 10^{10} Pa \cdot s$, $\sigma_s = 0.5MPa$

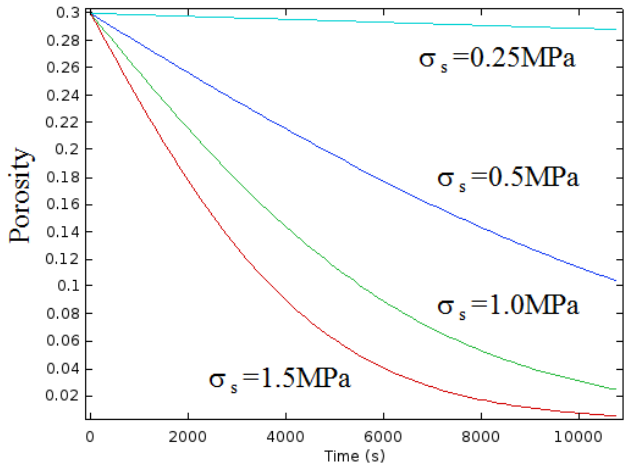


Figure 39. Dependance of the porosity on time at different values of the sintering stress. Initial porosity value is 0.3, $\eta = 10^{11} Pa \cdot s$

inhomogeneous stress in $y$-direction $S_y$ is sufficiently high at the corner, which might lead to the trap of the porosity $\theta$. The matter is that fixing boundary condition leads to the increase of stress at least for a three order in magnitude (Fig. 40 (d), (e), and (f)).

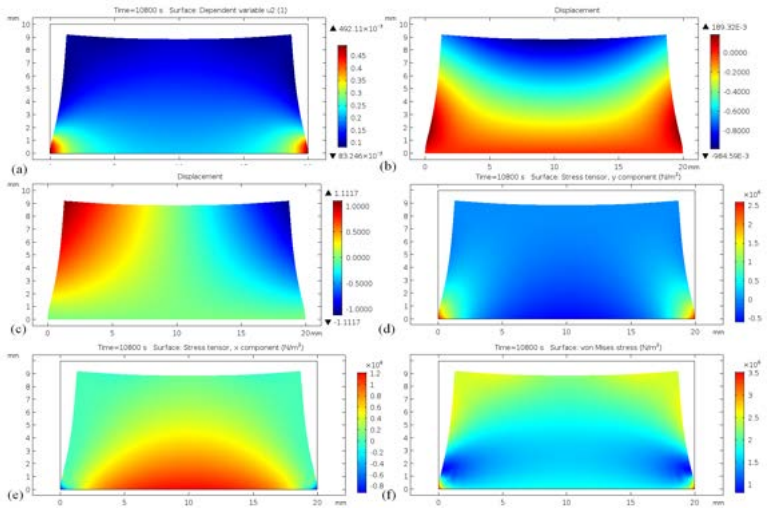

Figure 40. Porosity distribution at the end of sintering time – (a), vertical displacement – (b), horizontal displacement – (c), stress distribution $S_{yy}$ – (d), $S_{xx}$ – (e) and VonMises – (f). Initial porosity value is 0.3, $\eta = 1 \times 10^{11} Pa \cdot s$, $\sigma_s = 1$ MPa.

The next simulation results are done for axi-symmetric cylindrical structure Fig. 41 –42 with diameter 6 mm and hight of 20 mm. The results show that the higher is sintering stress the smaller is the porosity

value at the end of sintering time.

The averaged porosity distribution as function of sintering time for the axi-symmetric cylindrical structure presented in Fig. 41–42 is displayed on Figure 43. This plot is very similar to Figure 39 but in this case boundary conditions are fixed and we have inhomogeneous porosity distribution in contrast to Figure 39 where porosity is quasi homogeneous.

## 2.2 Equations for constitutive model for backbone polymer debinding. Shrinkage by binder expelling

The governing equations for an isotropic, homogeneous elastic solid medium with generalized thermo-diffusion are given in [8, 9].

$$\mu u_{i,ij} + (\lambda + \mu) u_{j,ij} + \beta_1 T_{,i} - \beta_2 C_{,i} = \rho \frac{\partial^2 u_i}{\partial t^2}, \quad i, j = 1, 2, 3 \tag{31}$$

where $u_i$ are the components of the displacement vector, $T$ is the absolute temperature, $C$ is the concentration of the diffusive material in the elastic body, $\lambda$ and $\mu$ are Lame's constants, $\rho$ is the density $\beta_1$ and $\beta_2$ are material constants given by

$$\beta_1 = (3\lambda + 2\mu)\alpha_t, \quad \beta_2 = (3\lambda + 2\mu)\alpha_c \tag{32}$$

where $\alpha_t$ and $\alpha_c$ are, respectively, the coefficients of linear thermal expansion and linear diffusion expansion

The constitutive equations for stress component $\sigma_{ij}$ have the forms

$$\sigma_{ij} = 2\mu\epsilon_{ij} + [\lambda\epsilon_{kk} - \beta_1(T - T_0) - \beta_2(C - C_0)]\delta_{ij}, \quad i, j, k = 1, 2, 3 \tag{33}$$

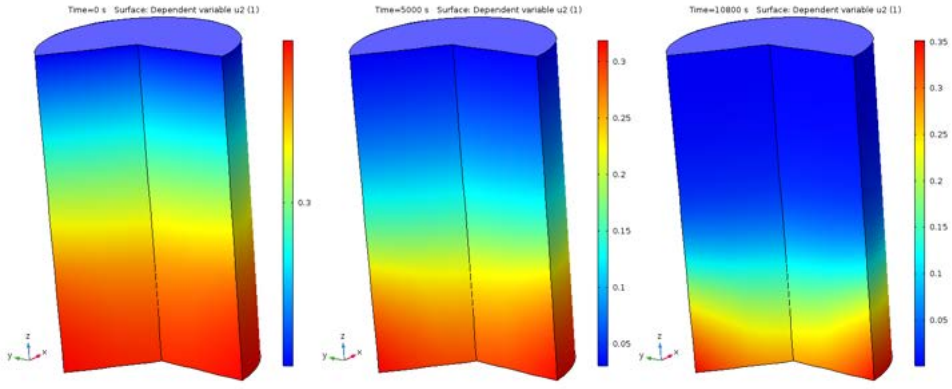


Figure 41. Time history concentration of the porosity (variable $\theta$) during sintering (left is at the $t = 0$, middle one $t = 5000$ s and right one is $t = 10^4$ s

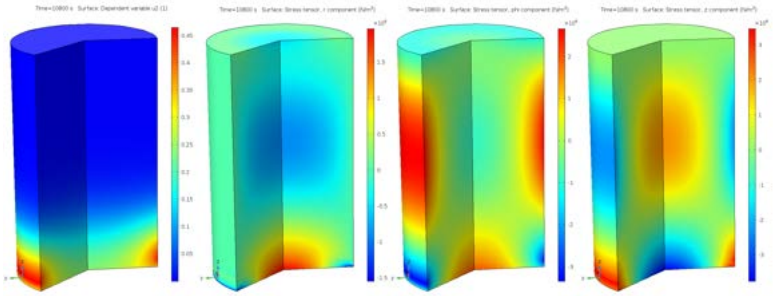

Figure 42. The porosity distribution (variable $\theta$) during sintering – left plot and radial, hoop and axial stress distributions, correspondingly $\eta = 5 \times 10^{11}\ Pa \cdot s$, $\sigma_s = 0.1$ MPa

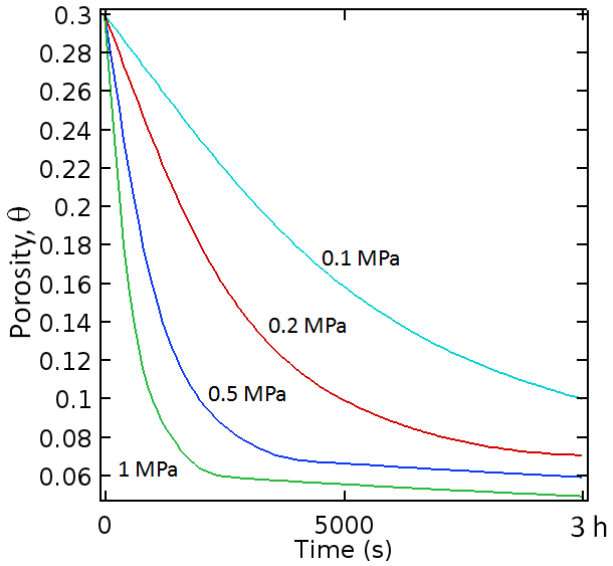


Figure 43. Average porosity distribution on time at different values of the sintering stress. Initial porosity value is 0.3, $\eta = 1 \times 10^{11} Pa \cdot s$

here $T_0$ and $C_0$ are reference temperature and concentration, and $\epsilon_{ij}$ are the stain components which are given by:

$$\epsilon_{ij} = \frac{1}{2}(u_{i,j} + u_{j,i}), \quad i, j = 1, 2, 3$$

The polymer binder can be considered as a "moisture" transport in the green part (in our case brown and silver parts) and is governed by the diffusion equation:

$$\frac{\partial C}{\partial t} = D\Delta C \tag{34}$$

which will be considered not depended on the strain and temperature

while diffusion coefficient $D$ could be presented in activation form

$$D = D_0 \exp(-U/kT)$$

where $U$ is activation energy , $k$ is the Boltsman constant. The temperature distribution is described by standard thermal equation

$$\frac{\partial T}{\partial t} = \kappa \Delta T \tag{35}$$

Here $\kappa$ is the heat conductivity coefficient. The boundary conditions on the exterior faces of the of the green part should be a flux of polymer concentration for Eq. (34) and fixed temperature determined by the heating law (Fig.**??** ) Eq. (35). In fact, slow change in temperature leads to quasi-static temperature change and we can omit solution of the equation (35) by considering that sintering part at each time moment has a temperature as presented by (Fig.**??**). This temperature activates the diffusion of the binder at different stages and makes it possible to predict shrinkage.

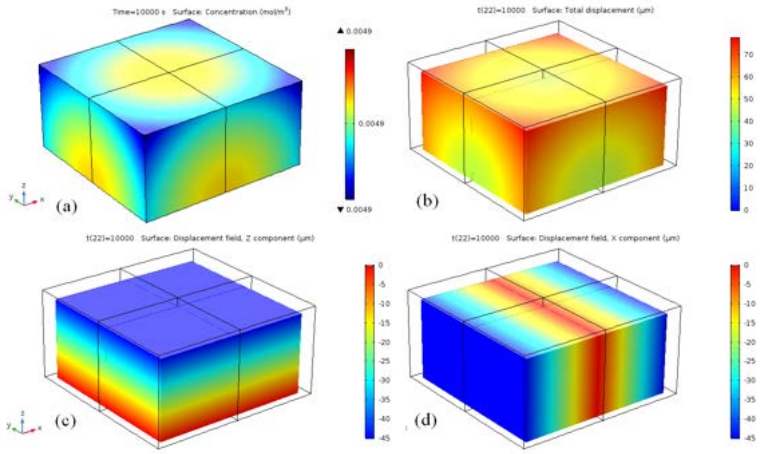


Figure 44. Concentration of the backbone debinder after sintering – (a), Total displacement – (b), direction z displacement – (c) and x one – (d). The parameters are $\beta = 10^{-3} m^3/kg$, intial concentration $10^3 mol/m^3$, diffusion coefficient $D = 4 \cdot 10^{-6} m^2/s$, brown part density was taken as $3000 kg/m^3$, Young modulus 10 GPa, Poisson ratio 0.4

During heating and expelling the residual backbone polymers from the brown part sample, the stress of the sample might change and this physics can be taken into account by the strain concentration relation

$$\varepsilon = \beta M (C - C_0) \tag{36}$$

where $\beta$ is the coefficient of hygroscopic shrinkage (swelling), $C$ is the backbone polymer concentration, and $C_0$ is the strain-free reference

concentration, M is the molar mass of the residual backbone polymer degraded products.

We consider that wax-polymer binder was able to retain the structure of the green part during thermal debinding with shrinkage as well as without any shrinkage. In the last case the brown compact stage is assumed to have the same shape as green part during sintering at 1400 °C for 3 hour. This makes it possible to consider sintering process separately and calculate shrinkage of the sintered part based on continues theory. Therefore, green parts are oversized to compensate for the sintering shrinkage. The fine particle size used in mf3 process results in high sintered density ranging from 95% to 99.5% of the theoretical density.

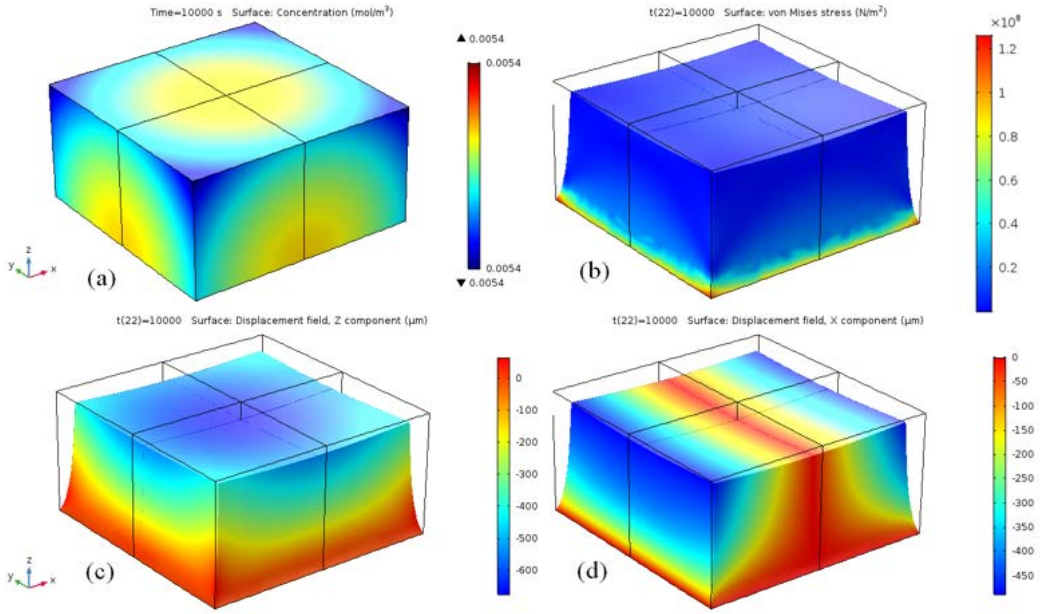


Figure 45. Concentration of the backbone debinder in the sintering part at fixed boundary conditions – (a), Von-Mises residual stress – (b), directional displacement in vertical direction (z) and in x axis (c) and (d), correspondingly. The $\beta = 10^{-3} m^3/kg$, intial concentration $10^3 mol/m^3$, diffusion coefficient $D = 4 \cdot 10^{-6} m^2/s$ , Young modulus is 10 GPa, Poisson ratio 0.4.

In the sintering step, the particles bond together, leading to densification of the small remaining brown part. During this stage the molded part undergoes volumetric shrinkages ranging from about 12% to 18% in experiment [1].

Sintering is the last stage of the process, providing the inter-particle bonding that generates the attractive properties from otherwise loose powder mass. During thermal debinding soaking the brown parts in an oven with a flux of a controlled atmosphere. This stage was mod-

eled by solving equations (31), (32) and (33). During this process backbone binder components are completely decomposed and transforms into gaseous state.

Considering that brown part has the same shape as a green one let us consider that the shrinkage has taken place during expelling backbone residual polymer. From simulation point of view this means that the brown part is described by heated continuum medium and the residual polymer expelling leads to shrinkage. As an example we consider that initial concentration of the this backbone polymer was $10^3$ $mol/m^3$. If we suppose that molecular mass of the degraded polymer is mainly determined by the polymer atoms we can have $M$ about several molecular unites (e.g. molecular mass of water 18 g/mol). For cubic cm of the sintering part volume the mass of the backbone binder will be 0.018 g, which is a pretty small value. If the mass of the specimens is several grams the residual mass of the backbone polymer has a mass about a thousand times smaller than metallic part.

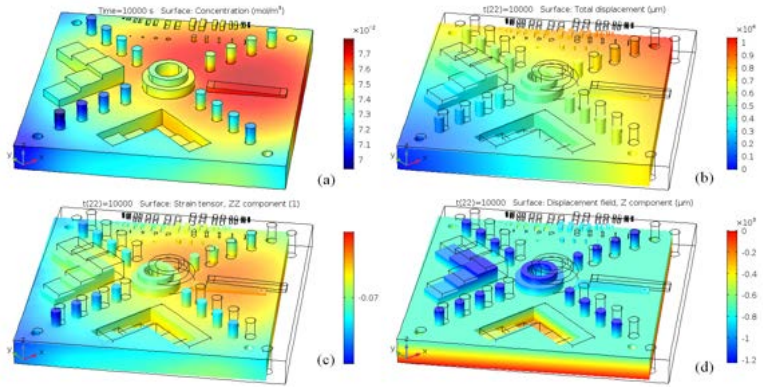


Figure 46. OMSOL simulations of the concentration of the backbone debinder in the sintering part (after sintering) – (a), Total displacement – (b), directional strain – (c) and displacement in vertical direction – (d). The $\beta = 10^{-3} m^3/kg$, initial concentration $10^3 mol/m^3$, diffusion coefficient $D = 4 \cdot 10^{-6} m^2/s$, brown part density was taken as $3000 kg/m^3$, Young modulus 10 GPa, Poisson ratio 0.4.

The result of shrinkage simulation for such case is presented in Fig. 44. One can see that during sintering backbone polymer concentration (degraded products of the polymer) changes for several orders and due to change of that the printed structure can experience shrinkage of about 10%. Similar simulation for a fixed boundary conditions at the bottom are presented in Fig. 45. One can see that the printed part might have enormous residual stress Fig. 45 (b) leading to higher shrinkage in vertical direction Fig. 45 (c).

Here, for example, we consider that initial backbone polymer concentration after green part expelling is set to $10^3 mol/m^3$. This value

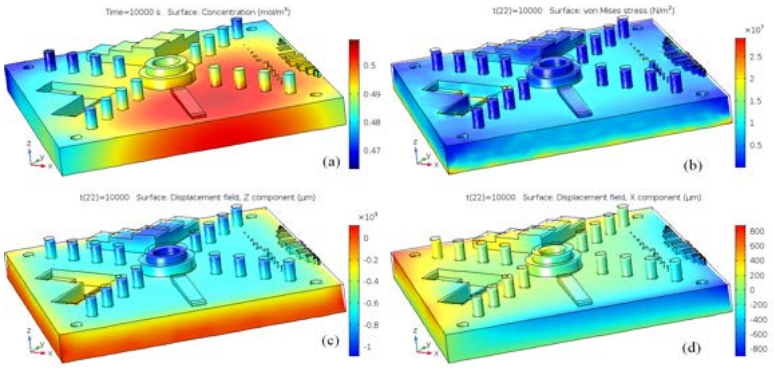


Figure 47. COMSOL simulations of the concentration of the backbone debinder in the sintering part (after sintering) – (a), Von-Mises residual stress – (b), directional displacement in vertical direction – (c) and in x one – (d). The $\beta = 10^{-3} m^3/kg$, intial concentration $10^3 mol/m^3$, diffusion coefficient $D = 4{\cdot}10^{-6} m^2/s$, brown part density was taken as $3000 kg/m^3$, Young modulus 10GPa, Poisson ratio 0.4.

was taken as reference for hygroscopic shrinkage swelling because all the stresses are assumed relaxed just after green part formation. The same system of equations (31), (32) and (33) can be used but in this case by gaseous binder concentration we can imply backbone gas and air concentration. The results of this modeling are presented in Fig. 46, 47.

As it was already emphasized green part and metal part have similar shape characteristics, but maintain the geometrical configuration features. This means that for the final part to have correct dimension one has to compensate the scale of the green part. It can be seen from the CAD plots 46 and 47 that all the features of the CAD are reproducible. Having the fixed boundary condition on the bottom we have deformable structure in vertical direction and inhomogeneous deformation parallel ton X-Y plane. The roller boundary conditions show the same shrinkage value in all three directions.

The shrinkage rate in the brown part depends on the swelling coefficient, which is a phenomenological parameter and should be determined by experiment for each composition. The shrinkage of the metallic part is a function of additional sintering stress, which is of the order of 0.1 - 3MPa and can be determined using microscopic simulation or measured by experiment.

## 3 Shrinkage Mechanism and discussion

The Mechanism for Anisotropic Shrinkage and Mechanical Properties can be explained based on the recent article [15], where the performed

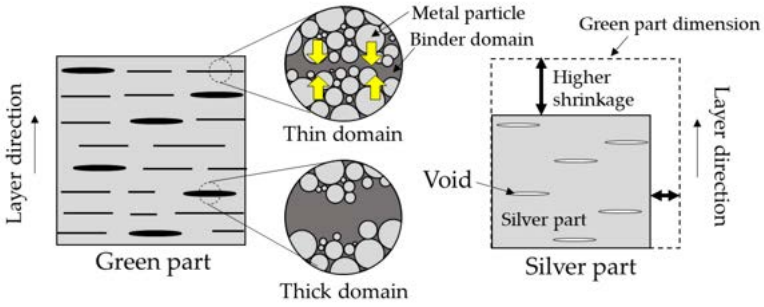


Figure 48. Illustration to explain the mechanism for the anisotropic shrinkage and mechanical properties [15].

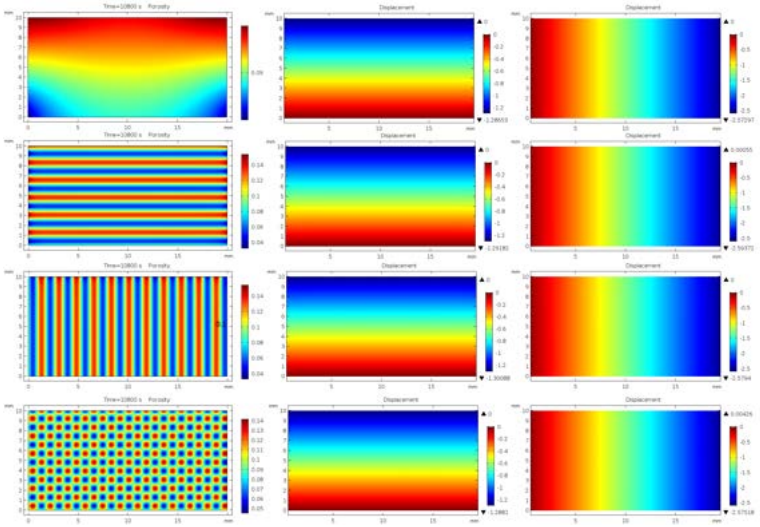

Figure 49. Illustration to explain the mechanism for the anisotropic shrinkage as a result of periodical void structures. Initial porosity distribution $\theta_0$ was 0.3 for the first row, $\theta_0 = 0.3(1 + 0.1sin(10^4 y)$ for the second raw, $\theta_0 = 0.3(1 + 0.1sin(10^4 x)$ for the third one, and $\theta_0 = 0.3(1 + 0.1sin(10^4 x)sin(10^4 y)$ for the last one, $\eta_0 = 10^{11}$ Pa·s, $\sigma_s = 0.5$ MPa, $\eta = 1 \times 10^{11}$ Pa·s, $\sigma_s = 1$ MPa. In all structures the averaged porosity distribution is about the same.

experimental results show that anisotropic shrinkage is a function of the initial porosity distribution Fig. 48 . Following this idea we studied such sintering approach based on Olevsky model (49) where first column is initial porosity distribution, second column is vertical displacement and third column is transverse displacement. First row is devoted to homogeneous porosity distribution and after sintering this case has the smaller shrinkage in vertical and horizontal direction. The second row shows the shrinkage simulation results for vertical periodic nonhomogeneous distribution. In this case lateral shrinkage is the largest. For

nonhomogeneous porosity distribution in the horizontal direction, vertical shrinkage is the largest. For periodic porosity distribution we have about the same shrinkage as for homogeneous porosity distribution (1st row). This is a qualitative simulation with small perturbation in the porosity value. In real experiments porosity is a pronounced function of the space with the value like 1 in a certain location (see [15]) and it is not modelled in this approach. However it correctly reflects the sintering property that initial value of porosity might lead to nonlinear shrinkage phenomena.

So, our conclusion is that porosity distribution itself cannot be the reason of the nonlinear shrinkage. This is some qualitative simulation with small perturbation in the porosity value. In real experiments porosity is a pronounced function of the space with the value like 1 in a certain location (see [15]) and it is not modelled in this approach. However it correctly reflects the sintering property that initial value of porosity might lead to nonlinear shrinkage phenomena.

Another question is that due to manufacturing process the sintering stress parameter may become anisotropic in certain direction. In fact, all directions during FDM are not equivalent, and this may change the sintering stress parameter. Considering that the sintering stress is higher in the layer direction we can easily get anisotropic sintering by using Olevsky model (Fig. 50 ). So, since in Olevsky model we have two major parameters (viscosity and sintering stress) the nonlinear shrinkage can arise as a results of these parameters variation. Figure 50 shows that any shrinkage can be explained based on variation sintering stress.

The same ideal about distribution of porosity was tested for the second model. Instead of homogeneous continuum we created cellular structure (Fig. 51). In such design we have open volumes between filaments (the paths of the fast diffusion transport for debinded backbone degraded polymer) and the concentration of the polymer becomes a couple orders less than concentration of the polymer of the homogeneous cube of the same size. However, we do not get any substation nonlinear shrinkage of such structure. Shrinkage in z and x (y) directions are about the same. This happened because porosity is a volumetric value and we use the isotropic coefficient of hygroscopic shrinkage (swelling) $\beta$. Using diagonal or symmetric form, where for example one component (such as z) is larger, we can easily get nonlinear shrinkage. This property does not depend on structure or microstructure explicitly. The matter is that microstructure arising during printing is still effecting shrinkage at the sintering stage by changing swelling coefficient in different directions (Fig. 52 and 53).

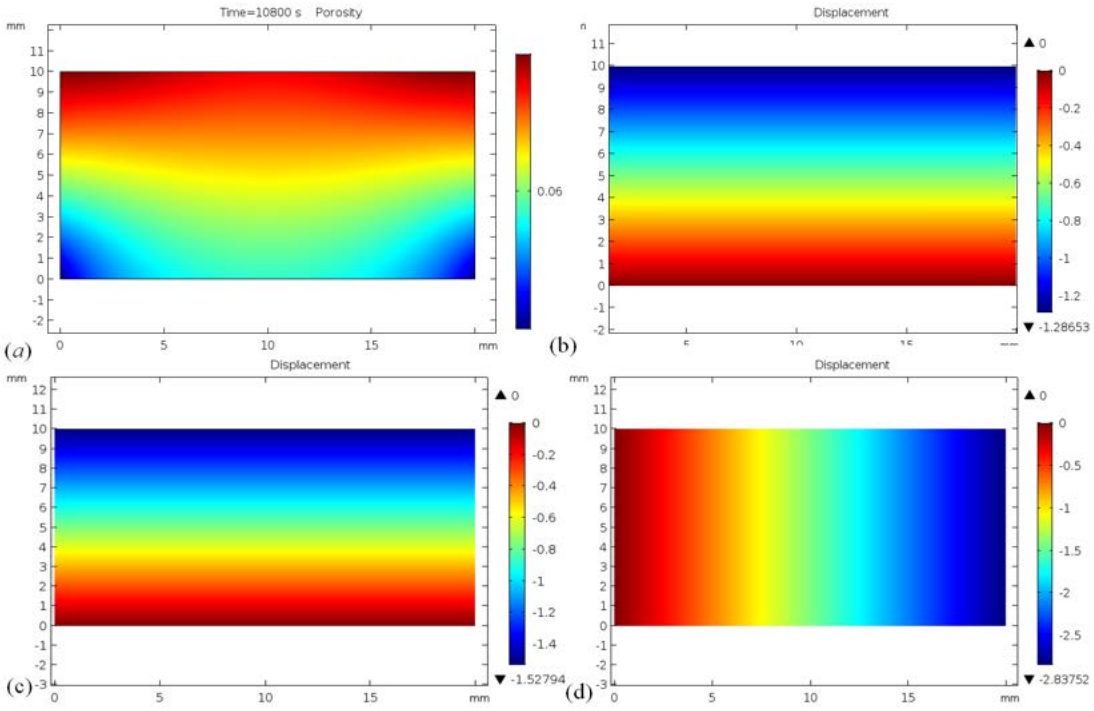


Figure 50. Illustration to explain the anisotropic shrinkage as a result of different value of sintering stress in two directions x and y. Initial porosity distribution $\theta_0$ was 0.3 , $\eta = 10^{11} Pas, \sigma_{sx} = 1MPa$, $\sigma_{sy} = 1.2MPa$.

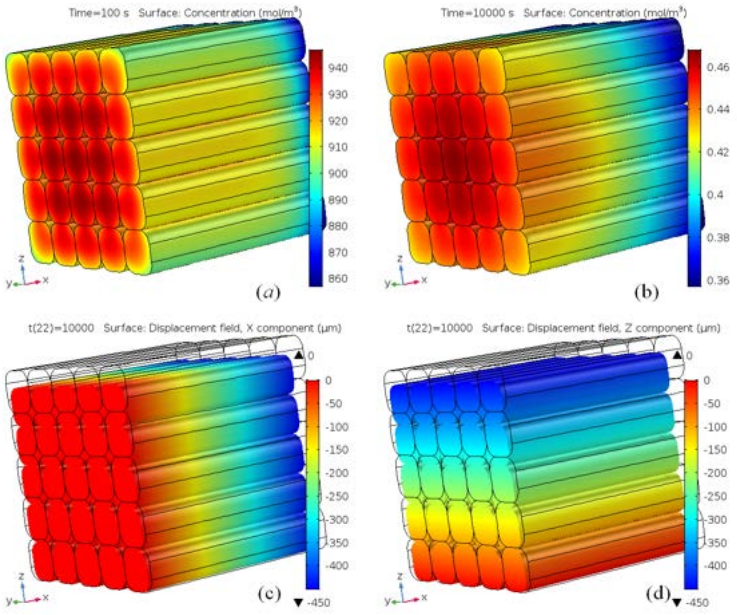


Figure 51. Concentration of the backbone degraded polymer at the beginning of the sintering (t=100s) – (a) and at the end (t=1000s) – (b), the value of shrinkage of the sample in the x direction – (c), vertical shrinkage (z direction) – (d) for isotropic shrinkage coefficient ($\beta = 0.005 m^3/kg$) and diffusion coefficient $D = 4 \cdot 10^{-9} m^2/s$. Computation is done for symmetric boundary condition in YZ plane for convenience of directional displacement calculation.

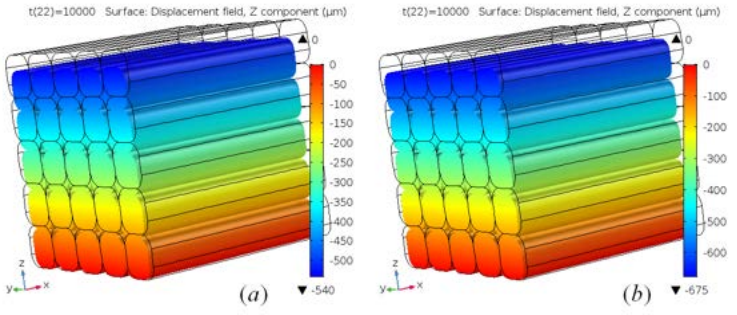


Figure 52. Continuation of the Fig. 51 vertical shrinkage (z direction) for anisotropic shrinkage coefficient in z component ($\beta = 0.006 m^3/kg$) – (a), shrinkage coefficient in z direction is ($\beta = 0.007 m^3/kg$) – (b). Computation is done for symmetric boundary condition in YZ plane for convenience of directional displacement calculation.

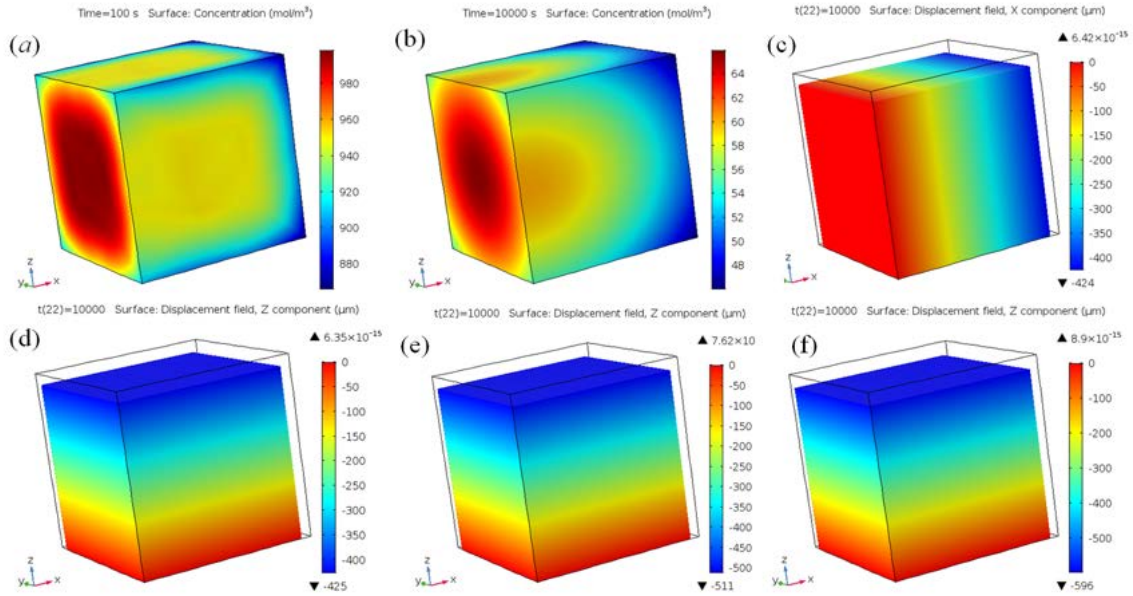


Figure 53. Concentration of the backbone degraded polymer at the beginning of the sintering (t=100s) – (a) and at the end (t=1000s) – (b), shrinkage of the sample in the x direction – (c), vertical shrinkage (z direction) for isotropic shrinkage coefficient ($\beta = 0.005 m^3/kg$) – (d), shrinkage coefficient in z direction is ($\beta = 0.006 m^3/kg$) – (e), shrinkage coefficient in z direction ($\beta = 0.007 m^3/kg$) – (f). Computation is done for symmetric boundary condition in YZ plane for convenience of directional displacement calculation.

## 4 Conclusion of Part VI

Two macroscopic models were developed for describing the sintering process. One is based on Olevsky approach and second one based on swelling (shrinking) the continuum due to concentration of backbone polymer. Both model show shrinkage property of the structure. If we do not prescribe different microstructure properties for the sintering stress or shrinkage coefficient we practically obtain isotropic shrinkage independent on initial porosity distribution (at least change in shrinkage for the continuum model is not substantial). Introducing anisotropic value of sintering stress or shrinkage coefficient, which might be due to morphology and microstructure of printed parts, we can explain any nonlinear shrinkage phenomena.

# Part VII
# Intelligent AM in space

In the next three sections we will provide a brief review of the current state of art in Machine Learning application to the additive manufacturing. In the final section of this part we will discuss a novel concept of intelligent AM in space.

## 1 Machine learning (ML) approach for prediction of nonlinear shrinkage [65].

As we have shown above, the unique multi-scale modeling approach developed in this work allows predicting many key parameters of sintering in BMD including anisotropic shrinkage of the whole part with complex geometry. However, these models rely on multiple phenomenological parameters that have to be tuned using experimental data. The tuning becomes even more important for space applications where distortion mechanisms may have a different physical nature. To make results of in space manufacturing experiment more informative and to further improve accuracy and reliability of predictions one could combine physics-based modeling with data-driven approaches using e.g. machine learning methods developed for additive manufacturing processes [65] to incorporate analysis of available experimental data [80].

Here we follow discussion of the machine learning in application to additive manufacturing of metals presented in recent work by [65] and [80]. For example, the current approach to printability analysis, determining which components are likely to build unsuccessfully, prior to manufacture, is based on ad-hoc rules and engineering experience [65]. Machine learning appears to be a convenient framework for determining geometric limits of printability [65] and more generally for application in solid-state material science [80].

Modern machine learning algorithms are able to learn highly complex nonlinear relationships between predictor and target variables, even in highly stochastic environments. Recent applications of machine learning to additive manufacturing [19,58] have focused on quality detection during or postmanufacturing or on optimisation problems around build process parameters [69,98].

The key component of the ML algorithm is the representation of the data using features that are able to capture all the relevant information, necessary to distinguish between different experimental setups [38]. For some methods the feature extraction can be considered as part of the model [22].

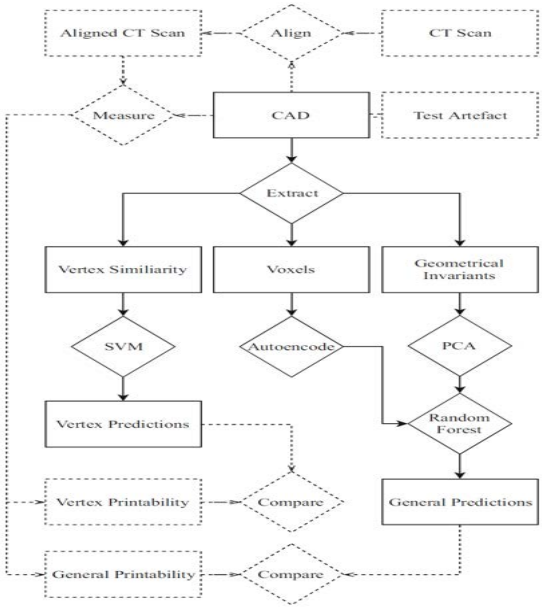


Figure 54. Workflows for algorithm for training (dotted and solid lines) and classification (solid lines). Rectangles denote variables and diamonds denote processing units [65].

**Methodology of ML.** For analysis of printability it is recommended [65] to use supervised ML algorithm that connects the predictor variables to the target variables. First, one has to construct the parts that generate these data. This process involves building and scanning custom components with a broad range of local geometries, especially those that limit capabilities of the additive manufacturing process.

Once custom parts are built, one has to extract invariants, which describe geometry in regions of interest and will form the input to the ML algorithm. To assess the printability of a given geometry, we measure the difference between our CAD and a computed tomography (CT) scan of the manufactured object.

Note that the additive manufacturing and scanning processes are both expensive and time-consuming, one has to develop efficient method to gain maximal information about the printability of various geometries for a small number of builds and scans. One of the requirements is to construct an artifact, such that any possible local geometry is sufficiently close to a local geometry exhibited in the artifact.

A general workflow of the ML algorithm proposed by [65] is shown in Fig. 54.

**Computer designed** components for additive manufacturing processes are typically specified as polyhedra: a solid with flat polygonal faces and straight edges. The theory of random convex polyhedra is well es-

tablished and by taking unions of such objects we can generate random (not necessarily convex) polyhedra.

**Alignment.** The conventional method used for the alignment is the iterative closest point (ICP) algorithm [23], with initial transformation given by applying Procrustes analysis [45] to a set of hand-picked landmark points.

**Geometry.** The industry standard for a CAD in additive manufacturing processes is a stereolithography file. This specifies a finite triangulated mesh $\partial T \in \mathbb{R}^3$: a collection of vertices $V$, edges $E$ and triangular faces $F$.

**Printability measure.** To assess the printability of a part, we need a numerical quantity which encodes the difference between our CAD $\partial T$ and the corresponding build $P$. We assume that the CT scan produces a faithful representation of the built component that is already locally aligned scan with CAD.

For each point $x \in \partial T$, one can define the Hausdorff printability measure as

$$\rho(x) = \inf_{y \in P} \| y - x \|_2 \in [0, \infty). \tag{37}$$

Next, for a fixed threshold $t$, one can define a point as problematic if $\rho(x) > t$ and printable if $\rho(x) \leqslant t$. The main advantages of this printability measure are its simplicity, computational ease and interpretability. The obvious drawback is that it is a point-wise measure of printability.

**Machine learning techniques.**

*Support vector machines* Certain machine learning algorithms naturally take as input a similarity measure, such as our vertex similarity measure. The major advantage of SVMs is their *sparsity*: to make predictions we only need to compute our similarity measure with a small subset of the training data.

*Random forests* are built as an ensemble of extremely simple rule based classifiers, known as decision trees, which require limited data preprocessing and are easily interpretable. However, to learn complex structure decision trees must be grown very deep and often have poor generalisation performance.

*Principal component analysis* Many classification algorithms are subject to the curse of dimensionality. To alleviate this issue one can employ principal component analysis, a linear technique which transforms observations of possibly correlated variables into uncorrelated variables known as principal components.

*Data augmentation* Out of the box supervised learning algorithms often struggle with imbalanced datasets. To overcome this issue one can use synthetic minority over-sampling technique.

**Model selection.** To study which particular predictive models and corresponding hyperparameters perform best, one needs a metric to assess the resulting performance. The problem of labelling areas of CAD as printable or problematic is an example of an imbalanced learning problem; the number of printable regions will in general drastically outweigh the number of problematic regions.

The conventional measure of performance – accuracy – is ill-suited in the imbalanced situation, i.e. this metric will simply predict high accuracy for all samples. A more appropriate measure can be introduced if $F_\beta$ accounts for true and false positives and true and false negatives denoted by **tp**, **fp**, **tn** and **fn** respectively.

$$F_\beta = (1+\beta^2) \cdot \frac{precision \cdot recall}{(\beta^2 \cdot precision + recall)} \tag{38}$$

where *recall* is **tp**/(**tp** + **fp** ) and *precision* is **tp**/(**tp** + **fn** ), while $\beta$ controls the relative importance of recall and precision; increasing $\beta$ will increase the likelihood of correctly capturing all problematic regions.

**Build process.** In the work [65] The manufacturing of the test artefact was carried out using an electron beam melting (EBM) system, ARCAM S12. Loaded with Ti6Al4V pre-alloyed powder as feedstock material, the size distribution was reported to be 45-106 µm under the batch 1250 specifications supplied by ARCAM Gothenburg Sweden.

**Scanning procedure.** Following manufacture, the geometry of the sample was analysed by X-ray Computed Tomography (CT) in the Henry Moseley X-ray Imaging facility at the University of Manchester. 3D data was reconstructed from the 2D radiographs using a filtered back projection algorithm and proprietary Nikon software. The voxel size calculated automatically by the Nikon software was 40 µm.

**Vertex printability.** To predict printability one can use both the threshold $t$ for marking a point as printable or problematic and the value of $\beta$ to optimise our $F_\beta$-metric. Note that values of $t$ and *beta* are heavily application dependant and has to be determined by the mission requirements. In the work the values $t = 0.5$ mm $\beta = 2.0$ were fixed for all predictive experiments.

## 2 Estimation of nonlinear shrinkage using neural networks (NN) [54].

One of the major problems of the sintering process is to estimate the anisotropic shrinkage of the powder geometry and shape deformation during powder consolidation and approaches range from rules of thumb to sophisticated finite element modeling. However, the industry still lacks a reliable and general way to accurately estimate final shape [54]. One of the promising approaches is based on neural networks that *combines pre-processing dimensions, powder characteristics and processing information to estimate post-processing dimensions*. Compared to nonlinear regression models to estimate shrinkage, the neural network models perform well and have a potential to optimize processing parameters and reduce operating costs.

**Processing.** In the powder metallurgy (P/M) process, parts are made by compacting metal powder using high pressure and/or temperature. Isostatic pressing, where pressure is uniformly applied from all directions (isostatic) in order to achieve uniform compaction, has become widely accepted as an effective method for compaction. HIP is the application of pressure (approximately 15,000 psi) at temperatures usually greater than 70% of the melting temperature of the material.

[**loading** ] the container is vibrated to reduce porosity and achieve uniform powder packing $\sim$ 70% dense[2].
[**outgassing** ] residual gases are pumped out as the container is heated.
[**compaction** ] pressure and heat are simultaneously applied until the powder is consolidated to full theoretical density.

To achieve the benefits of near net-shape, the shrinkage during the HIP process must be estimated accurately. If shrinkage is overestimated, additional machining will be required and expensive powder will be wasted. If it is underestimated, the part may be scrapped. Shrinkage is difficult to estimate because parts do not shrink uniformly and shape distortions may occur due to the structural design of container and/or the filling uniformity of the powder. Model of shrinkage will help in design, reduce cost, and time of manufacturing.

Traditional approach is mainly based on trial-an-error basis. If isotropic shrinkage is assumed, relative linear shrinkage $S$ for a solid cylinder can be given as follows

$$S = \frac{V_C + V_p \rho}{V_C + V_p}$$

where $V_C$ and $V_p$ are the container and particle volumes respectively an $\rho$ is the ration of packing density to theoretical density.

[2] They most likely overestimated the density

The following factors were found to affect anisotropic shrinkage

- packing density and variations in powder density
- relative container thickness and aspect ratio(length/diameter)
- pressure and heating rate during the HIP cycle
- position of container welds
- material parameters of the powder and container.

Using these factors authors of [90] developed an empirical model to predict post-HIP dimensions of solid/hollow cylindrical and rectangular shape containers with between 0.6±1.0% dimensional accuracy. There were several macroscopic (at the level of continuous compact) and microscopic (at the level of individual particles) approaches develop to model this process. These models, however, are expensive to develop, and still require experimental input to improve accuracy of predictions.

**Data.** The current project focused on a specific nickel based superalloy formed in solid cylinders. A repository consisting of the relevant historical HIP data was created in a relational database. After preprocessing the historical data 200 observations were left for model development and validation.

The characterization of the manufacturing parameters included

1. Sample and container geometry;
2. wall thickness;
3. packing ratio (PR) of the powder;
4. processing stages: pressure, temperature, duration;
5. location of the heaters and placement of the containers;
6. geometry of the processed container and sample.

**Constructing Neural Networks.** Seven feed-forward NN models with two hidden layers were constructed (and trained using backward-propagation algorithm) to predict post-HIP dimensions. In the selection of the independent variables, the relevant pre-HIP dimensions and packing ratio were always used. Then, a step-wise regression was carried out to identify the significant process variables for each post-HIP dimension. A ten-fold cross validation approach was used that leverages all data by using each observation for both model construction and, independently, model validation. The validation network was trained on 180 observations and tested on the remaining 20 observations.

It was shown that the NN method yields on average 13% accuracy for predictions of the length shrinkage and ~20% accuracy for predictions of the curvature changes.

The AM design-to-product transformation cycle based on decision support needs and ML opportunities is illustrated in Fig. 55.

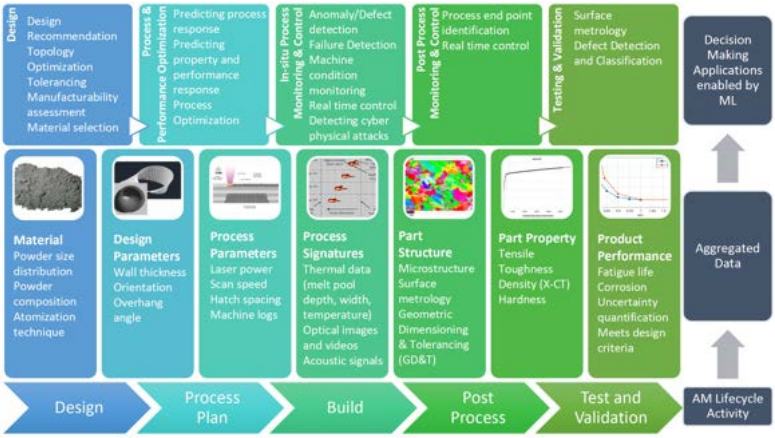


Figure 55. AM Lifecycle, Examples of Associated Data, and Decision Making Applications. [74]

In the work [74] the following four categories of AM life-cycle were selected: 1) Design, 2) Process and Performance Optimization, 3) In-Situ Process Monitoring and Control, and 4) Inspection, Testing and Validation. Within each category authors highlighted a few AM function that can significantly gain performance due to ML application.

## 3 Neural-Network-Based Machine Learning for Additive Manufacturing [90]

**Additive manufacturing** (AM), also known as three-dimensional printing is an important technology with wide range of applications. However, AM processing parameters are difficult to tune, since they can exert a huge impact on the printed microstructure and on the performance of the subsequent products. It is a difficult task to build a process-structure-property-performance (PSPP) relationship for AM using traditional numerical and analytical models. This paper (in reference [90]) overviews the progress of applying the NN algorithm to several aspects of the AM whole chain, including model design, in situ monitoring, and quality evaluation. However, AM parts also present dozens of unique defects that differ from those that appear in their cast and wrought counterparts; these include

- porosity due to a lack of fusion and gas entrapment,
- heavily anisotropic microstructure in both the perpendicular and parallel directions relative to the printing direction,
- distortion due to large residual stress introduced by a high cooling rate and steep temperature gradient.

The AM process always involves many essential parameters that can determine the final product's performance but the relationship between

these parameters and the output quality is too complicated to fully understand. For example selective laser sintering is a multi-physics and multiscale process that includes powder laser interaction at the microscale, melt pool dynamics and columnar grain growth at the mesoscale, and thermal-mechanical coupling at the macroscale.

**Neural networks.** Many theoretical and numerical models focus on one of the scales and concentrate on only one or two aspects of the whole process. As a result there is a lack of an in-depth understanding of AM. It is currently impractical to predict the whole AM process quickly and accurately via these physics-driven methods in a short time.

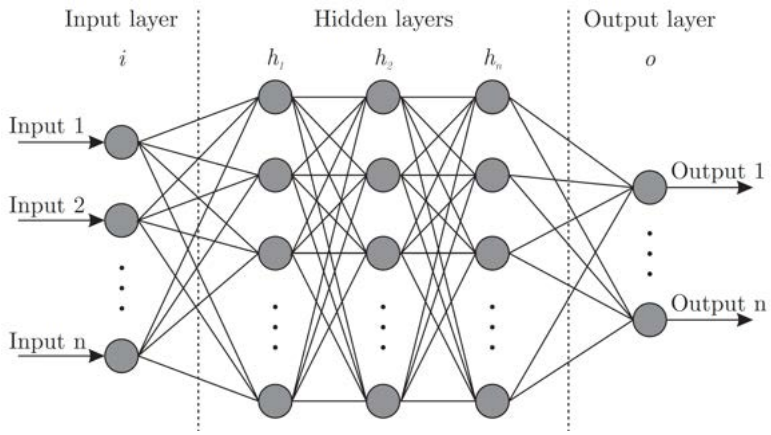


Figure 56. Artificial neural network architecture (ANN i-h1-h2-hn-o).

Alternatively, one can develop data driven models to relate process parameters to the manufacturing outcome. An advantage of such models is that they do not need to construct a long list of physics-based equations; instead, they automatically learn the relationship between the input features and output targets based on previous data.

There are various kinds of AM technologies that produce different kinds of data sheets. How to organize these data with a unified format and integrate the data-flow into the subsequent ML algorithms is a challenging task. In an NN algorithm, the data is labeled – that is, the method is supervised the model has been told the "answer" to the inputs. This is suitable for an AM case, since there are always clear targets and qualification methods for this manufacturing technique. It has been shown that even a network with only one hidden layer but sufficient number of neurons can express an arbitrary function.

The structure of the NN is shown in Fig. 56. Each layer consists of nodes or neurons. The coefficients in NN (weights), and represent the connection magnitudes between neurons in adjacent layers. The values

of weights are determined by training the NN iteratively [3], in order to minimize the loss function between predictions and actual outputs. For applications of the NN to AM the multilayer perceptron (MLP) seems to be most appropriate NN; its common mathematical operations are linear summation and nonlinear activation (such as the sigmoid function). It is widely used in dealing with tabular data. A detailed setting of the NN usually consists of: (i) number of hidden layers; (ii) number of neurons in one layer; (iii) activation function; and (iv) loss function.

**Design for AM.** AM is a value chain incorporating many aspects: model design, material selection, manufacturing, and quality evaluation. Design for AM (DfAM) involves building a CAD model of AM parts. An NN algorithm can be used to directly compensate the part geometric design, which helps to counterbalance thermal shrinkage and deformation in the manufactured. This process involves [29]: (i) A CAD model of the required part is prepared, and its surface 3D coordinates are extracted as the input of the NN model; (ii) a thermomechanical finite-element analysis software is used to simulate the AM process with a defined set of process parameters. The deformed surface coordinates are extracted as the output of the NN model; (iii) an NN model with mean square error (MSE) as the loss function is trained to learn the difference between the input and output; and (iv) the trained network is implemented to STL file to make the required geometric corrections so that manufacturing the part using the modified geometry results in a dimensional-accurate finished product.

In [53] a strategy which employs neural networks and deep learning to predict the maximum stresses in the realm of linear elasto-plasticity of a detail-level finite-element model was presented and demonstrated on a single lattice cell specimen.

**In situ monitoring.** In situ monitoring for data acquisition from multiple sensors provides first-hand information regarding product quality during the AM process. If these real-time data can be analyzed synchronously and accurately, complete open- [94] or closed-loop [92] control for manufacturing can be realized. The data source for these methods can incorporate three types, including one-dimensional (1D) data (e.g., spectra), 2D data (e.g., images), and 3D data (e.g., tomography).

**Processpropertyperformance linkage.** From a technological and economic point of view, process parameter selection for the optimization of the performance of AM parts is highly desirable. Constructing a direct linkage between process, property, and performance is therefore of great interest. For example FDM process parameters such as layer thickness, orientation, raster angle, raster width, and air gap can be

[3] Using e.g. one of the most popular methods called *back propagation*

linked to the performance values such as compressive strength [83] and dimensional accuracy [82].

**Challenges for AM applications.** At present challenges of ML applications for AM include small data sets, difficulties in labeling data and feature selection, problems with overfitting and underfitting. All these issues are mostly related to the lack of knowledge, experience, and data accessibility between different groups.

**Future perspectives.** There is a need for a unified approach to data acquisition, preprocessing, well-defined characterization of processing parameters, and testing standards, and data-base construction across different research groups.

Important future applications of the ML for additive manufacturing include development of AM unified standards for sensors hardware and software; implementing closed-loop control of AM using neural network algorithms, applying NNs for building the relationships between structure-property and process-property, and combining traditional physics-based models with ML algorithms for improved accuracy of predictions and process-property-performance linkage.

## 4 Intelligent AM in space. [52]

Current state of art in application of neural networks for additive manufacturing allows one to put forward a concept of intelligent AM that combines traditional physics-based approaches and numerical methods with data-driven algorithms and techniques. These ideas are in agreement with recently proposed paradigm of theory-guided data science (TGDS) for integrating physics-based models and data-driven models proposed in [52]. The overarching goal of intelligent AM is to introduce scientific consistency as an essential component for machine learning of AM models.

Within applications of this paradigm to BMD processing one has to combine physics-based multi-scale models (including Molecular dynamics, Phase field methods, Discrete element modeling, Kinetic Monte Carlo simulations, and Finite Element models) with data-driven approaches.

There are two primary reasons that have prevented data science models from reaching the level of success achieved in commercial domains. First, scientific problems are often under-constrained in nature as they suffer from paucity of representative training samples.

The second primary reason is that data science model require translation of learned patterns and relationships to interpretable theories and hypotheses that leads to advancement of scientific knowledge, e.g.,

by explaining or discovering the physical cause-effect mechanisms between variables. (i.e. learned patterns have to be explained scientifically to be used in design and planning.) Further, theoretical models prevent learning spurious patterns.

Hence a novel paradigm is required that uses the unique capability of data science models to automatically learn patterns and models from large data, without ignoring the accumulated scientific knowledge - theory-guided data science (TGDS) [52]. Examples demonstrating potential of this approach include the discovery of novel climate patterns, closure of knowledge gaps in turbulence, discovery of novel compounds in material science, design of density functionals in quantum chemistry, a recent IBM Research initiative on physical analytics.

**The conventional approach** is to use models based on scientific knowledge, i.e., theory-based models, which encapsulate cause-effect relationships between variables that have either been empirically proven or theoretically deduced from first principles. There is a wide range of models including analytical, finite element, finite difference, molecular dynamics, discrete element methods.

**A data driven approach** is to use a set of training examples involving input and output variables for learning a data science model that can automatically extract relationships between the variables.

**Objective** of model performance in TGDS can be summarized as [52] **Performance Accuracy + Simplicity + Consistency** The main research themes of TGDS can be formulated as:

- scientific knowledge can be used in the design of model families to restrict the space of models to physically consistent solutions;
- given a model family, we can also guide a learning algorithm to focus on physically consistent solutions. This can be achieved, for instance, by initializing the model with physically meaningful parameters, by encoding scientific knowledge as probabilistic relationships;
- the outputs of data science models can be refined using explicit or implicit scientific knowledge;
- another way of blending scientific knowledge and data science is to construct hybrid models, where some aspects of the problem are modeled using theory-based components while other aspects are modeled using data science components;
- data science methods can also help in augmenting theory-based models to make effective use of observational data.

| SCALES and METHODS | INPUTS | Available EXP data |
|---|---|---|
| Quantum chemistry and MD: **nsec** and **nm**. A few particles. | Interatomic potential, alloy composition | Surface energies, diffusion coefficients, viscosity, surface tension |
| Phase-field and kinetic Monte Carlo models. **Tens of $\mu m$** and **hours**. Several particles. | $\delta_{gb}$, diffusion coefficients, surface and grain boundary energies | Microstructure evolution, dimensional changes, shrinkage, Young moduli |
| Discrete element methods and kinetic Monte Carlo (**hours** and **mm**). Thousands of particles. | Elastic and viscous forces | Microstructure images, shrinkage data |
| Continuous finite element methods. (**hours** and **full part**) | Viscosity, sintering stress, spatial mass distribution | Dimensional changes for multiple structures, shrinkage, strength |

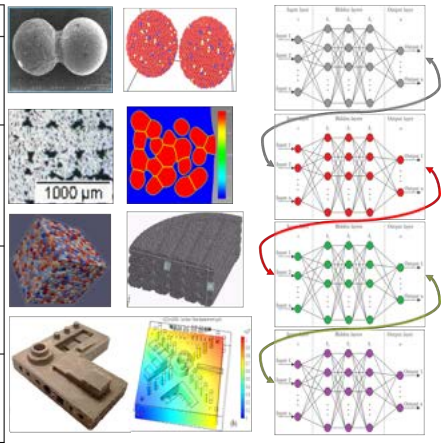


Figure 57. Sketch of application of intelligent AM to bound metal deposition modeling.

Application of intelligent AM to BDM technology can be briefly sketched as shown in Fig. 57. This figure shows how multi-scale approach developed in this work can be naturally decomposed into modular sub-problems, each of which represents a different physical subprocess. For each sub-problem a separate neural network can be constructed to tune model parameters using experimental data. On each scale parameters of the network can be corrected using accumulated scientific knowledge. The output of neural-network for one scale can be used to correct input and hyper-parameters at other scales.

To conclude this section we note that usually the physics-based and data-driven approaches to the problem are considered as alternatives on the ground that each approach has its own limitation. We believe that the real power of both methods can be only revealed by integrating complimentary strength of both methods with intelligent AM in space (IAMS). Application of the IAMS goes far beyond BMD technology and can be used for many other techniques of additive manufacturing in space. Our group is actively developing general framework for analysis of complex physical problems using a hybrid approach that combines machine learning and partial differential equations and has strong background for future work on intelligent AM.

# Part VIII
# Conclusions

We have performed analysis of nonlinear shrinkage and numerical methods that allow estimating anisotropic dimensional change during sintering in bound metal deposition process. To enable prediction of anisotropic shrinkage we developed a unique multi-scale sintering model and proposed a novel concept of intelligent additive manufacturing for BMD process.

Our multi-scale model includes several numerical methods

- estimations of anisotropic shrinkage based on mathematics of compact spherical and granular particles, Sec. II;
- Molecular dynamics of sintering of Ti6Al4V particles with diameter a few tens of nanometers on the scale of nanoseconds, Sec. III;
- Phase-field methods of sintering metal particles in 2D and 3D on the scale of tens of microns (cross-section or one filament) and time scale of hours, Sec. IV;
- Discrete element modeling of sintering on the scale of millimeters (sub-models) formed by tens of thousands particles on time scale of tens of minutes, Sec. V;
- Continuous Finite Element modeling of the whole part on the time scale of several hours, Sec. VI.

We have also briefly considered results of Kinetic Monte Carlo simulations of sintering, see Appendix E and Sec. 6.3. Below we provide brief conclusions for each of methods.

**Estimations based on packing and filling densities – Sec. II.** We have performed analysis of shrinkage of a vertical cylinder as a function of packing densities of particles and filling densities of the filaments. According to these estimations the key contribution to the nonlinear shrinkage is due to gravity. The samples with initial densities $\lesssim$61% are most affected by the non-linearity and the smaller is initial density the larger is non-linearity. Once samples approach density of the order ~61-63% subsequent densification on the ground is uniform.

The limiting value of the density is determined by the experimental fact that this is maximum density achievable without special effects such as e.g. vibration. Subsequent densification can only happened via necking, grain formation and growth [37] and is predominantly uniform. Exceptions are possible due to complex shapes, proximity of the walls, narrow walls, sharp features etc.

It is therefore important to ensure that initial density of samples at the sintering stage is of the order ~62%. And we conclude that the use of such a high density metallic powder in green samples will minimize distortion in zero gravity.

We note, however, that in zero gravity there may be additional mechanisms of significant distortion of the part shape for low initial density, sharp features, and narrow walls 2.2.

**Molecular dynamics – Sec. III.** Molecular dynamics simulations were developed to estimate important sintering parameters including width of the grain boundary and diffusion coefficients. In particular, it was shown that the grain boundary width $\delta_{gb}$ is around 1.0 µm for particles with diameter ~30 µm while the surface diffusion coefficient $D_{surf}$ was estimated to have a value ranging from $\approx 8 \times 10^{-10}$ m$^2$/sec to $1.6 \times 10^{-9}$ m$^2$/sec.

Despite the fact that the method can at present only a few particles with diameter $\lesssim$50 nm it offers unique opportunities in estimations of the key sintering parameters grain boundary width, diffusion coefficients, surface energies, and viscosities. We emphasize that these parameters are fundamentally important for the next scale of sintering simulations using phase-field method (Sec. IV). They are also used in theories including Coble (Sec. C), Wakai (Sec. D), and in the Master sintering curve method (Sec. F). It is further expected that the MD will be able to handle larger numbers and diameters of particles in the near future due to ongoing hardware and algorithms development.

**Phase field methods – Sec. IV.** At the next scale we simulate microstructure evolution in the cross-section of one filament using phase-field model of sintering [25, 26, 93]. This approach allows to model sintering up to 30 "particles" with diameter of the order of 10-20 µm in 2 dimensions and to cover the time scale corresponding to the transformation from particulate to dense granular structure of the samples. In 3 dimensions the number of particles is limited to ~10 and the system dimensions to ~ 20×20×20 µm$^3$. Phase-field model relies on parameters $\delta_{gb}$ and $D_{surf}$ estimated using MD simulations. This model also involves a number of phenomenological and experimentally available parameters of the system of particles. Using this approach we estimated value of sintering stress to be a few MPa and the time scale of sintering to be a few hours. This is in good agreement with experimental observations and numerical estimations based on the kinetic Monte Carlo method.

The value of the sintering stress is further used for finite element modeling of the whole part. The finite element model also requires estimations of the spatial mass distribution as an input parameters of the simulations. Estimation of this parameter was obtained using discrete element approach.

**Discrete element model (Sec. V)** was used to model initial rearrangement of the particles and spatial mass redistribution at the meso-scale

of the order ~10×10× 10 $mm^3$. Using this approach we modeled a small sections of the whole part that takes into account the layout of the filaments. This model allows to simulate several thousands particles (up 150,000 in one case) with diameter 50 µm. The model was build using discrete element method in KRATOS Multiphysics [33, 34].

The DEM simulations revealed a few important trends. In zero-G dependence of the shrinkage on filament layout is very weak. On average (for various system parameters) the shrinkage is slightly larger for samples with unidirectional layout as compared to cross-layout. This trend is much pronounced for samples with decreased density.

At the same time we found that gravity is the major source of strong non-linear shrinkage. In particular, shrinkage in vertical direction was found to be ~22.7% for initial density 40% (corresponding to filaments case), while in horizontal direction shrinkage remained very weak.

The results of simulations were also used to estimate sintering stress at the level of 0.3 MPa, which is smaller than estimations obtained using phase-field method and sets the lower bound on the value of sintering stress.

In addition, this model was used to estimate nonuniform spatial distributions of solid matter in the samples. These data together with estimations of sintering stress are further applied for simulations of full scale continuous models.

**Full scale Finite Element model** (Sec. VI) was developed to predict anisotropic shrinkage during debinding and sintering in bound metal deposition process using COMSOL. The model can simulate different stages of debinding and sintering of the whole part as a function of the processing parameters: pressure, temperature, duration. Two macroscopic models were developed for describing sintering process. One is based on Olevsky approach and second one based on swelling (shrinking) the continuum due to concentration of backbone polymer. Both model show shrinkage property of the structure.

It was shown that besides gravity boundary conditions is an important factor of anisotropic shrinkage. The model depends on the number of phenomenological and experimental parameters that can be estimated with developed multi-scale approach including sintering stress, diffusion coefficients, viscosity, non-uniformity of the mass distribution etc. The model can predict anisotropic shrinkage and determine required compensation for the green part.

**Intelligent AM in space.** The developed multi-scale model is unique in the sense that it covers the whole spectrum of scales defining the physics of the sintering problem spanning from atomic dynamics, microstructure evolution, rearrangement of the particles at meso-scale, and shrinkage of whole part. Each model is quite complex and usually the

research is focused on one of these models. Here we developed the whole set of models and analyzed coupling between them. However, all these models depend on a large number of parameters that have to be tuned using experimental data. Such tuning is also required for more accurate predictions of the nonlinear shrinkage and successful application of additive manufacturing in space. To incorporate experimental data into multi-scale model we propose concept intelligent additive manufacturing in space (IAMS).

The idea of the IAMS is based on the analysis of developed multi-scale model, successful applications of data-driven algorithms to additive manufacturing of metal powders and on the recently introduced paradigm of theory-guided data science.

It is proposed to combine within the IAMS strength of both data-driven and physics-based methods thus taking the best of both technique. Conceptual design of the IAMS involves hierarchical structure of artificial neural networks (ANN) that can individually tune parameters of each sub-model of the multi-scale model and are connected to each other via input-output coupling of the model parameters. In turn scientific knowledge is encoded as relationships that correct parameters of the ANN and restrict the space of ANN models to physically consistent solutions.

We believe that IAMS has a strong potential for the future space applications owing complexity of AM and paucity of related experimental data in zero-G. In this situation IAM has a capability to incorporate in the most efficient way both experimental data and a wealth of scientific knowledge obtained on the ground into development of advanced space applications.

# Appendices

## A Modified Pokluda-Frenkel model

The main idea of the Frenkel-Pokluda (PF) model [71] is to equate the work by viscous forces $W_v$ for Newtonian fluids [4]

$$W_u = \iiint_V \eta \nabla u : \left(\nabla u + \nabla u^T\right) dV \tag{A.1}$$

to the work of surface tension

$$W_s = -\Gamma \frac{dS}{dt}. \tag{A.2}$$

Here $\nabla u$ is the velocity gradient

$$\nabla u = \begin{bmatrix} \frac{\dot{\epsilon}}{2} & 0 & 0 \\ 0 & -\dot{\epsilon} & 0 \\ 0 & 0 & \frac{\dot{\epsilon}}{2} \end{bmatrix},$$

$\eta$ is the viscosity, $V$ is conserved volume of two particles, $\Gamma$ is the coefficient of surface tension, $S$ is the surface area of sintered particles that is changing in time, and $\dot{\epsilon}$ is the strain rate

$$\dot{\epsilon}_{ij} = \frac{1}{2A} \int_A \left( \frac{\partial u_i}{\partial x_j} + \frac{\partial u_j}{\partial x_i} \right) dS. \tag{A.3}$$

The key question of any sintering model is the rate with which particle volume diffuses across the plane of the interface. In the Frenkel-Pokluda model the change of the volume is related to the velocity $u$ characterizing the growth of the neck [89] between the particles $u = \dot{x}_2/x_2$.

The original PF model assumes that the volume of the particles diffused across the interface is evenly distributed along the remaining surface of the particles increasing their radius. To unite the FP model with Cobel model [31]. We will modify the FP model in two ways. Firstly, we will assume that the diffused mass will accumulate at the neck. Secondly, we will limit analysis by relatively small radii of the neck.

The surface area (SA) of the system of two particles is the sum of the SA of the neck cylinder with radius $x_2$ and two spheres without the caps with heights $\rho_1 + y_1$ and $\rho_2 + y_2$, see Fig. A.1

$$S = 4\pi\left(R_1^2 + R_2^2\right) - 2\pi R_1\left(\rho_1 + y_1\right) - 2\pi R_2\left(\rho_2 + y_2\right) + 2\pi x_2\left(\rho_1 + \rho_2\right) \tag{A.4}$$

or in Coble [31] approximation (see next subsection)

$$S = 4\pi\left(R_1^2 + R_2^2\right) - 2\pi x_2^2 + \frac{\pi}{2} x_2^3 \left(\frac{1}{R_1} + \frac{1}{R_2}\right)$$

[4] The double dot (or scalar, or inner) product produces a scalar

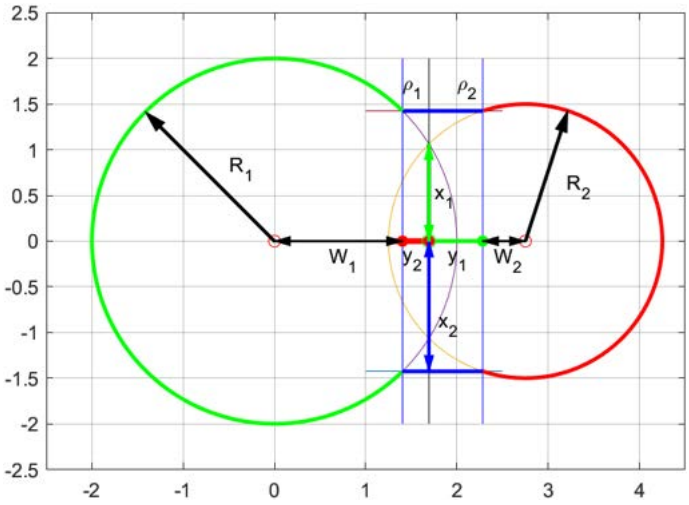


Figure A.1. Main characteristics of the overlap between two spheres.

The resulting work of surface tension is

$$W_s = \Gamma\left(4\pi x_2 - \frac{3\pi}{2R}x_2^2\right)\dot{x}_2. \tag{A.5}$$

The work of the viscous force is

$$W_u = \iiint_V 3\eta\dot{\epsilon}^2 dV = 3\eta\left(\frac{\dot{x}_2}{x_2}\right)^2 V_0, \tag{A.6}$$

where $V_0 = 4\pi/3(R_1^3 + R^3)$ is the conserved volume of the two spheres and the strain rate $\dot{\epsilon}$ is given in [89] $\dot{\epsilon} = \frac{\dot{x}_2}{x_2}$.

Equating $W_s$ and $W_u$ we obtain equation for $x_2$ in the form

$$\dot{x_2} = \frac{\pi x_2^3 \Gamma}{3\eta R V_0}\left(4R - \frac{3}{2}x_2\right) \tag{A.7}$$

# B Phase field models: example of parameters [24]

The motion of phase boundaries has attracted interest since the early nineteenth century. The boundary conditions for a solution set of differential equations are explicitly defined at the phase interfaces in these approaches. However, solving these sets of nonlinear expressions turns out to be extremely difficult, stemming from the interface interactions with various complex processes (such as merging, dissolution, and breakup) during the course of phase transformations.

Phase-field modeling overcomes these difficulties through inclusion into its formulism of a different interface description. A phase-field

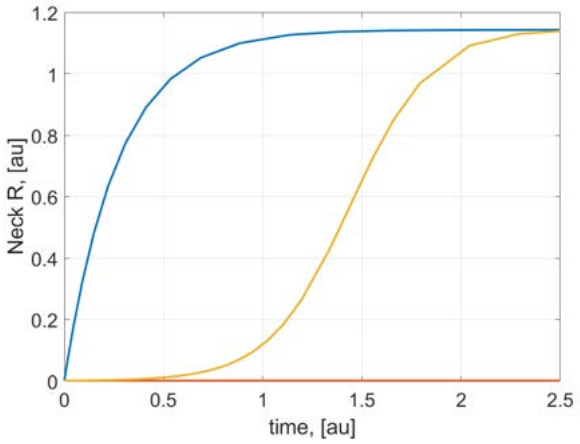


Figure A.2. Example of the neck radius dependence on time for modified Pokluda-Frenkel theory with force (left to right): $\propto x_2^0$; $\propto x_2^1$; and $\propto x_2^3$ .

model describes a microstructure (both the compositional and/or structural domains) with a set of field variables.

The field variables are assumed to be continuous across the interfacial regions, which is opposite of that in sharp interface models where they are discontinuous. There are two types of field variables: conserved and non-conserved.

The temporal evolution of the conserved field variables that is governed by the CahnHilliard nonlinear diffusion equation

$$\frac{\partial c_i}{\partial t} = \nabla M_{ij} \nabla \frac{\delta F}{\delta c_i(r,t} \tag{B.8}$$

and the non-conserved field variables evolve with the AllenCahn relaxation equation or time-dependent GinzburgLandau equation

$$\frac{\partial \eta_p}{\partial t} = -L_{pq} \frac{\delta F}{\delta \eta_q(r,t} \tag{B.9}$$

where $r$ is the position, $t$ is the time, $M_{ij}$ is the diffusivities of the species, and $c_1, c_2, ..., c_n$ are conserved field variables. $L_{pq}$ is the mobility of the non-conserved field variables, $\eta_1, \eta_2, ..., \eta_m$.

## B.1 Example of tungsten

Example parameters used in the phase model of sintering tungsten particles are shown in Fig. B.3 and B.4. We note that all the coefficients are exponetial functions of temperature and very strongly depend on concentration of dopands on the scale of 1 %.

**Table 3**
Mobility calculation for tungsten.

| GB mobility [42] | | | Surface mobility [44] | | | Volume mobility [43] | | |
|---|---|---|---|---|---|---|---|---|
| Diffusion prefactor ($cm/s^2$) | Activation energy (ev) | Mobility ($\mu m^5/ev\ s$) | Diffusion prefactor ($cm/s^2$) | Activation energy (ev) | Mobility ($\mu m^5/ev\ s$) | Diffusion prefactor ($cm/s^2$) | Activation energy (ev) | Mobility ($\mu m^5/ev\ s$) |
| 0.141 | 3.04 | $3.69 \times 10^{15}$ | 4.0 | 3.14 | $3.98 \times 10^{15}$ | 0.04 | 5.4 | $1.295 \times 10^4$ |

**Table 4**
Nondimensionalized simulation parameters used in parametric study.

| Parameters | $\kappa_\eta$ | $\kappa_c$ | A | B | $M_{vol}$ | $M_{vap}$ | $M_{surf}$ | $M_{gb}$ | $L$ |
|---|---|---|---|---|---|---|---|---|---|
| Case I | 0.5 | 1.0 | 16.0 | 1.0 | 0.0129 | 0.001 | 3.98 | 0.37 | M |
| Case II [40] | 1.0 | 10.0 | 16.0 | 1.0 | 0.01 | 0.001 | 4.0 | 0.4 | 10 M |
| Case III | 0.5 | 1.0 | 2.6 | 1.5 | 0.0129 | 0.001 | 3.98 | 0.37 | M |

Figure B.3. Example parameters of the sintering problem taken from [25].

For exampleone of the key parameters of the problem – intrinsic grain boundary mobility – is defined as

$$M_{gb} = M_{gb0} \exp\left(-\frac{Q_{gb}}{kT}\right)$$

with activation energy $Q_{gb} \approx 288$ kJ/mol and prefactor $M_{gb0} = 0.01$ $m^4/J/s$.

| Property | Value |
|---|---|
| Surface energy ($\gamma_s$) | 0.5823 $eV/A^2$ [55] |
| GB energy ($\gamma_{GB}$) | 0.4285 $eV/A^2$ [55] |
| Bulk diffusion prefactor ($D_{vol0}$) | 42.8 $cm^2/s$ [56] |
| Activation energy for bulk diffusion ($Q_v$) | 640 kJ/mol [56] |
| Vacancy diffusion prefactor ($D_{vac0}$) | 0.04 $cm^2/s$ |
| Activation energy for vacancy diffusion ($Q_{vac}$) | 2 eV/atom [57] |
| Surface diffusion prefactor ($D_{surf0}$) | 4.0 $cm^2/s$ [56] |
| Activation energy for surface diffusion ($Q_s$) | 3.14 eV/atom [56] |
| GB diffusion prefactor ($D_{GB0}$) | $1.41 \times 10^{-5}$ $m^2/s$ [58] |
| Activation energy for GB diffusion ($Q_{GB}$) | 400 kJ/mol [56] |
| GB mobility ($M_{GB}$) | $3.5 \times 10^{-21}$ $m^4\ s^{-1}\ Pa^{-1}$ [59] |
| Molar volume ($V_m$) | 9.58 $cm^3$/mol [56] |
| Young's modulus (E) | 390 GPa [56] |
| Poisson's ratio (v) | 0.28 [56] |
| Thermal conductivity ($k$) | 1.75 W/cm/K [56] |

Figure B.4. Example parameters of the tungsten sintering problem taken from [26].

## B.2 Example of CeO2

Parameters of the phase field sintering model for $CeO_2$ are [17]: $\gamma_s = 1.5J/m^2$; $\gamma_{gb} = 1.0J/m^2$; $A = 4.126e-9J/m^3$; $B = 3.75e-8J/m^3$; $kn = 2e-9J/m$; $kc = 4e-9J/m$; and $M_{gb} = 3e-14m^3/kg/s$ for $T = 1673.15K$. This parameters correspond to the length scale $\delta = sqrt\left(\frac{4k_n}{3B}\right) \approx 2$ nm.

However, numerical stability of the PF model requires a few mesh points to be placed within the interfacial regions [17]. "Since the physical interface width is in nanometers, the grid spacing would be limited to about 1 nm. In this case, mesoscale simulations (with grain sizes in micrometers) will not be feasible. This model stiffness can be handled by selecting the value of the diffuse interface large enough; this alters the phase field model parameters without actually altering the thermodynamic driving forces or the kinetics."

The only choice within a uniform mesh finite difference scheme is to increase the interface thickness [81]. However, to ensure that the key parameters that control the microstructural evolution are not changed one has to keep either $\kappa_c$ or $\Delta f_0$, or their product $\kappa_c \cdot \Delta f_0$ unchanged, depending on the specific problem under consideration.

## B.3 Parameters of TiAlV

Parameters of the phase field sintering model for shown in Fig. B.5

**Table 2**
Material properties of 316 L stainless steel, Ti and Ni used in PF model.

| Materials | | 316L | Ti | Ni |
|---|---|---|---|---|
| GB diffusion | Prefactor *Dgb0* (cm2/s) | 0.127 | 90 | 4.8 |
| | Activation energy *Qgb* (eV) | 0.58 | 1.93 | 1.71 |
| Surface diffusion | Prefactor *Dsyrf0* (cm2/s) | 4 × 103 | 0.47 | 23.9 |
| | Activation energy *Qsurf* (eV) | 2.21 | 1.3 | 1.85 |
| Volume diffusion | Prefactor *Dvol0* (cm2/s) | 2 | 3.58 × 10–4 | 0.92 |
| | Activation energy *Qvol* (eV) | 2.6 | 1.353 | 2.88 |
| GB mobility | Prefactor (m4/J/s) | 5.53 × 10–8 | 5.53 × 10–8 | 1.51 × 10–6 |
| | Activation energy (eV) | 0.171 | 0.171 | 0.26 |
| Surface energy $\gamma s$ (J/m2) | | 2.41 | 2 | 1.9 |
| GB energy $\gamma gb$ (J/m2) | | 1.06 | 1.1 | 0.87 |

Figure B.5. Parameters for mobility of Ti and Ni taken from [91].

**Ti-6Al-4V: Surface and grain boundary free energy**

| Temperature °C | Temperature °F | Surface free energy, ($F_s$) ergs/cm² | Grain boundary free energy, ergs/cm² | $\gamma_{gb}/F_s$ |
|---|---|---|---|---|
| 1137.3 | 2080 | 2095 | 810 | 0.39 |
| 1176.7 | 2150 | 2110 | 815 | 0.39 |
| 1221.1 | 2230 | 2010 | 815 | 0.40 |
| 1285.0 | 2345 | 2050 | 830 | 0.40 |

T.A. Roth, Elevated Temperature Values of the Surface and Grain Boundary Free Energies for Pure Titanium and Ti-6Al-4V, InterAmerican Conference on Materials Technology, Southwest Research Institute, 1978

Figure B.6. Surface and grain boundary energy for Ti-6Al-4V alloy [77].

# C Coble model

Here we consider briefly approximations used in Coble model [30, 31] of two particles of different size.

## C.1 Approximated geometry

In this model two spheres with radii $R_1$ and $R_2$ are sintering via surface diffusion. Approximated geometry of the Coble model is shown in Fig. C.7.

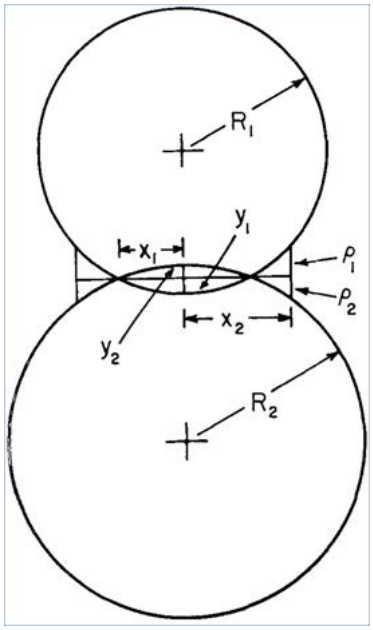


Figure C.7. Schematic cross-section of pair of sintering spheres

The two spherical caps of the overlapping spheres have heights $y_1$ and $y_2$

$$y_1 = \frac{x_1^2}{R_1} \qquad \text{and} \qquad y_2 = \frac{x_1^2}{R_2}. \tag{C.10}$$

The volume of the spherical cap is ($V_1 = \pi/3 y_1^2(3R_1 - y_1)$):

$$V_1 = \pi x_1^2 y_1 - \int_0^{x_1} 2\pi x y dx$$

and we have volumes of the spherical caps approximated as

$$V_1 = \frac{\pi x_1^4}{4R_1} \qquad \text{and} \qquad V_2 = \frac{\pi x_1^4}{4R_2}. \tag{C.11}$$

The mass of particles diffused across the interface is redistributed in the neck such that

$$V_1 + V_2 = V_3 + V_4,$$

where

$$V_{3,4} = \int_{x_1}^{x_2} 2\pi x(y - y_{1,2})dx$$

and the condition of the volume conservation gives

$$x_2 = \sqrt{2}x_1. \tag{C.12}$$

The size of the neck is then

$$\rho_1 = y_1 = \frac{x_2^2}{4R_1} \qquad \text{and} \qquad \rho_2 = y_2 = \frac{x_2^2}{4R_2}. \tag{C.13}$$

### C.2 Diffusion

Flux from the particle surface to the axis at the neck

$$J = 4\pi l D_v \Delta C \tag{C.14}$$

where $l$ is a unit of a cylinder (?), $D_v$ is the vacancy diffusion coefficient, $\Delta C$ is the difference in concentration between the surface and axis of the species transported.

## D Wakai model

### D.1 Wakai model: sintering stress [90]

Sintering stress is defined as

$$\sigma_i = \sigma_i^s + C_{ij}\dot{\varepsilon}_j \tag{D.15}$$

here $\sigma_i$ is applied stress, $\sigma_i^s$ is sintering stress, $C_{ij}$ is the viscosity tensor, and $\dot{\varepsilon}_i$ is the strain rate defined by

$$\dot{\varepsilon}_i = \dot{\varepsilon}_i^f + \frac{\sigma_i}{E_i} - \frac{\nu_{ij}}{E_i}\sigma_i \tag{D.16}$$

where $E_i$ is the uniaxial viscosity, $\nu_{ij}$ is the viscous Poisson's ratio, and $\dot{\varepsilon}_i^f$ is the free strain rate.

The free sintering rates and the uniaxial viscosity are all functions of density and microstructure, and they can be extracted from mechanical tests. In addition to this semi-empirical approach, it is necessary to establish a solid theoretical grounding for determining the sintering stress directly from the knowledge of the microstructure. This is possible when we assume some idealized particle arrangements as models.

A porous material shrinks when the total energy decreases with decreasing pore volume. Sintering stress is a concept that gives the relation between the total energy change and the pore volume change

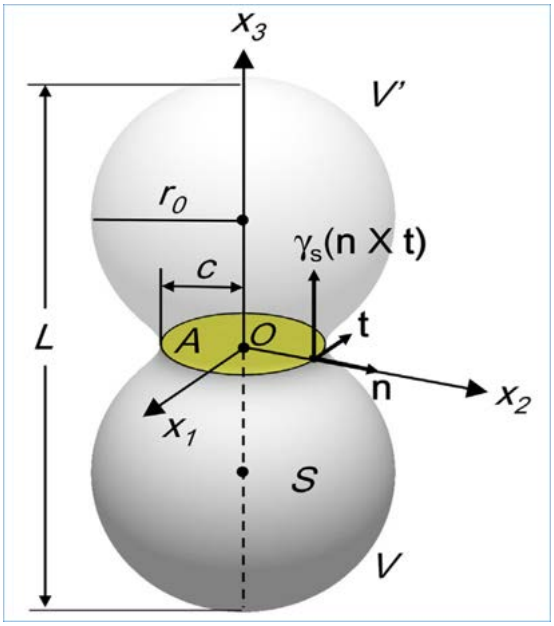


Figure D.8. Geometry of the two particle model in three dimensions.

Atoms on a particle surface have a chemical potential proportional to the surface curvature [88]

$$\mu = \mu_0 - \gamma_s \kappa \Omega \tag{D.17}$$

where $\mu_0$ is the standard chemical potential of the material, $\gamma_s$ is the surface energy, $\kappa = -2/r$ ($r$ is the sphere radius) is the surface curvature, and $\omega$ is the atomic volume. The positive normal stress on the surface $\gamma_s \kappa$ is tension and the negative one compression. Nite that on the flat grain boundary the chemical potential is

$$\mu = \mu_0 - \sigma_n \Omega$$

where $\sigma_n$ is normal traction.

The surface near the neck is the source of vacancy and the grain boundary is assumed to be a perfect sink of vacancies. The relative motion of two particles normal to the boundary takes place when the vacancies are annihilated at the grain boundary.

## D.2 Diffusion fux and stress distribution

The diffusive flux $j_{gb}$ along the grain boundary is proportional to the gradient of chemical potential:

$$j_{gb} = -\frac{\delta D_{gb}}{kT} \frac{1}{\Omega} \nabla_s \mu = \frac{\delta D_{gb}}{kT} \nabla_s \sigma_n \tag{D.18}$$

where $\delta$ is the grain boundary thickness and $D_{gb}$ is the surface diffusion coefficient.

The divergence of the flux times the atomic volume is equal to the normal component of the relative velocity $\dot{u}_n$

$$\Omega \nabla_s \cdot j_{gb} = -\dot{u}_n \tag{D.19}$$

and the normal stress is distributed according to a solution of the Poisson's equation

$$\nabla_s^2 \sigma_n = -\frac{kT}{\Omega \delta D_{gb}} \dot{u}_n \tag{D.20}$$

Solution to the Poisson's equation with boundary condition at the neck $\sigma_n = \gamma_s \kappa_{neck}$ is

$$\sigma_n = \gamma_s \kappa_{neck} + \frac{kT}{4\Omega \delta D_{gb}} \dot{u}_n (x^2 - r^2) \tag{D.21}$$

## D.3 Sintering velocity

To find equation for sintering velocity one can use condition of the balance between normal stress and surface tension

$$\int_{A_{gb}} \sigma_n \mathbf{e} dS = -\int_C \gamma_s (\mathbf{n} \times \mathbf{t}) dr + \mathbf{F}_{ext} \cdot \mathbf{e} \tag{D.22}$$

where $F_{ext}$ is the external field, $\mathbf{e}$ is the unit normal vector to the grain boundary, $\mathbf{n}$ is the unit normal vector to the surface, and $\mathbf{t}$ is the unit tangent vector along the surface triple junction $C$ as shown in Fig. D.8.

Using (D.21) we have

$$-\frac{\pi x^4 kT}{8\Omega \delta D_{gb}} \dot{u}_n = \gamma_s \kappa_{neck} A_{gb} + \int_C \gamma_s (\mathbf{n} \times \mathbf{t}) \cdot \mathbf{e} dr + F_{ext,n} \tag{D.23}$$

or by introducing effective viscosity $\eta_{eff} = \frac{\pi x^4 kT}{8\Omega \delta D_{gb}}$

$$\eta_{eff} \dot{\mathbf{u}}_n = -\mathbf{F}^s = -\gamma_s \kappa_{neck} A_{gb} \cdot \mathbf{e} - \int_C \gamma_s (\mathbf{n} \times \mathbf{t}) dr + F_{ext,n} \cdot \mathbf{e} \tag{D.24}$$

For circular geometry (the only geometry considered in this work)

$$F^s = \gamma_s \kappa_{neck} A_{gb} + \gamma_s L \sin\left(\frac{\psi}{2}\right) + F_{ext,n} \cdot \mathbf{e} \tag{D.25}$$

where $L = 2\pi x$ is the circumference and dihedral angle $\psi$ is given by the ratio of the grain boundary energy $\gamma_{gb}$ to the surface energy $\gamma_s$

$$\cos\left(\frac{\psi}{2}\right) = \frac{\gamma_{gb}}{2\gamma_s}$$

### D.4 Effective viscosity and neck growth

Dimensionless time of diffusion $t^*$

$$t^* = \frac{\gamma_s \Omega \delta D_s}{kT r_0^4} t = \frac{\pi \gamma_s}{8 \eta_{eff}} \left(\frac{x}{r_0}\right)^4 \tag{D.26}$$

is to be compared with Frenkel-Pokluda time $t^* = \frac{\Gamma}{a_0 \eta} t$, see (**??**).

And the neck growth rate can be approximated as

$$\left(\frac{x}{r_0}\right)^m = \frac{8 \eta_{eff}}{\pi \gamma_s} t, \tag{D.27}$$

which has to be compared with (**??**):

$$\left(\frac{\theta}{a_0}\right)^2 = \frac{\Gamma}{\eta a_0^3} t \qquad \text{or} \qquad \left(\frac{x}{a_0}\right)^2 \approx \frac{\Gamma}{\eta a_0} t, \tag{D.28}$$

where we used Coble approximation for small angles $x = a_0 \theta$.

## E Kinetic Monte Carlo simulation [62]

The simplest example of the kinetic Monte Carlo (kMC) model that can be used to model sintering dynamics is Potts kMC model [62]. Traditionally this is called an Ising model and has been used to study the dynamics of magnetic spin systems. The model has also been used to study the microstructural evolution of grain boundaries, since the two states can code for the two crystal orientations either side of a single grain boundary, and so be used to simulate the behavior of bicrystals.

The Ising model can capture not just the basic characteristics of a boundary, such as its interface free energy, but also the subtleties of the second derivative of energy with respect to boundary orientation and thus be used to investigate the impact of the Herring equation on curvature driven growth.

The Ising model describes an ideal two component system in which space is typically discretized into a regular array of lattice sites, in which the state is described in terms of the set of components of the system, called spins, which are associated with each lattice site, $s_i \in \{0, 1\}$, where $i$ labels the lattice site. The system defines a boundary between unlike spins and no boundary between like spins in the following way:

$$\gamma(s_i, s_j) = \begin{cases} 0 & \text{for } s_i = s_j \\ \dfrac{J}{2} & \text{for } s_i \neq s_j \end{cases} \tag{E.29}$$

where $i$ represents a site and $j$ its neighbor, and $J(> 0)$ is an interfacial energy constant of the system. The energy of the system is then

$$E = \sum_{i=1}^{N} \sum_{j=1}^{z} \gamma(s_i, s_j)$$

where $N$ is the total number of lattice sites in the system and $z$ is the maximum number of neighbors.

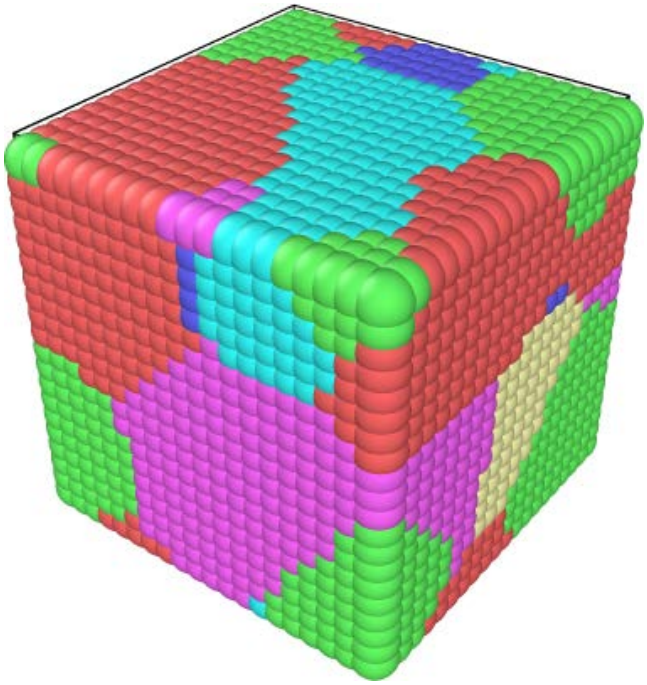

Figure E.9. Example of implementtion of the Potts model in SPPARKS.

In the presence of an external or volume driving force a modified Hamiltonian takes form

$$E = \sum_{i=1}^{N} \sum_{j=1}^{z} \gamma(s_i, s_j) - H \sum_{i=1}^{N} s_i$$

where $H(> 0)$ lowers the energy of one type of spin with respect to the other.

To simulate system dynamics one can run through each lattice site and chose at random new state of the site. The probability of transition to the new state is governed by the transition function in Metropolis or symmetric form

$$P(\Delta E) = \begin{cases} 1 & \text{for } \Delta E \leq 0 \\ \exp \dfrac{-\Delta E}{kT} & \text{for } \Delta E > 0 \end{cases} \quad \text{or} \quad P(\Delta E) = \frac{1}{2}\left(1 - \tanh \frac{\Delta E}{2kT}\right).$$

This algorithm is implemented in SPPARKS code by Sandia labs [21]. An example of the simulations is shown in Fig.

# F Master sintering curve [39]

The ability to predict material densification behavior for a given thermal history is an important result of sintering studies and has been made possible in part through the development of the master sintering curve (MSC) theory by [84]. It is practical for industrial use to predict the densification result for a given thermal history [72] through experimental observations and not purely through modeling or simulation.

Typically a sintering study involves running a series of powder specimens, with identical green-body preparation, through different thermal histories. Because of differences in either heating rate or hold temperature, specimens will exhibit different densification histories, as well as densification-temperature profiles. When the densification-temperature profiles are plotted against the amount of work performed, they will overlap forming the MSC.

The MSC approach is based on the ideas of the Combined-Stage Sintering Model by [47]. In this theory the instantaneous linear shrinkage rate is given by [84]

$$-\frac{dL}{Ldt} = \frac{\gamma\Omega}{kT}\left(\frac{\Gamma_v D_v}{G^3} + \frac{\Gamma_b \delta D_b}{G^4}\right)$$

where $\gamma$ is the surface energy, $\Omega$ the atomic volume. $k$ is the Boltzmann constant, $T$ is the absolute temperature, $G$ the mean grain diameter, $D_v$ and $D_b$ the coefficients for volume and grain boundary diffusion, respectively, and $\delta$ the width of the grain boundary. $\Gamma$ is lumped parameter, which relate the driving force, mean diffusion distance, and other geometric features of the micro-structure on which the sintering rate depends on the mean grain diameter.

Thus, $\Gamma$ relates the instantaneous linear shrinkage rate to the diffusion coefficient and other material parameters and mean grain diameter. For isotropic shrinkage

$$-\frac{dL}{Ldt} = \frac{d\rho}{3\rho dt}$$

where $\rho$ is the bulk density.

For one dominating mechanism of diffusion shrinkage equation can be simplified to

$$\frac{d\rho}{3\rho dt} = \frac{\gamma\Omega(\Gamma(\rho))D_0}{kT(G(\rho))^n}\exp\left(-\frac{Q}{kT}\right)$$

where $Q$ is the apparent activation energy; $R$ the gas constant; $D_0 = (D_v)_0$ and $n = 3$ for volume diffusion; and $D_0 = (\delta D_b)_0$ and $n = 4$ for grain-boundary diffusion.

The sintering equation can be rearrange and integrated as follows

$$\int_{\rho_0}^{\rho} \frac{(G(\rho))^n}{3\rho\Gamma(\rho)} d\rho = \int_0^t \frac{\gamma\Omega D_0}{kT}\exp\left(-\frac{Q}{RT}\right)dt$$

where $\rho_0$ is the green density of the powder compact.

The atomic diffusion process and the micro-structural evolution are separated in the last equation. The right-hand side (rhs) is related to atomic diffusion while left-hand (lhs) site is related to the micro-structural evolution. One can also combine the micro-structural and material properties on the lhs while the rhs will on depend on temperature and activation energy

$$\Phi(\rho) = \frac{k}{\gamma\Omega D_0}\int_{\rho_0}^{\rho}\frac{(G(\rho))^n}{3\rho\Gamma(\rho)}d\rho \qquad \Theta(t,T(t)) = \int_0^t \frac{1}{T}\exp\left(-\frac{Q}{RT}\right)dt$$

One way to construct the MSC is to obtain the mean grain size-density trajectory and the relationship between $\Gamma(\rho)$ and $\rho$ and then integrate the equation for $\Phi(\rho)$.

## G Equilibrium pore surfaces: sintering stress [85]

The sintering stress, $\sigma_s$, is defined as the mechanical hydrostatic stress which just balances the internal surface tension forces so that the porous solid does not shrink

$$\sigma_s dV = \gamma_b dA_b + \gamma_s dA_s \quad \text{and} \quad \sigma_s = \gamma_b\left(\frac{\partial A_b}{\partial V}\right) + \gamma_s\left(\frac{\partial A_s}{\partial V}\right)$$

where $dV$ is a virtual change of the volume of the pores (at a fixed volume of the grains) and $dA_b$ and $dA_s$ are the associated changes of the grain boundary area and surface area, respectively.

To evaluate partial derivatives let us consider forces acting at the interfaces. At equilibrium

$$\sigma_s dV = \frac{1}{2}\sum_i F_i du_i$$

where $F_i$ is the force acting on grain facet $i$, and $du_i$ is the virtual displacement across facet $i$, which is associated with a volume change $dV$.

The force at the interface has two components: (i) due grain boundary: $2\gamma_s\kappa A_i$ where $A_i$ is the contact area, $\gamma_s$ is the specific surface energy, and $\kappa$ is the mean curvature ($\kappa = 1/\rho$ and $\rho$ is the mean curvature radius); and (ii) due to the surface tension: $\gamma_s L_i \sin(\Psi)$ where $L_i$ is the circumference of the contact and $\Psi$ is dihedral angle. Hence

$$\sigma_s = \frac{1}{2}\gamma_s\sum_i (2\kappa A_i + L_i\sin(\Psi))\, du_i/dV.$$

For the tetrakaidekahedron, for example

$$du_4 = \frac{dV}{12a^2} \qquad \text{and} \qquad du_4 = \frac{\sqrt{3}dV}{24a^2}.$$

Estimations of the sintering stress are considered in the main text Part IV.

## References


1. Techshot FabLab Level 4 PDR Data Package Document No: G914DD3895 Rev

2. Material Trade Study Report Techshot FabLab Phase A. Document Number: G914DD3584. Report Number: G914DD3584 November 30, 2018.

3. I. AitMansour at al. Designdependent shrinkage compensation modeling and mechanical property targeting of metal FFF. Progress in Additive Manufacturing (2020) 5:5157.

4. Joan Horvath Rich Cameron Mastering 3D Printing: A Guide to Modeling, Printing, and Prototyping. CHAPTER 11 Metal 3D Printing and Casting 2020.

5. V.V. Skorohod, Rheological basis of the theory of sintering, Naukova Dumka, Kiev, 1972

6. Skorohod, V. V., Olevsky, E. A., Shtern, M. B. (1991). Continuum Theory for Sintering of Porous Bodies: Model and Application. Science of Sintering 23(2): 79-91.

7. Olevsky, E.A. (1998) Theory of sintering: from discrete to continuum. Mater. Sci. Eng., R, 23 (2), 41100.

8. H. H. Sherief, F. Hamza and H. A. Saleh, The theory of generalized thermoelastic diffusion. Int. J. Eng. Sci., 42 (2004) 591-608.

9. W.Nowacky. Thermoelasticity. 2nd Ed. Pergamon, 1986

10. D. Godec at al. Optimization of the 3D Printing Parameters for Tensile Properties of Specimens Produced by Fused Filament Fabrication of 17-4PH Stainless Steel. Materials 2020, 13, 774; doi:10.3390/ma13030774 www.mdpi.com/journal/materials

11. Riedel, H. (1990). A Constitutive Model for the Finite-element Simulation of Sintering-Distortions and Stresses. Ceramic Powder Science III. pp.619-630.

12. Z. Long and Z. Heng-wei. Sintering driving force of Al2O3 powders at the initial stage of pulse electric current sintering under thermoelastic diffusion Long and Heng-wei International Journal of Mechanical and Materials Engineering (2018) 13:9.

13. C. G. Cardona at al. On Sintering Stress in Complex Powder Compacts. J. Am. Ceram. Soc., 95 [8] 23722382 (2012)

14. R. Zuo, E. Aulbach, J. Rodel. Experimental determination of sintering stresses and sintering viscosities. Acta Materialia 51 (2003) 45634574

15. Takashi Kurose at al. Influence of the Layer Directions on the Properties of 316L Stainless Steel Parts Fabricated through Fused Deposition of Metals. Materials 2020, 13, 2493; doi:10.3390/ma13112493

16. Mukesh K. Agarwala, Vikram R. Jamalabad, Noshir A. Langrana, Ahmad Safari, Philip J. Whalen, and Stephen C. Danforth. Structural quality of parts processed by fused deposition. *Rapid Prototyping Journal*, 2(4):4–19, dec 1996.

17. K Ahmed, C A Yablinsky, A Schulte, T Allen, and A El-Azab. Phase field modeling of the effect of porosity on grain growth kinetics in polycrystalline ceramics. *Modelling and Simulation in Materials Science and Engineering*, 21(6):065005, jul 2013.

18. Karim Ahmed. *Phase Field Modeling of Grain Growth in Porous Polycrystalline Solids*. PhD thesis, 2015.

19. Masoumeh Aminzadeh and Thomas R. Kurfess. Online quality inspection using bayesian classification in powder-bed additive manufacturing from high-resolution visual camera images. *Journal of Intelligent Manufacturing*, 30(6):2505–2523, mar 2018.

20. M I Baskes and R A Johnson. Modified embedded atom potentials for HCP metals. *Modelling and Simulation in Materials Science and Engineering*, 2(1):147–163, jan 1994.

21. Corbett C. Battaile. The kinetic monte carlo method: Foundation, implementation, and application. *Computer Methods in Applied Mechanics and Engineering*, 197(41-42):3386–3398, jul 2008.

22. Y. Bengio, A. Courville, and P. Vincent. Representation learning: A review and new perspectives. *IEEE Transactions on Pattern Analysis and Machine Intelligence*, 35(8):1798–1828, aug 2013.

23. P.J. Besl and Neil D. McKay. A method for registration of 3-d shapes. *IEEE Transactions on Pattern Analysis and Machine Intelligence*, 14(2):239–256, feb 1992.

24. S. Bulent Biner. An overview of the phase-field method and its formalisms. In *Programming Phase-Field Modeling*, pages 1–7. Springer International Publishing, 2017.

25. Sudipta Biswas, Daniel Schwen, Jogender Singh, and Vikas Tomar. A study of the evolution of microstructure and consolidation kinetics during sintering using a phase field modeling based approach. *Extreme Mechanics Letters*, 7:78–89, jun 2016.

26. Sudipta Biswas, Daniel Schwen, and Vikas Tomar. Implementation of a phase field model for simulating evolution of two powder particles representing microstructural changes during sintering. *Journal of Materials Science*, 53(8):5799–5825, dec 2017.

27. R Bordia, R Zuo, O Guillon, S Salamone, and J Rodel. Anisotropic constitutive laws for sintering bodies. *Acta Materialia*, 54(1):111–118, jan 2006.

28. Cristina G. Cardona, Veena Tikare, Burton R. Patterson, and Eugene Olevsky. On sintering stress in complex powder compacts. *Journal of the American Ceramic Society*, 95(8):2372–2382, apr 2012.

29. Sushmit Chowdhury and Sam Anand. Artificial neural network based geometric compensation for thermal deformation in additive manufacturing processes. In *Volume 3: Joint MSEC-NAMRC Symposia*. American Society of Mechanical Engineers, jun 2016.

30. R. L. Coble. Initial sintering of alumina and hematite. *Journal of the American Ceramic Society*, 41(2):55–62, feb 1958.

31. R. L. Coble. Effects of particle-size distribution in initial-stage sintering. *Journal of the American Ceramic Society*, 56(9):461–466, sep 1973.

32. COMSOL. Comsol multiphysics reference manual, version 5.5, comsol inc., 2020.

33. P. Dadvand, R. Rossi, M. Gil, X. Martorell, J. Cotela, E. Juanpere, S.R. Idelsohn, and E. Oñate. Migration of a generic multi-physics framework to HPC environments. *Computers & Fluids*, 80:301–309, jul 2013.

34. Pooyan Dadvand, Riccardo Rossi, and Eugenio Oñate. An object-oriented environment for developing finite element codes for multi-disciplinary applications. *Archives of Computational Methods in Engineering*, 17(3):253–297, jul 2010.

35. I E Dzyaloshinskii, E M Lifshitz, and Lev P Pitaevskii. GENERAL THEORY OF VAN DER WAALS' FORCES. *Soviet Physics Uspekhi*, 4(2):153–176, feb 1961.

36. R. M. Geman. Sintering solutions aboard the international space station., 2018.

37. Randall M. German. *Sintering: from Empirical Observations to Scientific Principles*. Elsevier, 2014.

38. Luca M. Ghiringhelli, Jan Vybiral, Sergey V. Levchenko, Claudia Draxl, and Matthias Scheffler. Big data of materials science: Critical role of the descriptor. *Physical Review Letters*, 114(10), mar 2015.

39. Michael C. Golt, Kristopher D. Behler, and Jerry C LaSalvia. A software tool for the rapid analysis of the sintering behavior of particulate bodies. 2017.

40. Haijun Gong, Dean Snelling, Kamran Kardel, and Andres Carrano. Comparison of stainless steel 316l parts made by FDM- and SLM-based additive manufacturing processes. *JOM*, 71(3):880–885, nov 2018.

41. Joamin Gonzalez-Gutierrez, Santiago Cano, Stephan Schuschnigg, Christian Kukla, Janak Sapkota, and Clemens Holzer. Additive manufacturing of metallic and ceramic components by the material extrusion of highly-filled polymers: A review and future perspectives. *Materials*, 11(5):840, may 2018.

42. Joamin Gonzalez-Gutierrez, Ivica Duretek, Florian Arbeiter, Christian Kukla, and Clemens Holzer. Filler content and properties of highly filled filaments for fused filament fabrication of magnets. 2017.

43. Joamin Gonzalez-Gutierrez, Damir Godec, Christian Kukla, Thomas Schlauf, Carlo Burkhardt, and Clemens Holzer. Shaping, debinding and sintering of steel components via fused filament fabrication. In *16th International Scientific Conference on Production Engineering - Computer Integrated Manufacturing and High Speed Machining, At Zadar, Croatia*, volume 16, 06 2017.

44. Joamn Gonzlez-Gutirrez, Gustavo Beulke, and Igor Emri. Powder injection molding of metal and ceramic parts. In *Some Critical Issues for Injection Molding*. InTech, mar 2012.

45. J. C. Gower. Generalized procrustes analysis. *Psychometrika*, 40(1):33–51, mar 1975.

46. Ian Greenquist, Michael R. Tonks, Larry K. Aagesen, and Yongfeng Zhang. Development of a microstructural grand potential-based sintering model. *Computational Materials Science*, 172:109288, feb 2020.

47. James D. Hansen, Richard P. Rusin, Mao-Hua Teng, and D. Lynn Johnson. Combined-stage sintering model. *Journal of the American Ceramic Society*, 75(5):1129–1135, may 1992.

48. B. Hausnerova, T. Kitano, I. Kuritka, J. Prindis, and L. Marcanikova. The role of powder particle size distribution in the processability of powder injection molding compounds. *International Journal of Polymer Analysis and Characterization*, 16(2):141–151, feb 2011.

49. Pierre Hirel. Atomsk: A tool for manipulating and converting atomic data files. *Computer Physics Communications*, 197:212–219, dec 2015.

50. Nathanaël Hozé and David Holcman. Statistical methods for large ensembles of super-resolution stochastic single particle trajectories in cell biology. *Annual Review of Statistics and Its Application*, 4(1):189–223, mar 2017.

51. D. Lynn Johnson. New method of obtaining volume, grain-boundary, and surface diffusion coefficients from sintering data. *Journal of Applied Physics*, 40(1):192–200, jan 1969.

52. Anuj Karpatne, Gowtham Atluri, James H. Faghmous, Michael Steinbach, Arindam Banerjee, Auroop Ganguly, Shashi Shekhar, Nagiza Samatova, and Vipin Kumar. Theory-guided data science: A new paradigm for scientific discovery from data. *IEEE Transactions on Knowledge and Data Engineering*, 29(10):2318–2331, oct 2017.

53. Arnd Koeppe, Carlos Alberto Hernandez Padilla, Maximilian Voshage, Johannes Henrich Schleifenbaum, and Bernd Markert. Efficient numerical modeling of 3d-printed lattice-cell structures using neural networks. *Manufacturing Letters*, 15:147–150, jan 2018.

54. Abdullah Konak, Sadan Kulturel-Konak, Alice E. Smith, and Ian Nettleship. Estimation of shrinkage for near net-shape using a neural network approach. *Journal of Intelligent Manufacturing*, 14(2):219–228, 2003.

55. Christian Kukla, Joamin Gonzalez-Gutierrez, Carlo Burkhardt, Oxana Weber, and Clemens Holzer. The production of magnets by fff - fused filament fabrication. In *EuroPM 2017*, *At Milan*, *Italy*, 10 2017.

56. Christian Kukla, Joamin Gonzalez-Gutierrez, Santiago Cano, Stefan Hampel, Carlo Burkhardt, Tassilo Moritz, and Clemens Holzer. Fused filament fabrication (fff) of pim feedstocks. In *VI Congreso Nacional de Pulvimetalurgia y I Congreso Iberoamericano de Pulvimetalurgia*, *At Ciudad Real*, *Spain*, *Volume: VI*, 06 2017.

57. Christian Kukla, Joamin Gonzalez-Gutierrez, Ivica Duretek, Stephan Schuschnigg, and Clemens Holzer. Effect of particle size on the properties of highly-filled polymers for fused filament fabrication. Author(s), 2017.

58. Ohyung Kwon, Hyung Giun Kim, Min Ji Ham, Wonrae Kim, Gun-Hee Kim, Jae-Hyung Cho, Nam Il Kim, and Kangil Kim. A deep neural network for classification of melt-pool images in metal additive manufacturing. *Journal of Intelligent Manufacturing*, 31(2):375–386, oct 2018.

59. Byeong-Joo Lee, M.I. Baskes, Hanchul Kim, and Yang Koo Cho. Second nearest-neighbor modified embedded atom method potentials for bcc transition metals. *Physical Review B*, 64(18), oct 2001.

60. D. G. Luchinsky and P. V. E. McClintock. Irreversibility of classical fluctuations studied in analogue electrical circuits. *Nature*, 389(6650):463–466, October 1997.

61. L. Merz, S. Rath, V. Piotter, R. Ruprecht, J. Ritzhaupt-Kleissl, and J. Hausselt. Feedstock development for micro powder injection molding. *Microsystem Technologies*, 8(2-3):129–132, may 2002.

62. Mark Miodownik. Monte carlo potts model. In *Computational Materials Engineering*, pages 47–108. Elsevier, 2007.

63. Nele Moelans, Bart Blanpain, and Patrick Wollants. An introduction to phase-field modeling of microstructure evolution. *Calphad*, 32(2):268–294, jun 2008.

64. Amir Mostafaei, Pierangeli Rodriguez De Vecchis, Ian Nettleship, and Markus Chmielus. Effect of powder size distribution on densification and microstructural evolution of binder-jet 3d-printed alloy 625. *Materials & Design*, 162:375–383, jan 2019.

65. William Mycroft, Mordechai Katzman, Samuel Tammas-Williams, Everth Hernandez-Nava, George Panoutsos, Iain Todd, and Visakan Kadirkamanathan. A data-driven approach for predicting printability in metal additive manufacturing processes. *Journal of Intelligent Manufacturing*, 31(7):1769–1781, feb 2020.

66. S. Nosewicz, J. Rojek, K. Pietrzak, and M. Chmielewski. Viscoelastic discrete element model of powder sintering. *Powder Technology*, 246:157–168, sep 2013.

67. Eugene A. Olevsky. Theory of sintering: from discrete to continuum. *Materials Science and Engineering: R: Reports*, 23(2):41–100, jun 1998.

68. Eugene A. Olevsky, Veena Tikare, and Terry Garino. Multi-scale study of sintering: A review. *Journal of the American Ceramic Society*, 89(6):1914–1922, jun 2006.

69. Biranchi Panda, K. Shankhwar, Akhil Garg, and M. M. Savalani. Evaluation of genetic programming-based models for simulating bead dimensions in wire and arc additive manufacturing. *Journal of Intelligent Manufacturing*, 30(2):809–820, nov 2016.

70. Joseph A. Pask. Thermodynamic and geometric factors in sintering. In *Sintering Key Papers*, pages 567–578. Springer Netherlands, 1990.

71. Ondřej Pokluda, Céline T. Bellehumeur, and John Vlachopoulos. Modification of frenkel's model for sintering. 43:3253 – 3256, 12 1997.

72. V. Pouchly and K. Maca. Master sintering curve: A practical approach to its construction. *Science of Sintering*, 42(1):25–32, 2010.

73. Mohamed N. Rahaman. *Sintering of Ceramics*. Taylor & Francis Inc, 2007.

74. Sayyeda Saadia Razvi, Shaw Feng, Anantha Narayanan, Yung-Tsun Tina Lee, and Paul Witherell. A review of machine learning applications in additive manufacturing. In *Volume 1: 39th Computers and Information in Engineering Conference*. American Society of Mechanical Engineers, aug 2019.

75. Jerzy Rojek, Szymon Nosewicz, Kamila Jurczak, Marcin Chmielewski, Kamil Bochenek, and Katarzyna Pietrzak. Discrete element simulation of powder compaction in cold uniaxial pressing with low pressure. *Computational Particle Mechanics*, 3(4):513–524, dec 2015.

76. Jerzy Rojek, Szymon Nosewicz, Marcin Maździarz, Piotr Kowalczyk, Krzysztof Wawrzyk, and Dmytro Lumelskyj. Modeling of a sintering process at various scales. *Procedia Engineering*, 177:263–270, 2017.

77. T.A. Roth and P. Suppayak. The surface and grain boundary free energies of pure titanium and the titanium alloy ti6al4v. *Materials Science and Engineering*, 35(2):187–196, oct 1978.

78. SALOME. An open-source software for pre- and post-processing. https://docs.salome-platform.org/latest/gui/GEOM/index.html, 2020.

79. Uwe Scheithauer, Robert Johne, Steven Weingarten, Eric Schwarzer, Johannes Abel, Axel Müller-Köhn, Anne Günther, and Tassilo Moritz. CerAMfacturing: development of ceramic and multi material components by additive manufacturing methods for personalized medical products. *Journal of 3D Printing in Medicine*, 2(1):15–25, jan 2018.

80. Jonathan Schmidt, Mário R. G. Marques, Silvana Botti, and Miguel A. L. Marques. Recent advances and applications of machine learning in solid-state materials science. *npj Computational Materials*, 5(1), aug 2019.

81. C. Shen, Q. Chen, Y.H. Wen, J.P. Simmons, and Y. Wang. Increasing length scale of quantitative phase field modeling of growth-

dominant or coarsening-dominant process. *Scripta Materialia*, 50(7):1023–1028, apr 2004.

82. A K Sood, R K Ohdar, and S S Mahapatra. Parametric appraisal of fused deposition modelling process using the grey taguchi method. *Proceedings of the Institution of Mechanical Engineers, Part B: Journal of Engineering Manufacture*, 224(1):135–145, jul 2009.

83. Anoop K. Sood, Raj K. Ohdar, and Siba S. Mahapatra. Experimental investigation and empirical modelling of FDM process for compressive strength improvement. *Journal of Advanced Research*, 3(1):81–90, jan 2012.

84. Hunghai Su and D. Lynn Johnson. Master sintering curve: A practical approach to sintering. *Journal of the American Ceramic Society*, 79(12):3211–3217, dec 1996.

85. J. Svoboda, H. Riedel, and H. Zipse. Equilibrium pore surfaces, sintering stresses and constitutive equations for the intermediate and late stages of sintering—i. computation of equilibrium surfaces. *Acta Metallurgica et Materialia*, 42(2):435–443, feb 1994.

86. Young Rang Uhm, Jaewoo Kim, Kwang Jae Son, and Chul Sung Kim. Effect of particle size, dispersion, and particle–matrix adhesion on w reinforced polymer composites. *Research on Chemical Intermediates*, 40(5):2145–2153, mar 2013.

87. Silvia Vock, Burghardt Klöden, Alexander Kirchner, Thomas Weißgärber, and Bernd Kieback. Powders for powder bed fusion: a review. *Progress in Additive Manufacturing*, 4(4):383–397, feb 2019.

88. F. Wakai and K.A. Brakke. Mechanics of sintering for coupled grain boundary and surface diffusion. *Acta Materialia*, 59(14):5379–5387, aug 2011.

89. Fumihiro Wakai, Kota Katsura, Shun Kanchika, Yutaka Shinoda, Takashi Akatsu, and Kazunari Shinagawa. Sintering force behind the viscous sintering of two particles. *Acta Materialia*, 109:292–299, may 2016.

90. Fumihiro Wakai and Yutaka Shinoda. Anisotropic sintering stress for sintering of particles arranged in orthotropic symmetry. *Acta Materialia*, 57(13):3955–3964, aug 2009.

91. Gang Wang, De-chang Zeng, and Zhong-wu Liu. Phase field calculation of interface mobility in a ternary alloy. *Transactions of Nonferrous Metals Society of China*, 22(7):1711–1716, jul 2012.

92. Tianjiao Wang, Tsz-Ho Kwok, Chi Zhou, and Scott Vader. In-situ droplet inspection and closed-loop control system using machine

learning for liquid metal jet printing. *Journal of Manufacturing Systems*, 47:83–92, apr 2018.

93. Yu U. Wang. Computer modeling and simulation of solid-state sintering: A phase field approach. *Acta Materialia*, 54(4):953–961, feb 2006.

94. K. Wasmer, T. Le-Quang, B. Meylan, and S. A. Shevchik. In situ quality monitoring in AM using acoustic emission: A reinforcement learning approach. *Journal of Materials Engineering and Performance*, 28(2):666–672, oct 2018.

95. Krzysztof Wawrzyk, Piotr Kowalczyk, Szymon Nosewicz, and Jerzy Rojek. A constitutive model and numerical simulation of sintering processes at macroscopic level. Author(s), 2018.

96. Yeom, Ha, Kim, Jeong, Hwang, and Choi. Application of the discrete element method for manufacturing process simulation in the pharmaceutical industry. *Pharmaceutics*, 11(8):414, aug 2019.

97. Xing Zhang and Yiliang Liao. A phase-field model for solid-state selective laser sintering of metallic materials. *Powder Technology*, 339:677–685, nov 2018.

98. Yicha Zhang, Alain Bernard, Ramy Harik, and K. P. Karunakaran. Build orientation optimization for multi-part production in additive manufacturing. *Journal of Intelligent Manufacturing*, 28(6):1393–1407, feb 2015.

99. Ruzhong Zuo, Emil Aulbach, and Jürgen Rödel. Experimental determination of sintering stresses and sintering viscosities. *Acta Materialia*, 51(15):4563–4574, sep 2003.

## REPORT DOCUMENTATION PAGE

*Form Approved*
*OMB No. 0704–0188*



| 1. REPORT DATE *(DD-MM-YYYY)* | 2. REPORT TYPE | 3. DATES COVERED *(From - To)* |
|---|---|---|
| 01-10-2020 | Technical Memorandum | 03/2017–11/2018 |

**4. TITLE AND SUBTITLE**
Analysis of nonlinear shrinkage for the bound metal deposition manufacturing using multi-scale approach

**5a. CONTRACT NUMBER**

**5b. GRANT NUMBER**

**5c. PROGRAM ELEMENT NUMBER**

**6. AUTHOR(S)**
Dmitry G. Luchinsky, Vasyl Hafiychuk, Kevin R. Wheeler, Tracie J. Prater

**5d. PROJECT NUMBER**

**5e. TASK NUMBER**
15182.03.00.004.001

**5f. WORK UNIT NUMBER**

**7. PERFORMING ORGANIZATION NAME(S) AND ADDRESS(ES)**
NASA Ames Research Center
Moffett Field, California 94035-2199

**8. PERFORMING ORGANIZATION REPORT NUMBER**
L–12456

**9. SPONSORING/MONITORING AGENCY NAME(S) AND ADDRESS(ES)**
National Aeronautics and Space Administration
Washington, DC 20546-0001

**10. SPONSOR/MONITOR'S ACRONYM(S)**
NASA

**11. SPONSOR/MONITOR'S REPORT NUMBER(S)**
NASA/TM–2020–xxxxxx

**12. DISTRIBUTION/AVAILABILITY STATEMENT**
Unclassified-Unlimited
Subject Category 23
Availability: NASA CASI (443) 757-5802

**13. SUPPLEMENTARY NOTES**
An electronic version can be found at http://ntrs.nasa.gov.

**14. ABSTRACT**
We consider problem of nonlinear shrinkage of the metal part during bound metal deposition manufacturing on the ground and in zero-G. To analyze this problem we developed multi-scale physics-based approach that spans atomistic dynamics at the scale of nanoseconds and the full part shrinkage at the time scale of hours. Using this approach we estimated the key parameters of the problem including grain boundary width, coefficient of surface diffusion, initial redistribution of particles during debinding stage, micro-structure evolution from round particles to densely packed grains and corresponding change of the total and chemical free energy, and sintering stress. The introduced method was used to predict shrinkage at the level of two particles, filament cross-section, sub-model, and the whole green, brown, and metal parts. To further improve accuracy and reliability of the shrinkage predictions we propose concept of intelligent additive manufacturing of metal powders in space that combines the strengths of both physics-based and data-driven methods of analysis of AM.

**15. SUBJECT TERMS**
polymer, additive manufacturing, interface, welding, molecular dynamics

| 16. SECURITY CLASSIFICATION OF: | | | 17. LIMITATION OF ABSTRACT | 18. NUMBER OF PAGES | 19a. NAME OF RESPONSIBLE PERSON |
|---|---|---|---|---|---|
| a. REPORT | b. ABSTRACT | c. THIS PAGE | | | STI Help Desk (email: help@sti.nasa.gov) |
| U | U | U | UU | 78 | 19b. TELEPHONE NUMBER *(Include area code)* (443) 757-5802 |